Two-Dimensional Transition Metal Dichalcogenides for Ultrathin Solar Cells

Thesis by

Cora Margaret Went

In Partial Fulfillment of the Requirements

for the Degree of

Doctor of Philosophy

CALIFORNIA INSTITUTE OF TECHNOLOGY

Pasadena, California

2022

(Defended March 31, 2022)

Cora Margaret Went
ORCID: 0000-0001-7737-3348

Acknowledgements

First, I would like to thank my advisor, Harry Atwater, for being a source of motivation and inspiration throughout my PhD. Harry is a compassionate advisor who cares deeply about diversity, and as a result the culture in his lab is one of the most supportive I have seen. I have never met anyone who loves science as much as he does, and we need people like him in the world to make the discoveries that will enable a brighter future.

I would like to acknowledge my thesis committee—Professors Dave Hsieh, Nai-Chang Yeh, and Gil Refael—for providing excellent feedback on my work. In particular, Dave is both a powerful advocate for diversity at Caltech and an incredibly kind mentor, and I enjoyed collaborating with him to plan the first FUTURE of Physics conference, aimed to support undergraduate women in physics in their journey to graduate school.

Several postdocs and older graduate students generously shared their time, their physics knowledge, and their lab teachings with me. I would like to thank Zak Al Balushi, Mike Kelzenberg, Deep Jariwala, Artur Davoyan, Oggy Ilic, Yuri Lu, Michelle Sherrott, Will Whitney, Benji Vest, Yury Tokpanov, Yi-Rung Lin, Joe DuChene, and Wei-Hsiang Lin for their mentorship. I would like to thank Chris Chen and Carissa Eisler for taking me under their wing at my first conference, PVSC, before I even became a graduate student at Caltech. I also appreciate Professor George Rossman for sharing his spectroscopy equipment, his rocks, and his stories with me.

Two members of our group deserve special acknowledgement. Joeson Wong and Phil Jahelka are both brilliant scientists and skilled teachers, and they have taught me most of what I know about semiconductor and solar cell physics. They are also both great friends outside of lab. Joeson is an excellent travel buddy—I will never forget walking over 10 miles in Shanghai with him before a conference, eating street food and having great conversations along the way. Phil is an excellent running buddy and I have appreciated our recent conversations about climate change, solar cells, and the fate of the planet.

I would like to thank my other co-authors, including Souvik Biswas, Matthew Hunt, Abigail Carbone, Morgaine Mandigo-Stoba, Hannah Weaver, Dipti Jasrasaria, Eran Rabani, Naomi Ginsberg, Leanna Schulte, Ibadillah Digdaya, CX Xiang, and Shane Ardo for their contributions to this thesis. The PTL-EFRC collaboration has been quite the scientific adventure and I am grateful that we have become friends over the years. I appreciate everyone in the ARPA-E collaboration for teaching me technoeconomic analysis, chemistry, and carbon capture.

The Atwater Group has been such a fun, collaborative, and supportive place to do a PhD, and I appreciate all the members of the group whose paths crossed with mine. In particular, I would like to thank Haley, Megan, Rebecca, Kelly, Melissa, Prachi, Parker, Hamid, and many others for their friendship. My officemates, including Kelly, Melissa, Areum, Dagny, Laura, Lily, and Susana, have made Watson 252 such a fun and often lively place to work. I would also like to thank Catdog, my feline home officemate, for the endless snuggles and work disruptions. You can blame any typos in this thesis on him. I would like to thank Susana, Rachel and Miles for accepting the baton on the 2D PV project—I wish them the best of luck in their PhDs. Most importantly, I would like to thank the A-Team softball team for many perfectly defeated seasons, for always prioritizing fun and inclusivity, and for making summer softball something to look forward to every year!

I would like to thank Kam Flower, Jonathan Gross, Angie Riley, Lyann Lau, Liz Hormigoso, Tiffany Kimoto, Jennifer Blankenship, and Christy Jenstad for keeping our lab running, which has always seemed like a very challenging task. Mika Walton and Sofie Leon, among others, have made the physics department a measurably better place over their time at Caltech. I appreciate the Caltech Center for Inclusion and Diversity, especially Erin-Kate Escobar, and the Center for Teaching, Learning and Outreach, especially Jenn Weaver, for providing resources, training, and community. I appreciate GWiPMA (Gender Minorities & Women in Physics, Math & Astronomy), Caltech for Black Lives, and everyone else working towards a more equitable Caltech.

I am so grateful for my friends, and for all of the good conversations, delicious meals, and outdoor adventures that we have shared during my time in LA. Natalie, Chris, Haley,

Michael, Sara (and Cary) all started graduate school with me, and I am so lucky that we found each other our first year and shared this experience with each other. I am grateful for the softball crew, Sunrise friends, and all of the other friends whose paths have crossed with mine in LA at some point in the past six years, including Gwen, Melanie, Brittany, Missy, Ananda, Lucy, Alyssa, and Lauren. Although Jessica, Meg, and Bryn are not LA friends (yet), they have been indispensable sources of support, both over the phone and through visits.

My parents both have their PhDs in chemical engineering, and I have enjoyed relating to them through sharing stories about our graduate school experiences. My mom is responsible for my love of problem-solving and puzzles, and my most joyful research experiences have been those where I am approaching my research as I would solving a puzzle with her. She has continually reminded me of the intangible skills that you gain during a PhD. My dad is responsible for my tenacity, which he unfortunately was unable to instill in me as a young soccer player, but it now comes out when I am standing up for something I strongly believe in. I appreciate all the times that he stayed on the phone with me while I drove home after late nights in lab. My sister has deeply understood the challenges of my PhD, and has been one of my main sources of listening and support. She has served as a role model for me in so many ways during my PhD: her self-confidence (particularly as a woman in a male-dominated field); her ability to prioritize family, friends and time outdoors despite overwhelming amounts of work; and her willingness to think deeply about life.

Finally, I would like to thank my fiancé, Emily Wyatt, for her consistent love and encouragement. She got her PhD from Caltech a few years ahead of me, and she has guided me through this process in countless ways. Her support has come in the form of insightful advice that fundamentally changed the way I approached my PhD, many meals cooked throughout the writing of this thesis, and most importantly, intentional and loving emotional support through difficult times. I got through some of the hardest points in my PhD by remembering that I would not have met her if I had not come to Caltech. I quite honestly could not have finished my PhD without her, and I cannot wait to marry her in June!

Abstract

Ultrathin solar cells, with absorber layers less than one micron thick, have the potential to use orders of magnitude less high-quality semiconducting material than current silicon solar cells. This could be advantageous in applications that require high power output per unit weight, such as vehicle-integrated photovoltaics, or where reducing the capital cost of solar cell manufacturing is important. Transition metal dichalcogenides are a promising candidate for the semiconducting absorber layer of ultrathin solar cells due to their intrinsically passivated surfaces and their high absorption per unit thickness.

This thesis explores two-dimensional transition metal dichalcogenides for ultrathin photovoltaics. We start with the simplest type of solar cell, which collects carriers via a Schottky junction formed by sandwiching the absorber layer between two metal contacts with different work functions. To enable this geometry and avoid Fermi-level pinning, we develop a new process for gently transferring van der Waals metal contacts onto transition metal dichalcogenides. We measure an open-circuit voltage of 250 mV and a power conversion efficiency of 0.5% in Schottky-junction solar cells. To improve upon this efficiency, we next make carrier-selective contact solar cells, which employ wide bandgap semiconductors to selectively collect electrons on one side and holes on the other side of the absorber layer. We measure an open-circuit voltage of 520 mV and a power conversion efficiency greater than 2% in devices based on perovskite solar cell geometries, with PTAA and C60 as selective contact layers. We demonstrate that short carrier lifetimes limit the voltage in these solar cells to 750 mV, well below the detailed balance voltage limit. This motivates a more thorough understanding of the carrier dynamics at play, and we use a new pump-probe optical microscopy technique, stroboSCAT, to spatiotemporally track heat and carrier evolution in transition metal dichalcogenides. When paired with a kinetic model, we show that this technique can be used to measure lifetimes and other important material parameters even in materials with low radiative efficiencies.

We conclude by outlining future research directions towards achieving power conversion efficiencies greater than 10% in transition metal dichalcogenide solar cells.

Published Content and Contributions

Portions of this thesis have been drawn from the following publications:

1. **C. M. Went,** J. Wong, P. R. Jahelka, M. Kelzenberg, S. Biswas, M. S. Hunt, A. Carbone, H. A. Atwater, A new metal transfer process for van der Waals contacts to vertical Schottky-junction transition metal dichalcogenide photovoltaics. *Sci. Adv.* **5**, eaax6061 (2019). DOI: 10.1126/sciadv.aax6061
   C.M.W. *developed the metal transfer technique, fabricated the devices, performed the measurements, performed the simulations, and wrote the manuscript.*

2. **C. M. Went,** P. R. Jahelka, J. Wong, M. Mandigo-Stoba, H. A. Atwater, Achieving high open-circuit voltage in carrier-selective contact transition metal dichalcogenide photovoltaics. *In preparation* (2022).
   C.M.W. *conceived the project, fabricated the devices, performed the measurements, performed the simulations, and wrote the manuscript.*

3. H. L. Weaver, D. Jasrasaria, **C. M. Went,** J. Wong, H. A. Atwater, E. Rabani, N. S. Ginsberg, Spatiotemporally Resolving Heat and Exciton Transport in Few-Layer Transition Metal Dichalcogenides. *In preparation* (2022).
   C.M.W. *contributed to the fabrication of the samples, contributed to performing the temperature-dependent reflectance contrast measurements, contributed to the modeling, contributed to the interpretation of data, and contributed to the writing of the manuscript.*

4. **C. M. Went,** L. Schulte, I. Digdaya, CX Xiang, S. Ardo, H. A. Atwater, Technoeconomic Analysis of an Oceanwater Carbon Capture System Coupled with a Chemical Kinetics Model of Steady-State Rates of CO_2 Extraction. *In preparation* (2022).
   C.M.W. *contributed to the idea for the project, performed the technoeconomic analysis, and wrote the manuscript.*

Additional published content related to this thesis includes the following publications:

5. M. M. Potter, M. E. Phelan, P. Balaji, P. Jahelka, H. C. Bauser, R. D. Glaudell, **C. M. Went,** M. J. Enright, D. R. Needell, A. Augusto, H. A. Atwater, R. G. Nuzzo, Silicon Heterojunction Microcells. ACS Appl. Mater. Interfaces **13**, 45600–45608 (2021). DOI: 10.1021/acsami.1c11122
   C.M.W. *contributed to the photocurrent measurements and provided input on the manuscript.*

6. Y.-R. Lin, W.-H. Cheng, M. H. Richter, J. S. DuChene, E. A. Peterson, **C. M. Went,** Z. Y. Al Balushi, D. Jariwala, J. B. Neaton, L.-C. Chen, H. A. Atwater, Band Edge Tailoring in Few-Layer Two-Dimensional Molybdenum Sulfide/Selenide Alloys. J.

Phys. Chem. C **124**, 22893–22902 (2020). DOI: 10.1021/acs.jpcc.0c04719
C.M.W. *contributed to the MOCVD growth of molybdenum disulfide and provided input on the manuscript.*

7. W.-H. Lin, W.-S. Tseng, **C. M. Went,** M. L. Teague, G. R. Rossman, H. A. Atwater, N.-C. Yeh, Nearly 90% Circularly Polarized Emission in Monolayer WS_2 Single Crystals by Chemical Vapor Deposition. ACS Nano **14**, 1350–1359 (2020). DOI: 10.1021/acsnano.9b05550
C.M.W. *contributed to the TRPL measurements and provided input on the manuscript.*

8. M. C. Sherrott, W. S. Whitney, D. Jariwala, S. Biswas, **C. M. Went,** J. Wong, G. R. Rossman, H. A. Atwater, Anisotropic Quantum Well Electro-Optics in Few-Layer Black Phosphorus. *Nano Lett.* **19**, 269–276 (2019). DOI: 10.1021/acs.nanolett.8b03876
C.M.W. *performed the Raman measurements and provided input on the manuscript.*

9. O. Ilic, **C. M. Went,** H. A. Atwater, Nanophotonic Heterostructures for Efficient Propulsion and Radiative Cooling of Relativistic Light Sails. *Nano Lett.* **18**, 5583–5589 (2018). DOI: 10.1021/acs.nanolett.8b02035
C.M.W. *contributed to the calculations, the simulations, the figures, and the writing of the manuscript.*

10. H. A. Atwater, A. R. Davoyan, O. Ilic, D. Jariwala, M. C. Sherrott, **C. M. Went**, W. S. Whitney, J. Wong, Materials challenges for the Starshot lightsail. *Nat. Mater.* **17**, 861–867 (2018). DOI: 10.1038/s41563-018-0075-8
All authors conceived the project and contributed equally, led by H.A.A. All authors performed calculations and wrote the manuscript.

Table of Contents

List of Figures

List of Tables

Chapter 1: Introduction

1.1 Light

Light is central to two themes of this thesis: the climate crisis and solar energy. Visible light is one form of an electromagnetic wave, or oscillating electric and magnetic fields that travel through space. Different types of electromagnetic waves can be equivalently described by their energy, wavelength, or frequency, since all are related by the equations:

$$E = \frac{hc}{\lambda} = hf$$

where E is energy, λ is wavelength, f is frequency, h is Planck's constant, and c is the speed of light (*1*). The electromagnetic spectrum is shown in Figure 1.

	Interaction with Matter	Energy (eV)	Frequency (Hz)	Wavelength (m)
Gamma Rays	*excitation of nuclei*	1 MeV (10^6 eV)	100 Ehz (10^{20} Hz)	1 pm (10^{-12} m)
X-Rays	*ejection of core electrons*	10 keV (10^4 eV)	1 Ehz (10^{18} Hz)	100 pm (10^{-10} m)
Ultraviolet	*ejection of valence electrons*	100 eV	10 PHz (10^{16} Hz)	10 nm (10^{-8} m)
Visible	*electron excitation*	1 eV	100 THz (10^{14} Hz)	1 μm (10^{-6} m)
Infrared	*molecular vibrations/phonons*	10 meV (10^{-3} eV)	1 THz (10^{12} Hz)	100 μm (10^{-4} m)
Microwaves	*molecular rotations*	100 μeV (10^{-6} eV)	10 GHz (10^{10} Hz)	1 cm (10^{-2} m)
Radio waves	*plasma oscillations*	1 μeV (10^{-6} eV)	100 MHz (10^8 Hz)	1 m

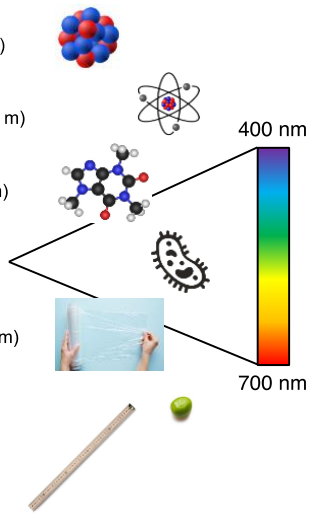

Figure 1. **The electromagnetic spectrum.**

FM radio, microwaves, 5G cell phone service, light from a lightbulb, and X-rays are all forms of electromagnetic waves. The wavelength of the radiation, or the distance between consecutive peaks of the wave, determines the type of radiation. FM radio transmits on electromagnetic waves with wavelengths of about a meter. Typical kitchen microwaves have wavelengths about the length of a credit card. 5G service propagates with wavelengths

about the diameter of a pea. Visible light coming out of a lightbulb has wavelengths that are much smaller, about one micron, or one-tenth the thickness of plastic wrap. Medical X-rays use electromagnetic waves with wavelengths over one thousand times smaller than that.

Everything that has a temperature is constantly emitting electromagnetic radiation. The temperature of the material determines the spectrum of the emitted electromagnetic radiation via the blackbody equation:

$$B_E(E,T) = \frac{2}{h^3c^2}\frac{E^3}{e^{E/k_BT} - 1}$$

where B is the spectral irradiance (power emitted, per unit area, per solid angle, per unit energy), E is the photon energy, and T is the temperature of the blackbody. Dividing the blackbody equation by the energy per photon E yields photons emitted per time rather than power emitted. Blackbody radiation is also called thermal radiation, and it is one of the mechanisms for heat transfer between two bodies. Figure 2 plots the blackbody spectrum at a few different temperatures.

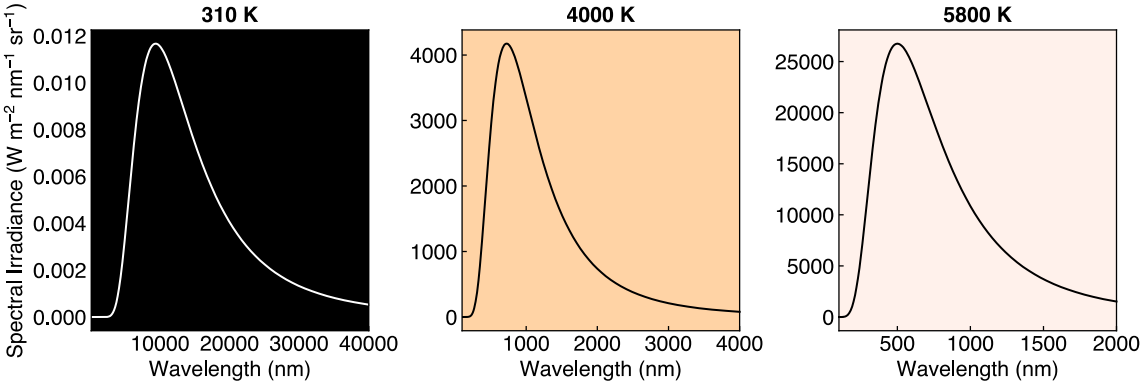

Figure 2. **Blackbody spectra with various blackbody temperatures.** Background color of each plot signifies the approximate color of the blackbody radiation as perceived by the human eye. (Black signifies that no color is visible, as the emission is in the infrared.)

When this emission overlaps significantly with the visible part of the electromagnetic spectrum, it is possible to convert this emission spectrum into a color as perceived by the human eye. The sun is a blackbody with a temperature of around 6000 K, so its spectrum

peaks around 500 nm, explaining why the sun emits visible white light. Halogen lightbulbs are blackbodies with temperatures around 4000 K, so their spectrum peaks around 700 nm, which is why they exhibit an orange glow. Humans are also blackbodies with temperatures around 310 K, so our spectrum peaks in the infrared, explaining why infrared cameras can detect the presence of humans or animals in the wild. The earth has a temperature around 290 K, so it also emits light in the infrared.

1.2 How Light Interacts with Materials

Whether an electromagnetic wave with a certain wavelength can travel through a material depends on whether that material absorbs light at that wavelength. For example, most materials do not absorb light at the 5G wavelength, which is why cell phone service can propagate over such long distances. Visible light, however, can be absorbed as it boosts electrons to higher energies in a material. Infrared light, which has wavelengths between those of visible light and microwaves, can be absorbed by molecules that use the energy to rotate and vibrate.

There are multiple equivalent descriptors of how a material interacts with light, including the complex refractive index $\tilde{n} = n + ik$, the dielectric constant $\varepsilon = \varepsilon_1 + i\varepsilon_2$, the complex optical conductivity $\tilde{\sigma} = \sigma_1 + i\sigma_2$, and the absorption coefficient α. They are all related by algebraic transformations, and they can each be useful in different settings (*2*). Knowing the real or complex part of any of the optical constants is sufficient to know the other part (complex or real), because the two are related by causality through the Kramers-Kronig relations. Given one of these optical constants of a material, we can calculate the reflection, absorption, and transmission through a slab of that material of a given thickness using transfer matrix calculations (*3*).

To understand the microscopic underpinnings of a material's optical response, it is easiest to begin with the absorption coefficient, as that is most intuitively related to physical processes within the material. Figure 3 shows a few of these physical processes and how they contribute to the absorption coefficient. In the infrared (1–100 μm), electromagnetic waves can transfer their energy into vibrations in the lattice of a solid, or phonons, leading to peaks in the absorption coefficient. Similarly, for a gas or a liquid, electromagnetic

waves can be absorbed into molecular rotations and vibrations. Free carrier absorption (or equivalently, Drude or intraband absorption) dominates the optical response of metals, where electromagnetic waves can be absorbed into oscillations of the free electrons in the material. In semiconductors and insulators, which have a gap in the allowed energy states for electrons in the material, electromagnetic waves with energies greater than the bandgap can provide the energy to boost an electron in the lower energy states (the valence band) to the higher energy states (the conduction band).

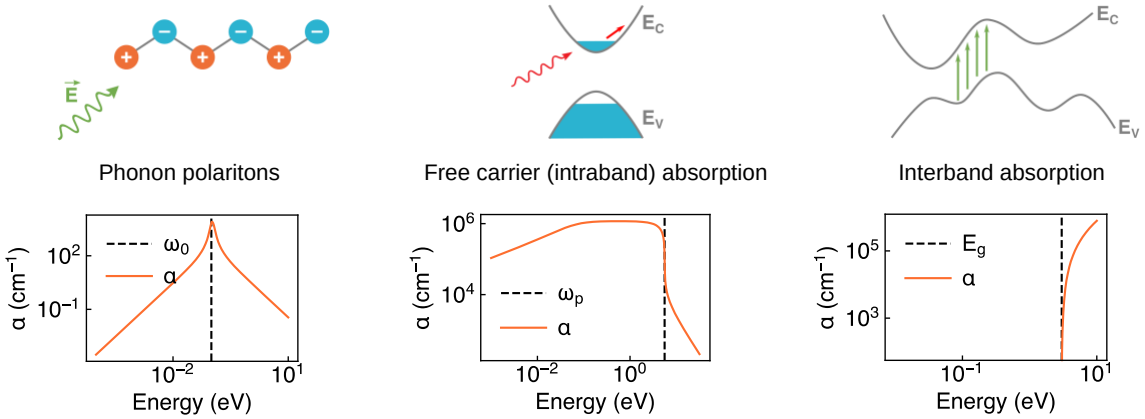

Figure 3. **Microscopic underpinnings of the absorption coefficient of a material**.

Summing these effects together for any given material yields the material's absorption coefficient (Figure 4).

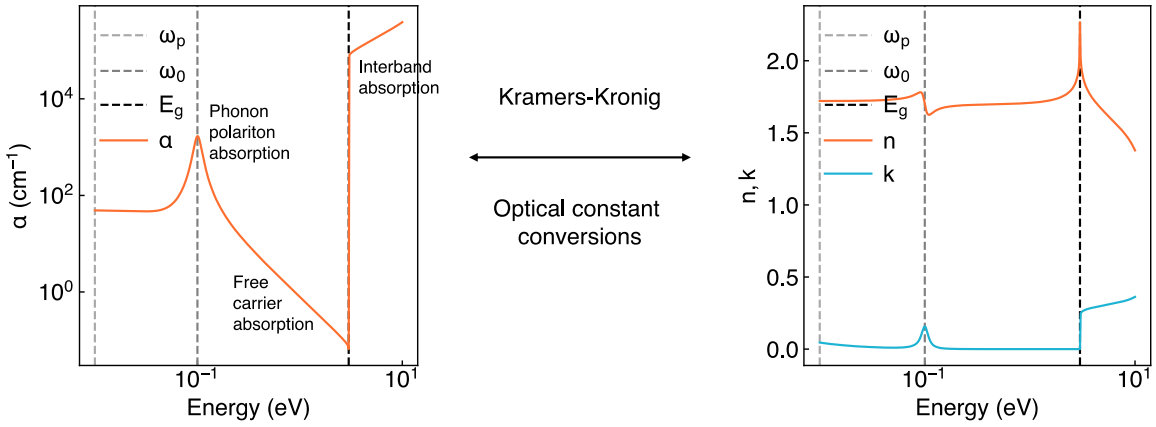

Figure 4. **Summing together the various microscopic contributions yields the optical response of the material**. Here, we calculate the absorption coefficient α for a toy model of a semiconductor, and we convert to the complex refractive index $\tilde{n} = n + ik$ using optical constant conversions and the Kramers-Kronig relations.

With the algebraic transformations and Kramers-Kronig relations described above, it is possible to calculate, for example, the complex refractive index starting from just the absorption coefficient. Because of Kirchhoff's law of thermal radiation, which describes optical reciprocity, the absorptivity of a material equals it emissivity. So, for any real material, multiplying the idealized blackbody spectrum by the material's absorptivity/emissivity yields the real emission spectrum of that material.

1.3 How Climate Change Works

Many people learn about how climate change works through the simple analogy of greenhouse gases forming a blanket around the earth to insulate it and trap the sun's radiation—more greenhouse gases equals a thicker blanket. With an understanding of both blackbody radiation and how materials interact with light, it is possible to add more detail to this description of climate change.

If we treat the sun as a 5800 K blackbody and integrate over the spectrum in Figure 2, taking into account that the solid angle of the sun as seen from the earth is 6.8×10^{-5} steradians, the solar radiation that hits the top of the earth's atmosphere is about 1380 W/m^2. This assumes that the earth is a disk facing the sun with an area $A = \pi r^2$, so to calculate the average solar radiation over the entire surface area of the earth $SA = 4\pi r^2$, we divide by 4 to get about 345 W/m^2. To be in thermal equilibrium, the earth must reradiate the same amount of power back out in all directions. Using the Stefan-Boltzmann law that relates emitted power to the temperature of the blackbody, and taking into account that the earth reflects about 30% of the power it receives directly back to space, we can calculate that the earth's temperature would be about 255 K, or 0ºF.

Gases in the atmosphere keep the earth at a warmer temperature than that chilly 0ºF via the greenhouse effect. The greenhouse gases consist of water vapor, CO_2, methane, nitrous oxide, and ozone. While these molecules are mostly transparent to visible light, they can absorb infrared light into molecular vibrations and rotations. The absorption spectrum of one of the most prominent greenhouse gases, CO_2, is shown in Figure 5, overlaid with the blackbody spectra of the sun and the earth. When sunlight (approximately a blackbody

spectrum at 5800 K, peaking at 500 nm in the visible) is incident on the atmosphere, it mostly passes through to earth. When the earth reradiates back to space (approximately a blackbody spectrum at 290 K, peaking at 10 μm in the infrared), some of that infrared radiation is absorbed by greenhouse gases in the atmosphere. The greenhouse gases reemit that infrared light in all directions, given that absorptivity equals emissivity, and that the temperature of the atmosphere is close to the earth's temperature. Half is emitted to space, and half comes back to earth, raising the earth's temperature to around 290 K.

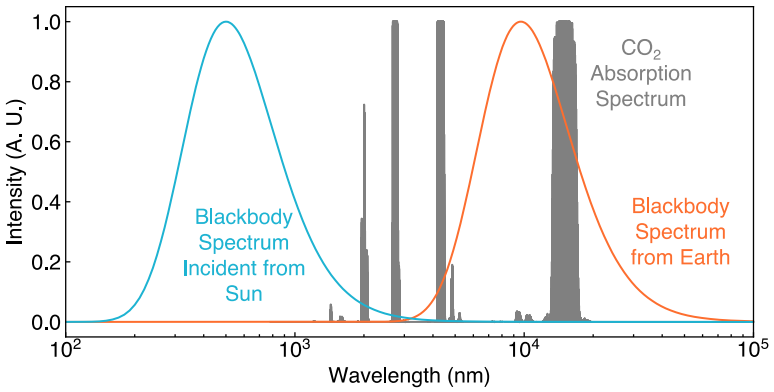

Figure 5. **Mechanism for climate change**. CO_2 in the atmosphere is transparent to sunlight in the visible range incident on earth, but it can absorb and reradiate thermal radiation leaving earth. Blackbody spectra are normalized to their maximum values (in reality, the sun's blackbody radiation is much more intense than the earth's). CO_2 spectrum from (*4*).

An idealized model of the greenhouse effect is presented in (*5*), which considers the temperature of the sun, the earth, and the atmosphere, and calculates the flux balance and resulting equilibrium temperatures between the three. By solving for the atmosphere's emissivity, the model arrives at the earth's surface temperature of about 288 K. By integrating the emissivity spectrum of CO_2 in the atmosphere with the earth's blackbody emission spectrum, it is possible to calculate the radiative forcing (or increase in radiated power back to earth) resulting from a doubling of CO_2. The idealized model then calculates that if the CO_2 concentration in the atmosphere doubles, the earth's temperature rises by ~2.5 K. Thus, with the relatively simple blackbody physics presented here, it is possible to predict that an increase in CO_2 concentration causes an increase in the earth's temperature.

More sophisticated climate models, of course, predict the same effect with higher accuracy. These models also can predict the effects of an increase in earth's surface temperature on

our climate, and they show that limiting warming to 1.5ºC rather than 2ºC yields shockingly significant societal benefits. To select just a few, with an extra half degree of warming: 23% more people worldwide will be exposed to severe heat waves; coral reefs go from frequent mass mortalities to mostly disappearing; and roughly double the number of species of plants and animals will lose more than half of their range (*6*). While limiting warming by *any* amount will yield societal benefits (there is no "point of no return" where taking action becomes futile), limiting warming to 1.5ºC is collectively agreed upon by climate scientists to be an important target (*6*).

1.4 The Scale of the Problem

Humans emit about 35 billion tons of CO_2 per year globally, and the United States emits about 6.5 billion of those tons (*7*, *8*). In the US, this breaks down to 30% from transportation, 25% from electricity, 23% from industry, 13% from commercial/residential (e.g. fossil fuel-based heating of buildings), and 10% from agriculture (*8*). Figure 6 pictorially puts this quantity of emitted CO_2 into context.

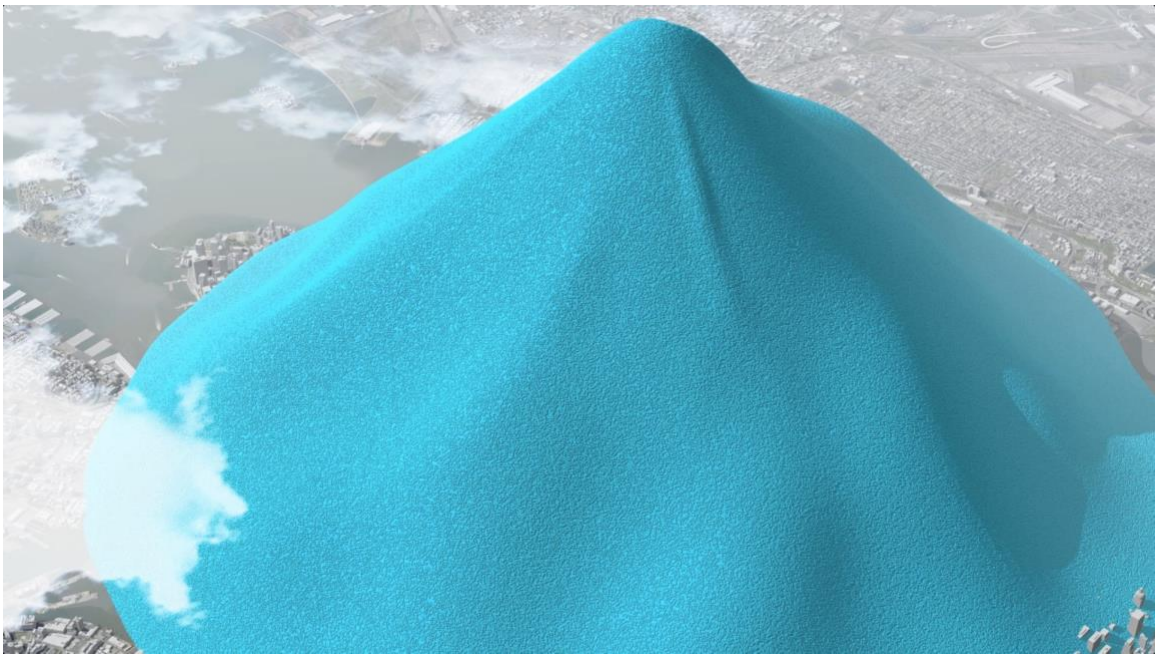

Figure 6. **The volume of a year of New York City's CO_2 emissions.** Each blue sphere represents 1 ton of CO_2, and is sized to be the actual volume of a ton of gaseous CO_2. New York city emitted 54 million tons of CO_2 in 2010. Figure from (*9*).

The 35 billion tons of CO_2 emitted globally per year weigh significantly more than the steel produced by the global steel industry each year (2 billion tons) and the cement produced by the global cement industry each year (4 billion tons) (*10*, *11*). In fact, the CO_2 emitted each year weighs more than all other material flows through the global economy, *combined* (*12*).

Given that the earth's atmosphere weights about 5×10^6 billion tons, we can estimate that we are adding about 8 ppm CO_2 by mass to the atmosphere each year, which translates to about 5 ppm by volume when considering the masses of different atmospheric gases. In reality, measurements or more sophisticated climate models are needed to calculate the change in CO_2 concentration per year, and the actual change is closer to 2.5 ppm (*13*). As will be discussed in Appendix A, the ocean absorbs as much as 40% of anthropogenic CO_2 emissions, explaining some of the discrepancy.

The entire global ecosystem—including all of the trees and plants on the planet—pulls about 2 billion tons of CO_2 per year from the atmosphere (*12*). If we wanted to capture all the CO_2 that we emit each year, we would have to create a CO_2-sucking industry about *twenty times* more effective at sucking CO_2 out of the atmosphere than all of the earth's plants. Thus, we need to dramatically reduce our global CO_2 emissions to have any hope of limiting warming to 1.5ºC.

1.5 The Scale of the Solution

To achieve a 1.5ºC future, the IPCC has shown that we need to reach net-zero CO_2 emissions worldwide by 2050 (*6*). Experts are coming to a consensus on the main steps needed to reach net-zero: 1) electrify everything we can (buildings, transportation, and some of industry); 2) switch electricity production to renewables; and 3) rely on a mix of hydrogen, carbon capture, and other solutions for the remaining ~10% of harder-to-decarbonize emissions. There have been many excellent efforts to model trajectories to net-zero by 2050, and we will draw on work from the REPEAT Project here (*14*). Figure 7 shows primary energy and electricity supply and demand in the present day, and projected out to 2030 and 2050 in a net-zero scenario.

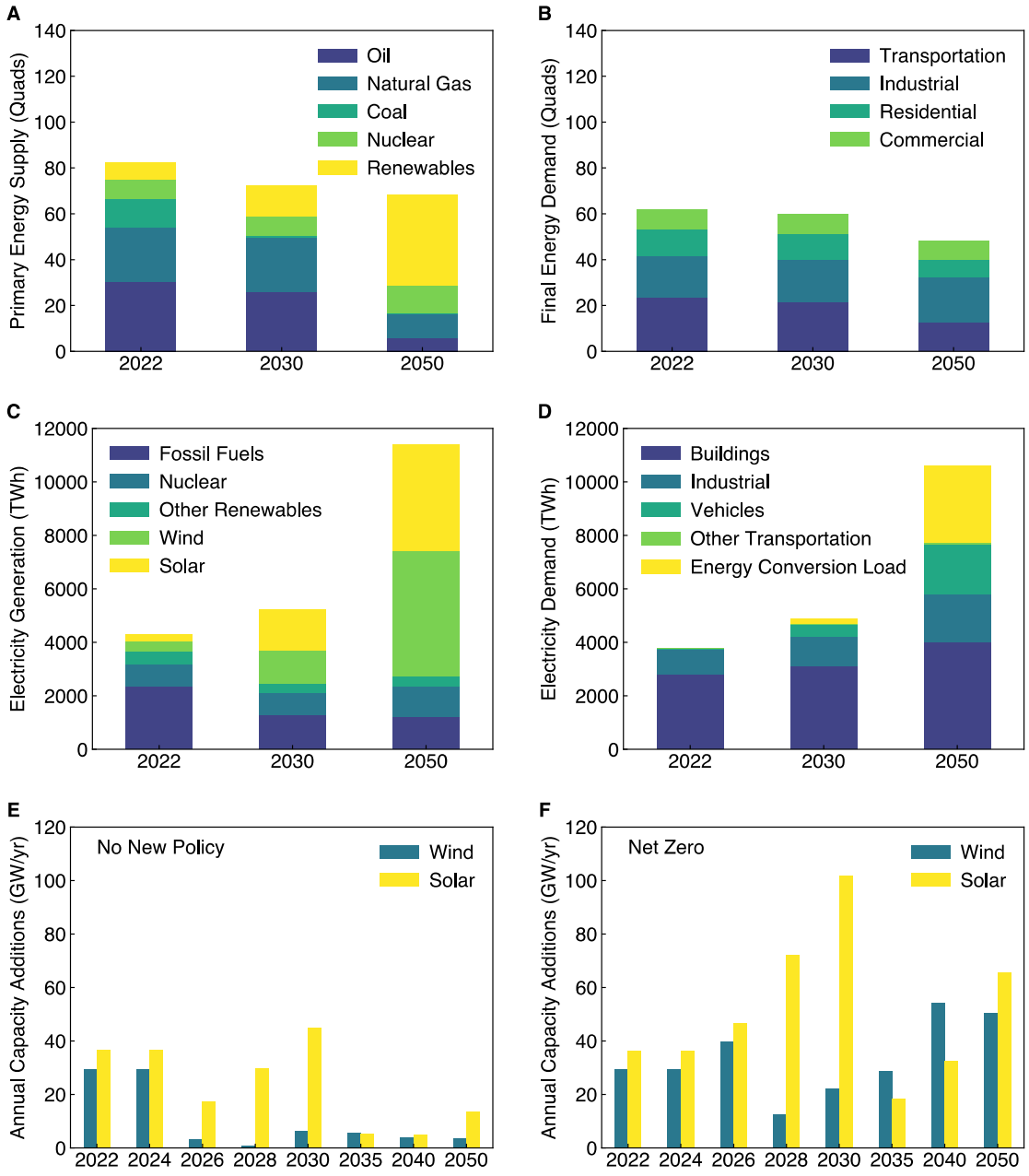

Figure 7. **A pathway to net-zero CO_2 emissions in 2050**. (**A**) Primary energy supply by source, present-day and projected out to net-zero in 2050. (**B**) Final energy demand by sector. (**C**) Electricity generation by source. (**D**) Electricity demand by sector. (**E**) Annual capacity additions of wind and solar, assuming no new policy. (**F**) Annual capacity additions of wind and solar in an optimized net-zero pathway. Data from the REPEAT Project (*14*).

The primary energy supply in the US currently equal to 80 exajoules (80 EJ = 80 × 10^{18} J ≅ 80 quads) (Figure 7A). The final energy demand is currently equal to ~60 EJ, and the 20

EJ lost between primary and final energy are mostly due to inefficiencies in burning fossil fuels to generate electricity (Figure 7B). Of the 80 EJ of primary energy, oil accounts for ~30 EJ, natural gas accounts for ~20, and coal, nuclear, and renewables each account for ~10 (Figure 7A). Of the 60 EJ of final energy demand, ~20 EJ each are in the industrial and transportation sectors, and ~10 each are in the residential and commercial sectors (Figure 7B).

The first step to achieving net zero by 2050, electrifying everything, has the dual benefit of: 1) increasing the efficiency with which we use energy, and 2) relying on increasingly clean energy sources (Figure 7C). Electric cars use energy with an efficiency of ~70% (90% battery efficiency × 80% drivetrain efficiency), compared to ~30% efficiency in internal combustion engines (*12*). Electrifying three quarters of our transportation could therefore reduce final energy demand by as much as 10 EJ, shrinking the transportation sector final energy demand to 10 EJ (Figure 7D). Similarly, heat pumps are at least three times as energy-efficient for heating and cooling homes as gas furnaces. Electrifying buildings could shrink the final energy demand for the residential and commercial sectors substantially. As we carry out the second step of switching to renewables, the benefits compound, because everything that runs on electricity is as clean as the grid.

In a high electrification scenario, our final energy demand could drop from our current 60 EJ to 50 EJ in 2050 (Figure 7B). At the same time, electricity demand could more than double, increasing from 4,000 TWh now to 10,000 TWh (roughly 35 EJ, as 1 EJ ≅ 300 TWh) in 2050 (Figure 7D). Electricity from renewable energy could provide more than two-thirds of our energy by 2050, in contrast to fossil fuels providing more than two-thirds of our energy today (Figure 7A).

Last year, wind provided ~340 TWh of US yearly electricity demand, and solar provided ~130 TWh. To meet renewable electricity demand in a net-zero future, by 2050, wind and solar would each need to supply ~4000 TWh of electricity. For solar with a 25% capacity factor, 4000 TWh annually translates to 1.8 TW of installed capacity, and for wind with a 35% capacity factor, this translates to 1.3 TW of installed capacity (1 TWh of *energy* per year ≅ 0.1 GW of continuous *power* flow, on average). Between now and 2050, we need

to install 60 GW of solar each year and 40 GW of wind each year on average (Figure 7E–F). For context, 10 GW of solar and 15 GW of wind were installed in 2020. These 60 GW and 40 GW installation rates are similar to the installation rates necessary for the sustainable replacement rate of these technologies in 2050, assuming a 30 year lifetime for both technologies. However, to avoid overshooting and oversizing the industry, then decommissioning manufacturing plants, we must scale to those installation rates within the decade. This places extreme demands on the scaling of the wind and solar industries. It also requires large policy-driven government investments in scaling up manufacturing capacity quickly—many studies show that market forces alone will not get us there (*14*).

1.6 The Case for Ultrathin Solar Cells

With record lab efficiencies greater than 26%, silicon has continued to dominate the photovoltaics market. Silicon is earth-abundant, stable, and nontoxic, and it is already produced at scale for the electronics industry. However, the upfront cost required to build a silicon solar cell manufacturing plant is quite large (*15*). This is mostly due to the high capital expense (CapEx) of many of the processing steps involved in making a silicon wafer, including trichlorosilane production, Siemens CVD, and Czochralski growth. This high CapEx, combined with low profit margins, places limits on how quickly the solar industry can scale independently (*15*). Achieving a 6x increase in annual installed capacity within the decade will therefore be challenging without an infusion of government capital.

Due to an indirect bandgap and resultant low absorption per unit thickness, silicon solar cells must be on the order of 100 μm thick to absorb the full incident solar spectrum. Thinner solar cells have many advantages: 1) they require less raw material, and therefore can have lower CapEx, as semiconductor processing equipment is expensive; 2) they pose less stringent requirements for material quality, as impurity *concentrations* can be higher (and still yield the same total *number* of impurities as in a thicker solar cell) and mobilities can be lower (since carriers with smaller diffusion lengths can reach the contacts); and 3) they weigh less, rendering them useful for applications that require lightweight solar cells. It therefore could hypothetically be desirable to find a new material that would enable high-efficiency ultrathin photovoltaics.

Realistically, it is unlikely that a new material for ultrathin solar cells will beat silicon in the race to 60 GW per year of installed capacity by 2030, based on the maturity and existing scale of the silicon industry. Silicon has a significant head start in the race. However, a low CapEx ultrathin solar cell could be beneficial in industries where high specific power, or power per unit weight, is required, such as building-integrated, vehicle-integrated, or aerospace solar.

1.7 Transition Metal Dichalcogenides for Ultrathin Solar Cells

Two-dimensional (2D) semiconducting transition metal dichalcogenides (TMDs), including MoS_2, WS_2, $MoSe_2$, and WSe_2, are particularly promising for high-specific-power photovoltaics (Figure 8). With absorption coefficients 1–2 orders of magnitude higher than conventional semiconductors, monolayer (<1 nm thick) TMDs can absorb as much sunlight as about 15 nm of GaAs or 50 nm of Si (*16*). Due to their layered structure and out-of-plane van der Waals bonding, TMDs have intrinsically passivated surfaces with no dangling bonds and can form heterostructures without the constraint of lattice matching.

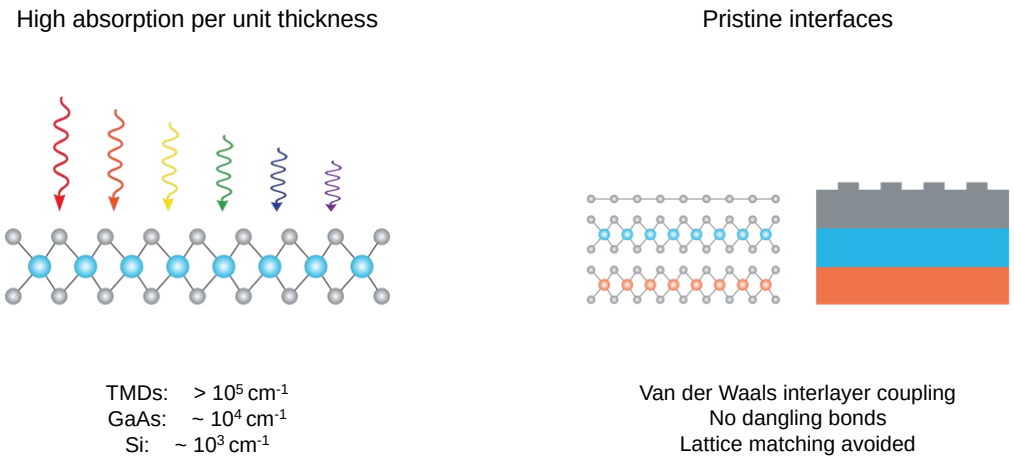

Figure 8. **Advantages of transition metal dichalcogenides for ultrathin photovoltaics**.

In their monolayer form, TMDs have direct bandgaps at ideal energies for tandem solar cells with silicon, and high photoluminescence quantum yields, especially upon passivation (*17–19*). In their multilayer form, TMDs have indirect bandgaps and lower photoluminescence quantum yields, but also smaller exciton binding energies and ideal

bandgaps for single-junction solar cells approaching the detailed balance efficiency limit (*20*). Both multilayer and monolayer TMDs can achieve near-unity broadband absorption in the visible range, though the necessary geometry is much simpler for multilayer TMDs (*21*, *22*). The theoretical maximum power conversion efficiency achievable for multilayer and monolayer single-junction solar cells is similar, due to the tradeoff between bandgap energy and photoluminescence quantum yield (*23*).

Different carrier collection techniques have been explored in multilayer and monolayer TMD photovoltaics. Monolayer TMD solar cells usually collect carriers laterally, as tunneling dominates transport in vertical monolayer devices. The carrier-separating junctions formed in monolayer TMD solar cells include p-n junctions defined by split-gate electrodes (*24–26*), p-n junctions defined by type-II band alignment between two TMDs (*27–30*), p-n junctions defined by chemical doping (*31*), and Schottky junctions (*32*, *33*). In multilayer TMD solar cells, both lateral and vertical devices have been fabricated. Internal quantum efficiency (IQE) >70% has been demonstrated in 3 nm MoS_2/9 nm WSe_2 vertical p-n junctions (*34*). AM1.5G power conversion efficiencies of 0.4% and 2.8% have been achieved in ultrathin (11 nm) (*35*) and thicker (120 nm) (*36*) chemically-doped vertical p-n junctions of MoS_2, respectively, and AM1.5G power conversion efficiency 0.7% has been achieved in lateral Schottky junctions with a 3-nm-thick TMD (*37*). Recently, a V_{OC} of 680 mV has been observed in MoO_x-doped WS_2 solar cells (*38*), and a specific power of 4 W/g and efficiency of 5% has been observed in Schottky-junction WSe_2 solar cells with ~100-nm-thick active layers on lightweight and flexible substrates (*39*).

1.8 How Solar Cells Work

A solar cell converts electromagnetic power from the sun into electrical power. Electrical power equals current times voltage, so a solar cell must generate both a high current and a high voltage when illuminated with sunlight. Solar cells are made from semiconductors, which have an energy bandgap (or a gap in the allowed energy states for electrons within the material) that is comparable to the energy of visible light from the sun. The lower lying energy states (the valence band) are full, and electrons in those states are therefore unable to move collectively in one direction and generate a current. But when these electrons are

excited with enough energy (e.g. when they absorb sunlight), they enter the higher-energy conduction band, which has empty energy states and can sustain a current. A solar cell can therefore supply both current (from the flow of electrons through the conduction band) and voltage (from the energy those electrons gain when they absorb light and enter a higher energy state).

At equilibrium, the Fermi level for a semiconductor lies in the bandgap, and the only electrons in the conduction band are those that are thermally excited. This can be equivalently thought of as thermal excitation from the 300 K blackbody of the environment, or the tailing off of the Fermi-Dirac distribution centered around the Fermi level into the conduction band. After excitation, the electrons quickly thermalize with the lattice and relax to the conduction band edge (within ~1 ps) before recombining (usually on the order of ~1 μs). After thermalization, but before recombination, they can be described by a 300 K Fermi-Dirac distribution, but with a different Fermi level, called a quasi-Fermi level. The number of electrons in the conduction band can be calculated by integrating the product of the Fermi-Dirac distribution and the density of states in the conduction band to yield:

$$n = N_C e^{-\frac{E_C - E_{FC}}{k_B T}}$$

where n is the electron concentration in the conduction band, N_C is the effective density of states in the conduction band, E_C is the conduction band energy, and E_{FC} is the quasi-Fermi level for electrons (equal to the Fermi level if the semiconductor is in equilibrium). A similar expression can be derived for holes (the "negative space" left behind by electrons, which behave like positively charged particles) in the valence band:

$$p = N_V e^{-\frac{E_{FV} - E_V}{k_B T}}$$

The product of these two expressions is equal to:

$$np = N_C N_V e^{\frac{-E_g}{k_B T}} e^{\frac{E_{FC} - E_{FV}}{k_B T}} = n_i^2 e^{\frac{E_{FC} - E_{FV}}{k_B T}}$$

The quasi-fermi level splitting, $E_{FC} - E_{FV}$, dictates the maximum electrochemical energy that can be extracted from the solar cell, which is proven nicely in (*40*). So, the maximum voltage of a solar cell with perfect carrier collection is given by:

$$qV = E_{FC} - E_{FV}$$

Once excited, electrons and holes can either recombine radiatively (via emission of a photon with the energy of the bandgap), or nonradiatively (via phonon emission). The product of the electron and hole concentrations is proportional to the rate of radiative recombination:

$$R_{rad} = k_{rad} np$$

where R_{rad} is the rate of radiative recombination per volume, per time (in $cm^{-3}\ s^{-1}$), and k_{rad} is the radiative recombination coefficient (in $cm^3\ s^{-1}$). When thinking about what is happening in an entire solar cell rather than a small volume within it, it is useful to convert from rates to photon current densities by integrating over the thickness of the material. This yields:

$$j_{emit} = k'_{rad} np$$

where j_{emit} is the emitted photon current density from the surface of the solar cell in units of photons emitted per area per time ($cm^{-2}\ s^{-1}$) and k'_{rad} is effectively k_{rad} integrated over thickness (in $cm^4\ s^{-1}$). Note that in reality, this equation is an approximation of the generalized Planck's law, which is derived in detail in Ref (*40*).

It is possible to derive the maximum efficiency for a planar, single-junction solar cell with no optical concentration from purely thermodynamic considerations (Figure 9). This is called the detailed balance efficiency limit, and a derivation follows (*20*). The three key assumptions of the detailed balance efficiency limit are 1) that the solar cell absorbs all photons above its bandgap and none below it (step-function absorption), 2) that there is no nonradiative recombination and any electron hole pairs that are not collected as current therefore recombine radiatively (unity radiative efficiency), and 3) that all generated

electron-hole pairs are collected at the maximum possible voltage represented by the quasi-Fermi level splitting.

We need two final pieces of information for this derivation. The first is the blackbody radiation emitted by a planar solar cell:

$$BB_{cell} = \frac{2\pi}{h^3c^2}\frac{E^2}{e^{E/k_BT_{cell}} - 1}\,dE$$

where BB_{cell} is the photons emitted by the solar cell per unit time, area, and energy, T_{cell} is 300 K, and π is the solid angle for emission from a planar surface into a hemisphere. The second is the blackbody radiation emitted by the sun as seen by earth:

$$BB_{sun} = \frac{2\Omega_{sun}}{h^3c^2}\frac{E^2}{e^{E/k_BT_{sun}} - 1}\,dE$$

where BB_{sun} is the photons emitted by the sun towards the earth per unit time, area, and energy, T_{sun} is 5800 K, and Ω_{sun} is the solid angle subtended by the sun as seen by earth, or 6.8×10^{-5} sr. For more accuracy, we can also input the actual measured AM1.5G spectrum of the sun in place of BB_{sun}.

In equilibrium, the solar cell is constantly exchanging thermal radiation with the 300 K environment. The emitted photons must equal the absorbed photons, which gives:

$$j_{Emit} = j_{Abs} = \int a(E)BB_{cell}(E)dE = \int_{E_g}^{\infty} BB_{cell}(E)dE$$

where $j_{Emit/Abs}$ represent a photon current density and $a(E)$ is the absorption of the solar cell (generally calculated from the absorption coefficient using the Beer-Lambert law, but equal to a step function in the detailed balance limit). From $j_{emit} = k'_{rad}np$, we now know that $k'_{rad}n_i^2 = \int_{E_g}^{\infty} BB_{cell}(E)dE$, since the equilibrium electron-hole product is n_i^2.

The solar cell is out of equilibrium with its environment when it is illuminated, or when a voltage is applied. (Note that steady-state is different from equilibrium—an illuminated solar cell is still at steady-state.) Out of equilibrium, the emitted photons no longer equal

the absorbed photons. However, we still have $j_{emit} = k'_{rad} np$, and we know k'_{rad} from what happens at equilibrium. So, the emitted photon current density out of equilibrium is:

$$j_{Emit} = \frac{np}{n_i^2} \int_{E_g}^{\infty} BB_{cell}(E) dE = e^{\frac{E_{FC} - E_{FV}}{k_B T}} \int_{E_g}^{\infty} BB_{cell}(E) dE$$

where T is the cell temperature of 300 K. The absorbed photon current density is equal to the photons absorbed from both the sun and the 300 K environment:

$$j_{Abs} = \int_{E_g}^{\infty} BB_{cell}(E) dE + \int_{E_g}^{\infty} BB_{sun}(E) dE$$

With the assumption that every absorbed photon creates an electron, we can switch to units of current density (e.g. in mA/cm^2) by multiplying the photon current density by the charge of an electron q. We then arrive at the definitions:

$$J_0 = q \int_{E_g}^{\infty} BB_{cell}(E) dE$$

$$J_L = q \int_{E_g}^{\infty} BB_{sun}(E) dE$$

We can also use $qV = E_{FC} - E_{FV}$ to replace the quasi-Fermi level splitting with the voltage. Finally, we apply the continuity principle, which says that every electron-hole pair that is created by a photon either recombines, emitting a photon, or is collected as current:

$$J = J_{abs} - J_{emit} = -J_0 \left(e^{\frac{qV}{k_B T}} - 1 \right) + J_L$$

This equation represents the J-V curve for an ideal solar cell, plotted in Figure 9. By changing the bandgap in the integration limits in the definitions of J_0 and J_L, we can calculate the J-V curve for a solar cell as a function of bandgap. Dividing the maximum power point of each J-V curve by the incident power from the sun yields the maximum efficiency as a function of bandgap, as shown in Figure 9A. A good solar cell will have a high short-circuit current (J_{SC}), open-circuit voltage (V_{OC}), and fill factor (FF, the

squareness of the I-V curve), and the product of the three is the power conversion efficiency (Figure 9B).

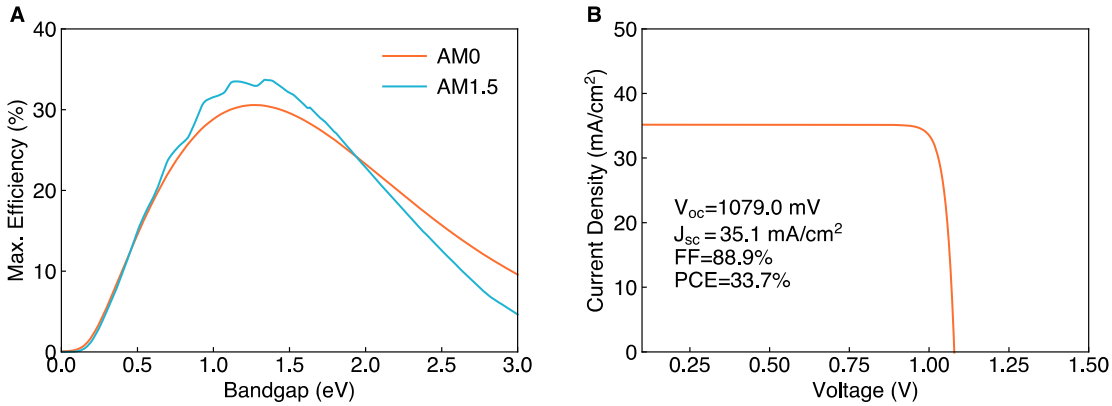

Figure 9. **Detailed balance efficiency limit.** (**A**) Maximum efficiency as a function of bandgap calculated from detailed balance. (**B**) Ideal J-V curve for a maximum efficiency solar cell, with a bandgap of 1.4 eV.

To summarize, there are three essential processes in a solar cell, and each corresponds to a materials requirement for any new photovoltaic material (Figure 10).

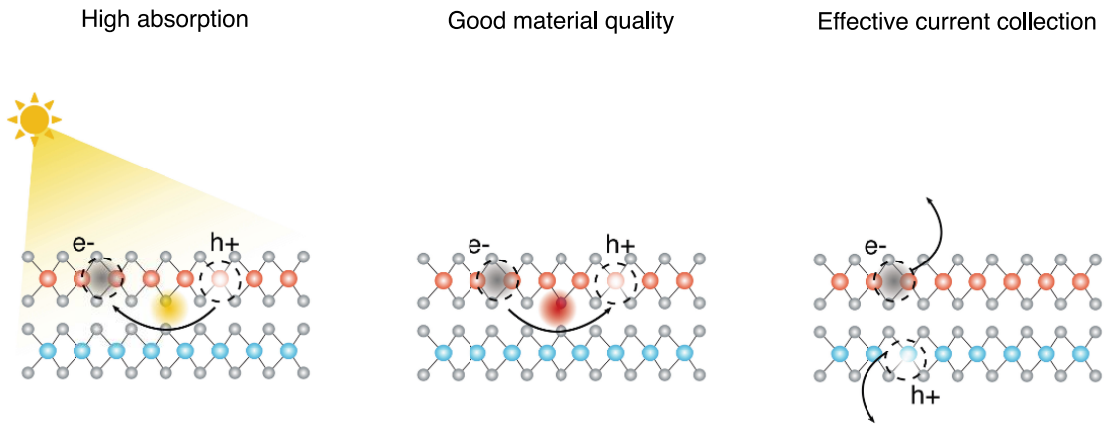

Figure 10. **Materials requirements for an efficient solar cell**.

First, a solar cell absorbs light, exciting electrons into the conduction band. A new solar material must therefore have high absorption, which translates to a high current density. Second, a high population of electrons in the conduction band and holes in the valence band must be sustained to create a large quasi-Fermi level splitting and a high voltage. A

new solar material must therefore have a low defect concentration, leading to a long lifetime or a high radiative efficiency. Third, to propel a current through an external circuit, there must be some gradient or symmetry-breaking that tells the electrons which direction to flow. A new solar material must therefore be designed with an effective carrier collection mechanism (whether a Schottky junction, a p-n junction, or a selective contact geometry), which affects current, voltage, and efficiency. This thesis will explore all three of these materials requirements for TMD solar cells.

1.9 The Scope of this Thesis

In Chapter 1, we provide some of the necessary background information for understanding this thesis, including the physics of electromagnetic waves and the physics of solar cells. We demonstrate the scale of the problem posed by the climate crisis, and the scale of the solution. We introduce 2D TMDs, and explain why they are particularly promising for ultrathin solar cells.

Chapter 2 focuses on the simplest type of solar cell: a Schottky-junction TMD solar cell. We develop a process for gently transferring metal contacts onto TMDs to avoid Fermi-level pinning, and we demonstrate that solar cells with transferred metal contacts perform significantly better than solar cells with evaporated metal contacts. These Schottky-junction TMD solar cells achieve one-sun power conversion efficiencies of 0.5%.

In Chapter 3, we aim to increase efficiency by fabricating the best type of solar cell: a carrier-selective TMD contact solar cell. The highest efficiency silicon and perovskite solar cells use this carrier-selective contact geometry. We demonstrate the transferability of perovskite carrier-selective contacts to TMDs by using PTAA and C60 as selective contacts for TMD solar cells. These solar cells achieve one-sun power conversion efficiencies of 2.4%. Through measurements and calculations, we demonstrate that the short lifetimes in TMDs limit the maximum achievable voltage in undoped TMD solar cells to 750 mV.

Motivated by this finding, Chapter 4 focuses on understanding the kinetics in illuminated TMDs using stroboSCAT, a new pump-probe optical microscopy technique. We show that

this technique, combined with a kinetic model, can be used to extract carrier lifetimes, even in materials with low radiative efficiencies. We demonstrate that exciton-exciton annihilation can have a significant effect even in multilayer samples and that heat can dominate transient optical spectra.

Chapter 5 gives an outlook for TMD solar cells and suggests future research directions.

Finally, Appendix A presents a self-contained project on technoeconomic analysis of an oceanwater carbon capture system. Appendices B and C provide detailed experimental methods and calculations. Appendix D presents cover art generated for an issue of *Nature Materials*.

Chapter 2: Vertical Schottky-Junction Transition Metal Dichalcogenide Photovoltaics Enabled by a New Metal Transfer Process

Two-dimensional transition metal dichalcogenides are promising candidates for ultrathin optoelectronic devices due to their high absorption coefficients and intrinsically passivated surfaces. To maintain these near-perfect surfaces, recent research has focused on fabricating contacts that limit Fermi-level pinning at the metal-semiconductor interface. Here, we develop a new, simple procedure for transferring metal contacts that does not require aligned lithography. Using this technique, we fabricate vertical Schottky-junction WS_2 solar cells with Ag and Au as asymmetric work function contacts. Under laser illumination, we observe rectifying behavior and open-circuit voltage above 500 mV in devices with transferred contacts, in contrast to resistive behavior and open-circuit voltage below 15 mV in devices with evaporated contacts. One-sun measurements and device simulation results indicate that this metal transfer process could enable high-specific-power vertical Schottky-junction transition metal dichalcogenide photovoltaics, and we anticipate that this technique will lead to advances for two-dimensional devices more broadly.

2.1 Introduction

Two-dimensional (2D) semiconducting transition metal dichalcogenides (TMDs), including MoS_2, WS_2, $MoSe_2$, and WSe_2, are promising for many optoelectronic applications, including high-specific-power photovoltaics (*17*, *18*, *23*, *41*, *42*). With absorption coefficients 1–2 orders of magnitude higher than conventional semiconductors, monolayer (<1 nm thick) TMDs can absorb as much visible light as about 15 nm of GaAs or 50 nm of Si (*16*). Both multilayer and monolayer TMDs can achieve near-unity broadband absorption in the visible range (*21*, *22*). Due to their layered structure and out-of-plane van der Waals bonding, TMDs have intrinsically passivated surfaces with no dangling bonds and can form heterostructures without the constraint of lattice matching.

To take advantage of the intrinsically passivated surfaces of TMDs, gentle fabrication techniques are needed to form metal contacts without damaging the underlying semiconductor. A number of new contact techniques have been presented recently, including one-dimensional edge contacts (*43*), via contacts embedded in hBN (*44*), slowly-deposited In/Au contacts (*45*), and 2D metals (*46*). Recently, Liu *et al* have shown that transferring rather than evaporating metal contacts onto TMDs can yield interfaces with no Fermi-level pinning, where the Schottky barrier height can be predicted by the ideal Schottky-Mott rule (*32*). Their work demonstrates the utility of transferring an arbitrary three-dimensional metal onto a 2D material, forming a nondamaging van der Waals contact. However, this technique requires a final aligned lithography step to expose the contact under the polymer used for transfer, which limits its scalability (*32*).

To date, the above techniques for gentle contact fabrication have been applied to device geometries where carriers are collected laterally rather than vertically. Laterally-contacted TMD devices utilize contact spacing on the order of 5 μm, which would be prohibitively expensive to fabricate for large-area low-cost photovoltaic devices. Though laterally-contacted devices are important for electronic applications, such as field-effect transistors, vertically-contacted devices are preferable for optoelectronic applications that require scalable photoactive areas, such as solar cells. Van der Waals contacts could have an even greater advantage for these vertical device geometries, where the ratio of contact area to device area is often higher than in lateral device geometries.

Schottky-junction solar cells represent one specific device geometry where van der Waals metal contacts could enable high performance in vertical devices. Although vertical-junction solar cells are more aligned with conventional photovoltaics (*47*), most Schottky-junction TMD solar cells studied have been lateral-junction devices (*32*, *33*, *37*). Vertical Schottky-junction TMD solar cells have been limited by ohmic I-V behavior, low external quantum efficiencies, and low open-circuit voltages, likely due to Fermi-level pinning induced by contact evaporation (*21*, *34*). New gentle contact fabrication techniques have the potential to eliminate this Fermi-level pinning, enabling high-efficiency vertical TMD solar cells in the Schottky-junction geometry.

Here, we develop a simple technique for transferring metal contacts, where all lithographic patterning is done on a donor substrate rather than on the active device. We apply this technique to vertical Schottky-junction solar cells with multilayer TMD absorber layers. Due to the tradeoff between bandgap energy and photoluminescence quantum yield, the theoretical maximum power conversion efficiency achievable for multilayer and monolayer single-junction solar cells is similar (*19*, *23*), and further, tunneling limits transport in monolayer vertical devices (*27*), so we focus on multilayer devices in this work. Ultrathin (10–20 nm) WS_2 forms the absorber layer, while Ag and Au form the asymmetric-work-function contacts. Devices made with transferred metal contacts show diode-like I-V behavior with a near-unity ideality factor and high V_{OC}, while similar devices made with evaporated metal contacts show ohmic I-V behavior and near-zero V_{OC}. We demonstrate peak external quantum efficiency (EQE) of >40% and peak active-layer internal quantum efficiency (IQE_{active}) of >90% in transferred-contact devices. Using a solar simulator, we measure a photovoltaic power conversion efficiency of 0.46%, comparable to what has been seen in ultrathin vertical TMD photovoltaics with a p-n junction rather than a Schottky junction (*28*, *35*). Device simulations of further-optimized geometries suggest that this new metal transfer process has the potential to enable Schottky-junction TMD solar cells with power conversion efficiencies greater than 8% and specific powers greater than 50 kW/kg.

2.2 Fabrication of Vertical WS_2 Schottky-Junction Solar Cells

We prepare vertical WS_2 Schottky-junction solar cells made from 16-nm-thick WS_2 absorber layers, with Ag ($\phi_{Ag} \approx 4.3$ eV) and Au ($\phi_{Au} \approx 5.1$ eV) as asymmetric work function contacts (Figure 11A) (*32*). Template-stripped Ag, which exhibits an RMS roughness <0.5 nm, forms both the electron-collecting bottom contact and back reflector for all devices (*48*). We mechanically exfoliate WS_2 directly onto the Ag substrate. The subwavelength-thick WS_2 achieves broadband, angle-insensitive absorption on top of the highly reflective Ag, giving the WS_2 a deep purple color (*21*, *49*). For transferred-contact devices, we transfer thin Au disks from a thermally-oxidized Si donor substrate to form the semi-transparent hole-collecting top contact, using the process described in the following section. Both the top surface of the template-stripped Ag and the bottom surface of the

transferred Au inherit the smoothness of the SiO_2/Si donor substrate, leading to near atomically-sharp metal-WS_2 interfaces (*32*, *48*). Using cross-sectional analysis by transmission electron microscopy (TEM), we examine the interface between the transferred Au and the WS_2 (Figure 11B). We find that in contrast to depositing Au via electron-beam evaporation (*32*), transferring Au does not damage the intrinsically-passivated WS_2 layers, as evidenced by the columns of atoms visible in the TEM image. Figure 11C shows an optical image of a completed device. For comparison, we also fabricate devices by direct evaporation of thin Au disks onto the WS_2 using standard photolithography techniques.

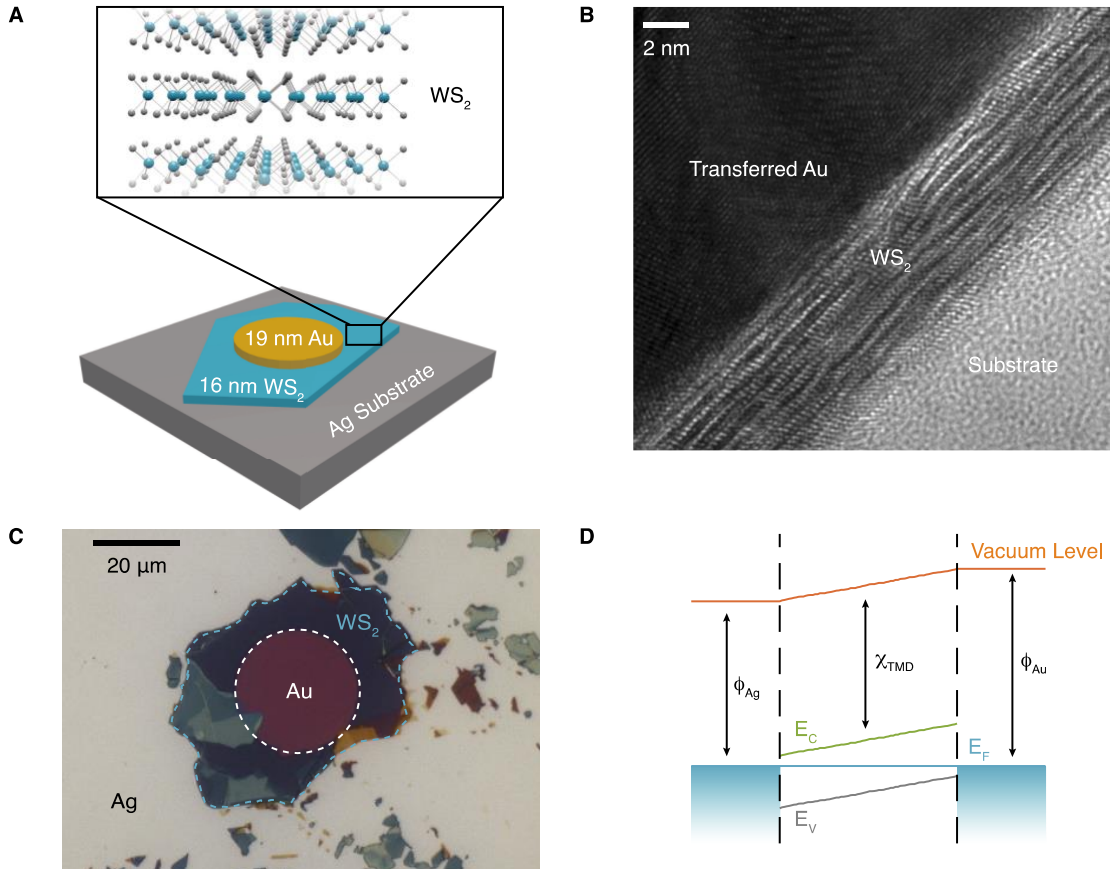

Figure 11. **Vertical Schottky-junction multilayer WS_2 solar cells with transferred contacts.** (**A**) Bottom: Schematic of device structure. Top contact is a transferred gold disk; bottom contact and back-reflector is template-stripped silver. Top: three-dimensional representation of multilayer WS_2. W, blue spheres; S, grey spheres. (**B**) Cross-sectional image of metal-semiconductor interface captured by transmission electron microscopy. (**C**) Optical image of device. (**D**) Solar cell band diagram obtained from electrostatic simulations.

The ideal band diagram of this Schottky-junction solar cell is shown in Figure 11D. We assume a doping concentration of 10^{14} cm^{-3} for WS_2, as provided by the bulk crystal vendor. Since the length of the depletion region at a Schottky junction between bulk WS_2 and either Au or Ag is on the order of 1 μm, the device is fully depleted. We measure the final thicknesses of the WS_2 and the Au to be 16 nm and 19 nm, respectively, using atomic force microscopy.

2.3 Metal Transfer Process

We develop a new, simple process for transferring metal contacts onto TMDs (Figure 12).

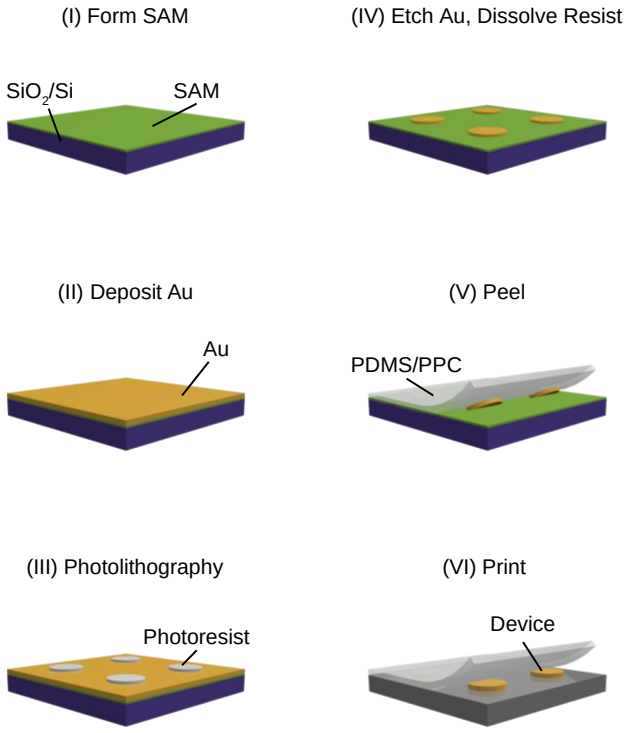

Figure 12. **Metal transfer process.** Briefly, a self-assembled monolayer is applied to a clean SiO_2/Si substrate (I). Au is deposited in an electron beam evaporator (II). Disk contacts are defined using photolithography (III), and the surrounding Au is etched away (IV). To peel the contacts, a PDMS/PPC stamp is laminated to the contacts, heated above the glass transition temperature of PPC, then cooled and removed quickly (V). To print the contacts, the PDMS/PPC stamp is aligned and laminated onto the device, then peeled away slowly above the glass transition temperature of PPC, leaving the contacts behind (VI).

This process relies on a self-assembled monolayer (SAM) to reduce the adhesion between the Au and the SiO_2/Si donor substrate (*50*), a thermoplastic polymer to preferentially pick up or drop down the metal (*51*), and a variable peeling rate to tune the velocity-dependent adhesion between a metal and a viscoelastic stamp (*50*).

Briefly, we create a SAM on clean thermally-oxidized Si chips in a vacuum desiccator (*50*). We then deposit 20 nm of Au via electron beam evaporation. Using photolithography, we define the contact areas with positive photoresist and a positive photomask. We etch the Au outside the masked contact areas, then dissolve the remaining photoresist in acetone, leaving Au disks on the SAM-coated SiO_2/Si substrates. We prepare a polydimethylsiloxane (PDMS) stamp coated with the thermoplastic polymer polypropylene carbonate (PPC) on a glass slide (*51*). In a 2D transfer setup, we align and slowly lower the stamp onto a contact at 60ºC. We set the temperature to 40ºC, and once the stage reaches that temperature, we raise the transfer arm rapidly to peel the stamp and pick up the contact. We align the contact with the target TMD and slowly lower the stamp down at 60ºC, and then slowly peel it away immediately after contact at the same temperature. The contact delaminates from the PDMS/PPC stamp and sticks to the TMD. Further details of the procedure are provided in Appendix B.

This metal transfer technique has worked in 15 out of 16 devices fabricated thus far (>90% yield). It works for both 20-nm-thick and 100-nm-thick Au, and can be extended to other metals and to larger-scale contacts (i.e. for contacts to CVD-grown TMDs). A substantial advantage of this technique is that, whereas prior metal transfer techniques require a final aligned electron-beam lithography step to expose the contact area (*32*), this technique only utilizes unaligned photolithography to define the initial contacts on the SiO_2/Si donor substrate. This allows for batch-fabrication of an array of contacts that can then be picked up, aligned, and printed to form multiple devices. Further, this metal transfer process could enable van der Waals contacts to air- and moisture-sensitive nanomaterials, such as lead halide perovskites or black phosphorus, to be formed without removing the sample from an inert environment.

2.4 Comparison of Transferred and Evaporated Metal Contacts

We measure I-V curves under illumination with a 633 nm laser focused to a ~1 μm^2 spot in a confocal microscope at room temperature. In devices with transferred metal contacts, we observe rectifying I-V curves and a pronounced photovoltaic effect (Figure 13A). We measure a V_{OC} of 510 mV under the maximum laser excitation. Short-circuit current follows a power law as a function of incident power, $I_{SC} = P_{inc}^{\alpha}$, with α close to 1 (Figure 13C). According to the diode equation, V_{OC} scales linearly with ln(I_{SC}) and can be fit with an ideality factor n = 1.2 (Figure 13D). This near-unity ideality factor confirms the high interface and material quality in these devices. The ideality factor, diode-like behavior and high open-circuit voltage suggest that a Schottky junction is successfully formed in devices with transferred contacts.

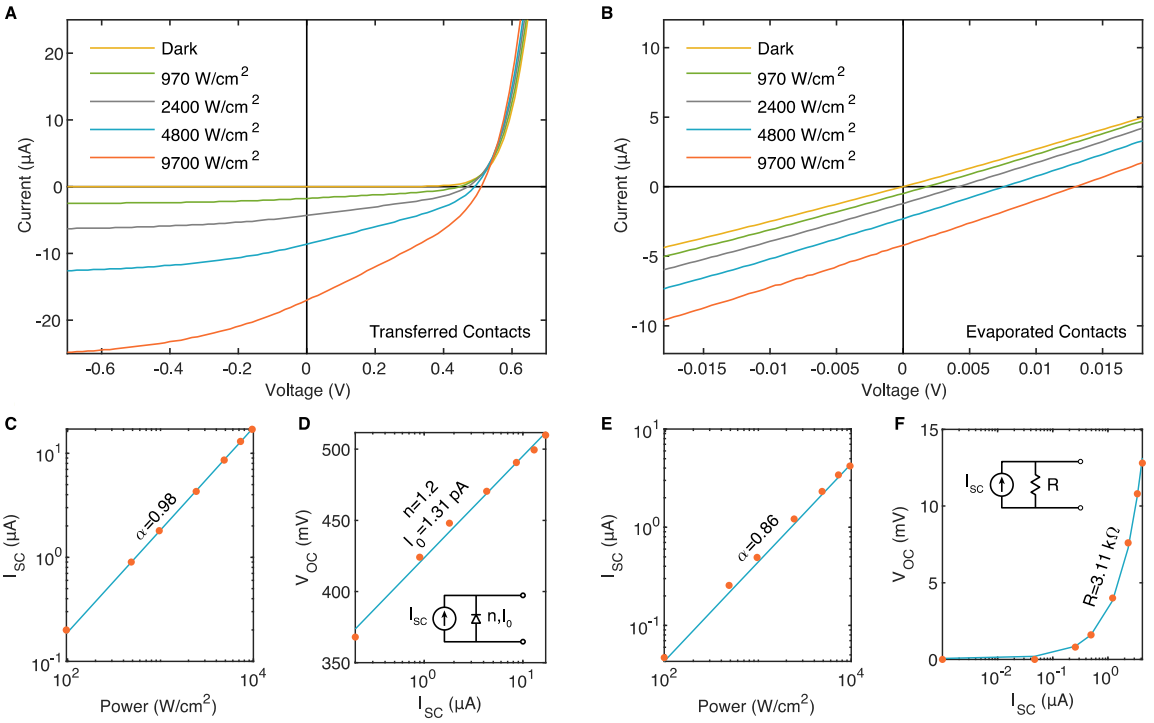

Figure 13. **Comparison of devices with transferred and directly evaporated top metal contacts.** (**A, B**) Power-dependent I-V characteristics of devices with transferred (**A**) and evaporated (**B**) Au top contacts taken under excitation with a 633 nm laser focused to a spot size of ~1 μm^2. (**C, E**) Short-circuit current of devices with transferred (**C**) and evaporated (**E**) Au contacts. Symbols, measurements; line, power law fit. (**D, F**) Open-circuit voltage of devices with transferred (**D**) and evaporated (**F**) Au contacts. Symbols, measurements; line, fit. Insets show representative circuit diagrams. n is the ideality factor and I_0 is the dark saturation current extracted from the diode fit in (**D**). R is the resistance extracted from the linear fit in (**F**).

In contrast, we observe resistive behavior and a small photovoltaic effect in devices with evaporated top metal contacts (Figure 13B). I_{SC} vs. P_{inc} follows a power law with $\alpha < 1$ (Figure 13E). As shown in Figure 13F, this device behaves as a resistor with R = 3.1 kΩ. At comparable laser powers, V_{OC} is around 4 mV in evaporated contact devices and 400 mV in transferred contact devices, and J_{SC} is three to four times higher for transferred contacts than for evaporated contacts. Previous work demonstrates that due to Fermi-level pinning, evaporated Au and transferred Ag have effectively the same barrier height for electrons and holes (*32*). Assuming an effective work function difference between Au and Ag of 50 meV, device simulations can predict the purely resistive behavior in an evaporated-contact Schottky-junction device. This evidence points to strong Fermi-level pinning in devices with evaporated contacts due to interface states induced by the Au evaporation.

In devices with transferred contacts, the slope of the I-V curve at short-circuit increases linearly with increasing laser power, corresponding to a decreasing shunt resistance. This photoshunting effect occurs in solar cells without perfectly selective contacts due to increased minority carrier conductivity across the device under illumination (*52*, *53*). Device simulations can replicate this photoshunt pathway without the addition of any external shunt resistance. In future devices, the introduction of contacts with greater carrier selectivity or the combination of a p-n junction with a Schottky junction could reduce or eliminate the photoshunting observed here.

2.5 Quantum Efficiency and Photocurrent Generation

Light-beam induced current (LBIC, or photocurrent) maps, acquired with a 633 nm laser in a confocal microscope, show uniform current generation under the entire Au disk contact, except where shaded by the contact probe (Figure 14A). The uniformity of the photocurrent demonstrates that the Au is homogeneously semitransparent and in good contact with the TMD. Importantly, this indicates that the area of the Au disk can be used to accurately define the device active area and suggests that one-dimensional device simulations are sufficient to describe the behavior in these vertical devices (*54*). Further, it demonstrates that there are no visible bubbles created during the metal transfer process.

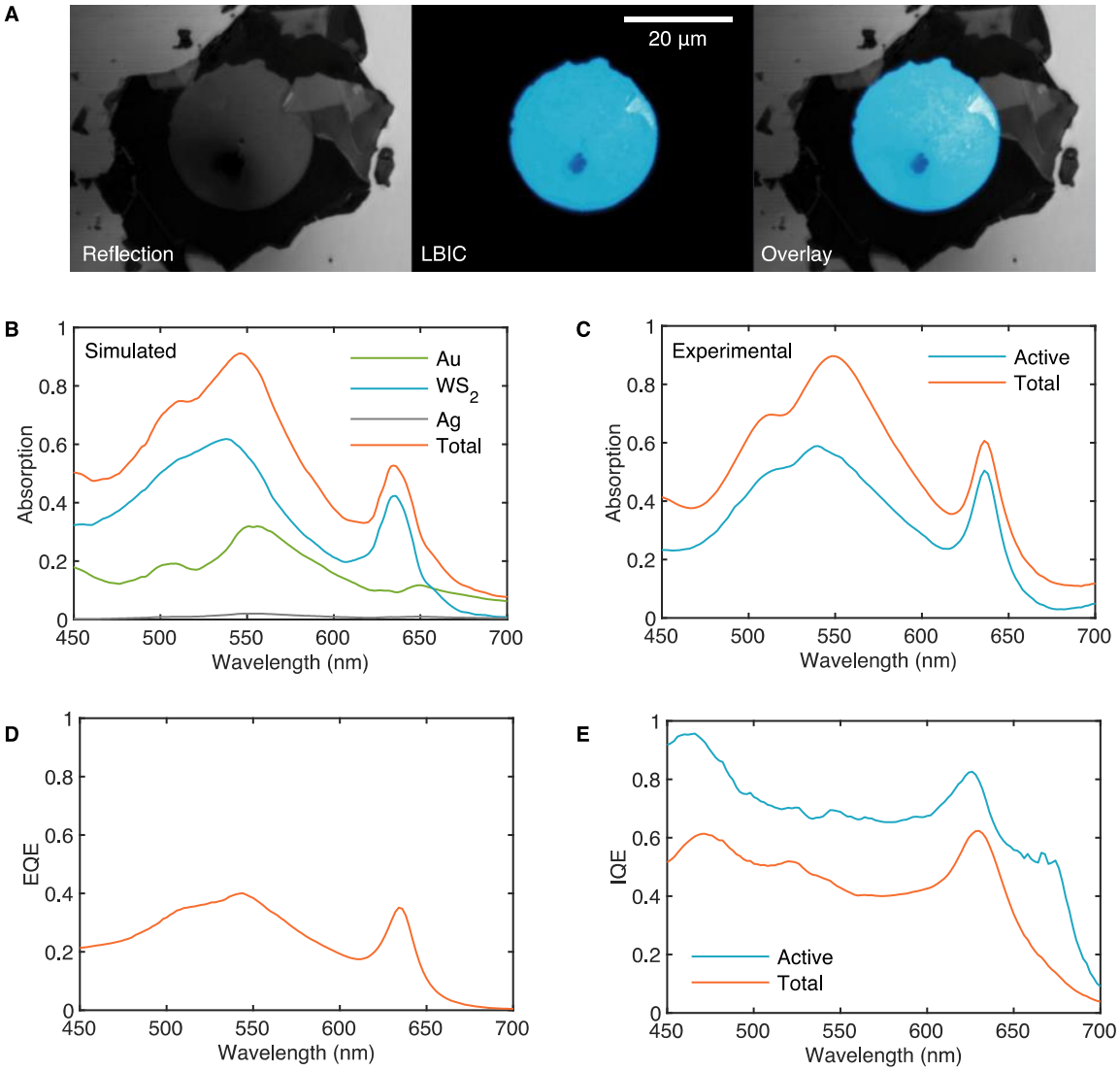

Figure 14. **Photocurrent and quantum efficiency.** (**A**) Confocal reflection, photocurrent, and reflection/photocurrent overlay maps for the device. The dark spot in the lower left part of the device active area is a probe tip artifact. (**B**) Simulated total absorption in the device and absorption in each device layer. (**C**) Experimental total absorption in the device and active-layer absorption calculated by subtracting the simulated parasitic absorption from the experimentally measured total absorption. (**D**) Measured external quantum efficiency. (**E**) Internal quantum efficiency calculated from external quantum efficiency and absorption; active-layer internal quantum efficiency calculated from external quantum efficiency and active-layer absorption.

The measured total absorption (Figure 14C) matches well with the absorption calculated using the transfer matrix method (Figure 14B), as has been previously demonstrated in TMD solar cells (*21*, *34*). To calculate the active-layer absorption in the experimental WS_2 devices, we subtract the simulated parasitic absorption (the sum of the Au and Ag curves

in Figure 14B) from the experimentally measured total absorption in Figure 14C. The mean active-layer absorption from 450 nm to 650 nm is 39%. The reduced absorption in our devices relative to what has been previously demonstrated in WS_2 on a metal back-reflector (~80% over this wavelength range) (*21*) is due to parasitic absorption and reflection losses from the 19-nm-thick Au top contact. Using a more transparent top contact could double our photogenerated current, assuming identical work function and conductivity.

The external quantum efficiency (EQE) of the device follows the spectral shape of absorption well, averaging 28% from 450 nm to 650 nm and reaching a peak of above 40% around 550 nm (Figure 14D). To accurately determine EQE, we multiply by a shading factor of 1.39 to correct for shading from the probes (see Appendix B). Internal quantum efficiency (IQE) remains relatively flat across all wavelengths above the bandgap, averaging 49% from 450 nm to 650 nm (Figure 14E). IQE_{active}, calculated by dividing EQE by the active-layer absorption rather than the total absorption, is greater than 90% at its peak, and averages 74% between 450 nm and 650 nm (Figure 14F). This high IQE_{active} suggests efficient collection of photogenerated carriers in transferred-contact devices.

2.6 Performance Under One-Sun Illumination

Vertical Schottky-junction WS_2 solar cells with transferred top contacts achieve reasonable photovoltaic performance when measured under simulated AM1.5G illumination. Figure 15 shows the AM1.5G I-V behavior of a representative device. We divide the measured current by the device active area to yield current density, then then further divide by a factor of 0.67 to account for spectral mismatch between our solar simulator calibration point and the true AM1.5G spectrum (see Appendix B: Fabrication Methods) (*55*). The spectral mismatch correction leads to a 50% increase in short-circuit current, so the V_{OC} and power conversion efficiency of the device are likely underestimated here. We measure a V_{OC} of 256 mV, a corrected J_{SC} of 4.10 mA/cm^2, a fill factor (FF) of 0.44, and a power conversion efficiency (PCE) of 0.46%. This efficiency is in the range of what others have reported for ultrathin TMD photovoltaics (*28*, *34*, *35*, *37*). Using the densities of Au, WS_2, and Ag, we estimate a specific power of 3 kW/kg for this device.

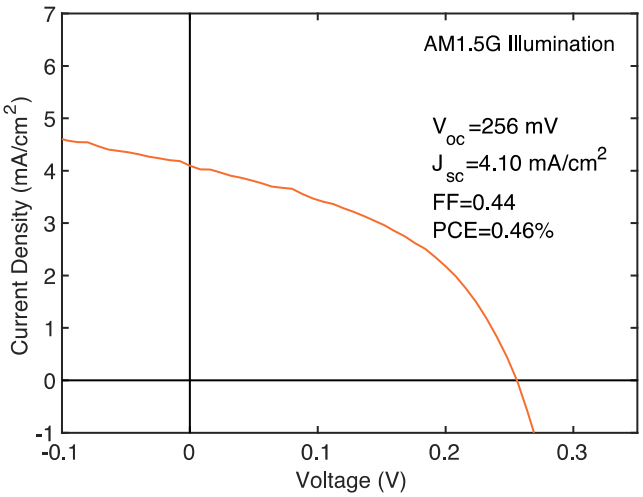

Figure 15. **Photovoltaic performance under one-sun illumination.** I-V characteristics of a vertical Schottky-junction multilayer WS_2 solar cell measured using an AM1.5G solar simulator, corrected for spectral mismatch.

By fitting the one-sun I-V curve using the diode equation with series and shunt resistances, we estimate a shunt resistance (R_{SH}) of 231 Ω cm^2 and a negligible series resistance (R_S). The shunt resistance is likely due to the photoshunting behavior discussed above, and could be reduced by design and realization of contacts that are more carrier-selective.

This photovoltaic performance is consistent among multiple measurements and devices. The J_{SC} of 4.10 mA/cm^2 that we measure with the solar simulator is within 10% of the J_{SC} that we calculate by integrating the EQE over the solar spectrum (4.55 mA/cm^2). We believe that probe shading, which we correct for in EQE measurements but not in solar simulator measurements, accounts for the 10% discrepancy. Though the J_{SC} varies due to differences in thickness and therefore absorption in exfoliated flakes, the V_{OC} is replicable across all devices fabricated for this work. V_{OC} is between 220 mV and 260 mV in all four devices measured under one-sun illumination, and V_{OC} is > 220 mV in six different devices measured under illumination with a halogen lamp (~20 suns power density). The I-V curves show no hysteresis when swept in the forwards and backwards directions.

2.7 Simulated Performance of Optimized Devices

To examine and further optimize the performance of these devices, we simulate a variety of device geometries. The assumed material parameters of the WS_2 are detailed in Table 1.

Simulating the same device geometry as our experimental device yields the I-V curve in Figure 16A. The simulated J_{SC} of 5.7 mA/cm^2 is consistent with our measured active-layer IQE of 74% and the J_{SC} of 4.55 mA/cm^2 estimated from the EQE. The simulated V_{OC} of 646 mV and R_{SH} of 2240 Ω cm^2 are considerably higher than the V_{OC} of 256 mV and R_{SH} of 231 Ω cm^2 observed in our one-sun measurements. This demonstrates that with further optimization, our device geometry could achieve higher voltages and less shunting than we currently see. As a first improvement, we suggest replacing Au with a different high-work-function metal, as Au is known to form thiol bonds with sulfides that could affect the quality of the van der Waals contact (*32*, *56*).

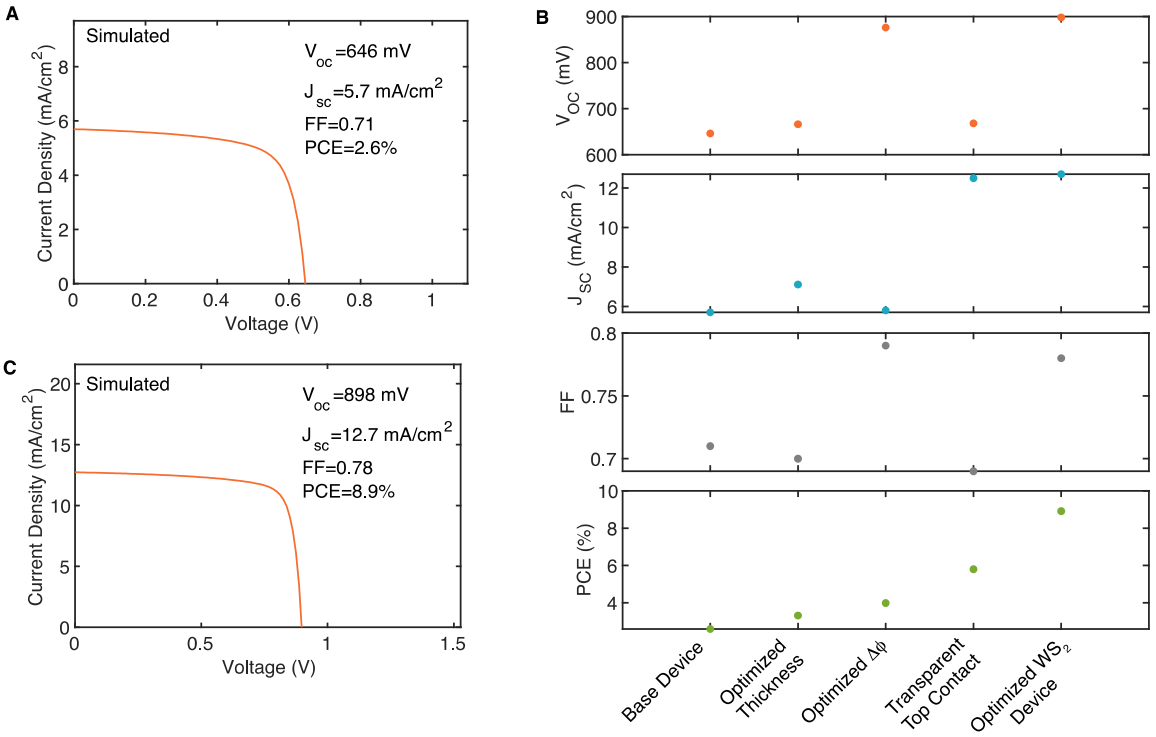

Figure 16. **Simulated performance of optimized devices.** (**A**) Simulated I-V characteristics of the device geometry used in our experiments, assuming no external series/shunt resistances. (**B**) Simulated V_{OC}, J_{SC}, fill factor, and power conversion efficiency for optimized devices. Apart from the final device geometry ("Optimized WS_2 Device"), optimizations are independent, not cumulative. (**C**) Simulated I-V characteristics of the fully-optimized WS_2 device.

To identify a potential path towards high-efficiency vertical Schottky-junction WS_2 solar cells, we simulate a series of optimized devices (Figure 16B). Using an optimized thickness

of WS_2 (26 nm) for maximum absorption under 20 nm of Au increases the J_{SC} to 7.1 mA/cm^2. The J_{SC} can be further increased to 12.5 mA/cm^2 by replacing Au with a transparent top contact, assuming an identical work function to Au and no parasitic absorption or reflection. By selecting metal work functions that are optimally aligned to the conduction and valence bands of WS_2 (ϕ_1 = 4.05 and ϕ_2=5.2 eV, e.g. In and Pd), we predict a V_{OC} increase of 230 mV. Combining transparent top contacts and optimized metal work functions yields the device shown in Figure 16C, with a V_{OC} of 898 mV, a J_{SC} of 12.7 mA/cm^2, a fill factor of 0.78, and a power conversion efficiency of 8.9%. This simulated power conversion efficiency in a device with a thickness <150 nm represents a specific power of 58 kW/kg, demonstrating that this metal transfer process has the potential to enable devices with an unprecedented power-per-unit-weight ratio for transportation and aerospace applications.

Table 1: **WS_2 parameters for device simulations in Lumerical.**

Parameter	**Value**	**Source**
Bandgap	1.35 eV	(*57*)
Work function	4.62 eV	(*58*)
Electron effective mass	$0.63m_e$	(*59*)
Hole effective mass	$0.84m_e$	(*59*)
Doping	10^{14} cm^{-3}	HQ Graphene
Out-of-plane mobility (for holes & electrons)	0.01 cm^2/Vs	(*60–62*)
DC permittivity	6.7	(*63*)
Radiative recombination coefficient	1.64×10^{-14} cm^3/s	Calculated using optical constants in (*64*)
Shockley-Read-Hall Lifetime	611 ns	Calculated using PLQY from (*65–67*)

2.8 Conclusion

We develop here a process for transferring metal contacts with near-atomically smooth interfaces that has high-yield, allows for batch fabrication, and eliminates aligned lithography. We expect that this procedure will be highly relevant and useful to the 2D community, as well as to researchers working on air-sensitive nanomaterials, as it allows all processing to be done on the contacts rather than the device. By applying this new technique to vertical Schottky-junction TMD solar cells, we demonstrate that transferred contacts are particularly advantageous for vertical device geometries, which are important for photovoltaic and other optoelectronic applications due to their scalable active areas. Recent advances in techniques such as growth of wafer-scale 2D TMDs via chemical vapor deposition (*68–70*) and pick-up and stacking of large-area van der Waals materials (*71*) will enable the scaling of TMD solar cells from micron-scale to wafer-scale.

The rectifying I-V curves shown in transferred-contact devices and resistive I-V curves shown in evaporated-contact devices support the hypothesis that transferring contacts can reduce Fermi-level pinning and allow the work function asymmetry between the contacts to define the maximum achievable V_{OC}. We observe active-layer absorption >55%, EQE >40%, and active-layer IQE >90% in these devices, demonstrating efficient collection of photogenerated carriers. Under one-sun illumination, we measure a V_{OC} of 256 mV, a J_{SC} of 4.10 mA/cm^2, a fill factor of 0.44, and a power conversion efficiency of 0.46%. We highlight areas for improvement by simulating the behavior of optimized devices based on this architecture and show 8.9% simulated efficiency and 58 kW/kg simulated specific power in a device with transparent top contacts, optimized thickness, and ideal metal work functions for carrier extraction.

Given the proof-of-concept performance and the clear pathways for improvement presented here for devices less than 150 nm thick, ultrathin vertical Schottky-junction TMD solar cells with transferred contacts are promising candidates for high-specific-power photovoltaic applications. We anticipate that this new metal transfer process will enable similar advances for 2D TMD devices beyond Schottky-junction solar cells, as well as for nanomaterial-based devices more broadly.

Chapter 3: Achieving High Open-Circuit Voltage in Carrier-Selective Contact Transition Metal Dichalcogenide Photovoltaics

Transition metal dichalcogenide solar cells are promising candidates for high-specific-power photovoltaics, with reported power conversion efficiencies now greater than 5%. To date, most transition metal dichalcogenide solar cells rely on p-n or Schottky junctions, although the highest efficiency silicon and perovskite solar cells employ carrier-selective contacts. Here, we achieve a one-sun open-circuit voltage of 523 mV and one-sun power conversion efficiency of 2.4% in a carrier-selective contact multilayer WS_2 solar cell with an ultrathin (10-nm-thick) active layer. Following the most efficient inverted perovskite device architectures, we use C60 as an electron-transporting layer and PTAA as a hole-transporting layer, and we outline a library of low-cost perovskite selective contacts that are transferrable to transition metal dichalcogenides. We demonstrate that symmetric carrier-selective contact conductance is important for high fill factors, and we show that S-shaped I-V curves can be eliminated by thinning down the low-conductance contact. Finally, we show that the maximum open-circuit voltage of undoped multilayer transition metal dichalcogenide solar cells is limited by their short lifetimes to 750 mV, and we outline suggestions for overcoming this materials challenge.

3.1 Introduction

Two-dimensional (2D) semiconducting transition metal dichalcogenides (TMDs), including MoS_2, WS_2, $MoSe_2$, and WSe_2, are promising new photovoltaic materials (*23*, *72*). They exhibit strong light-matter interactions, with absorption coefficients 1–2 orders of magnitude higher than conventional semiconductors in the visible range (*16*, *21*). They can be easily stacked into heterostructures without the constraint of lattice matching, as layers couple through the van der Waals interaction. Combined, these factors make 2D TMDs promising for low-cost ultrathin solar cells, with potential applications where high specific power (power per unit weight) is needed. These applications could include aerospace, vehicle-integrated, or building-integrated photovoltaics (*41*).

Despite their promise, most 2D TMD solar cells exhibit efficiencies less than 2% and open-circuit voltages less than 600 mV under simulated solar illumination (*34–37*, *73–78*). A notable exception to this is recent work from Nassiri Nazif et al, which has shown an open-circuit voltage of 681 mV in WS_2 p-n junction solar cells with MoO_3 doping and lateral carrier transport (*38*) and a power conversion efficiency of 5.1% in WSe_2 Schottky-junction solar cells with 200-nm-thick TMD layers, MoO_3-doped graphene contacts and vertical carrier transport (*39*). To improve upon existing 2D TMD solar cells, researchers must focus on 1) continuing to improve efficiency, of which open-circuit voltage is usually the most challenging component, 2) designing and fabricating even thinner solar cells, on the order of 10 nm, and 3) working towards cheap, scalable fabrication methods for large-area solar cells that rely on vertical carrier transport.

To date, most 2D TMD solar cells have either employed p-n junctions (*34–36*, *38*, *74*, *75*, *77*) or Schottky junctions (*37*, *39*, *73*, *76*, *78*) for charge carrier separation. However, carrier-selective contact solar cells are widely considered to have the highest efficiency potential for a given absorber material (*52*). In a carrier-selective contact solar cell, an intrinsic absorber is sandwiched between two carrier-selective contacts (or equivalently, the charge transport layers), which are highly doped wide-bandgap semiconductors. The hole transport layer (HTL) is p-doped, with its valence band aligned with that of the absorber, and the electron transport layer (ETL) is n-doped, with its conduction band aligned with that of the absorber. By separating the absorber and the transporter, carrier-selective contact solar cells achieve both high minority carrier concentration in the absorber, necessary for high V_{OC}, and low minority carrier conductivity at the contacts, necessary for high selectivity (*52*). In fact, the highest efficiency silicon and perovskite solar cells rely on this carrier-selective contact geometry.

A library of carrier-selective contact materials has been developed for perovskite solar cells, most of which can be deposited via low-cost methods such as spin-coating or thermal evaporation (*79*). The highest efficiency inverted (p-i-n) perovskite solar cells use PTAA HTLs and C60 ETLs, and have achieved 23% power conversion efficiency (*80–82*).

Here, inspired by this geometry, we fabricate carrier-selective contact WS_2 solar cells using 8-nm-thick PTAA as the HTL, 10-nm-thick WS_2 as the absorber, and 2-nm-thick C60 as the ETL. These devices achieve an open-circuit voltage of 523 mV and a power conversion efficiency of 2.4% under one-sun illumination. We characterize the optoelectronic properties of these solar cells, including photocurrent, absorption, quantum efficiency, and I-V behavior. We show that asymmetric contact conductance can lead to S-shaped I-V curves, and we propose thickness dependence as a powerful means of diagnosing the low-conductance selective contact. By reducing the thickness of the C60 from 20 nm to 2 nm, we recover high fill factor in carrier-selective contact WS_2 solar cells. From photoconductivity measurements, we calculate the minority carrier lifetime to be ~100 ps, limiting the voltage entitlement in these devices to 590 mV. More broadly, we demonstrate that the short lifetime in TMDs limits the open-circuit voltage in undoped, multilayer solar cells to 750 mV. We outline suggestions for overcoming this challenge as well as for improving upon the specific device geometry presented here.

3.2 Appropriate Carrier-Selective Contacts for Transition Metal Dichalcogenides

Figure 17 shows the predicted band alignment between multilayer TMDs and common carrier-selective contact materials.

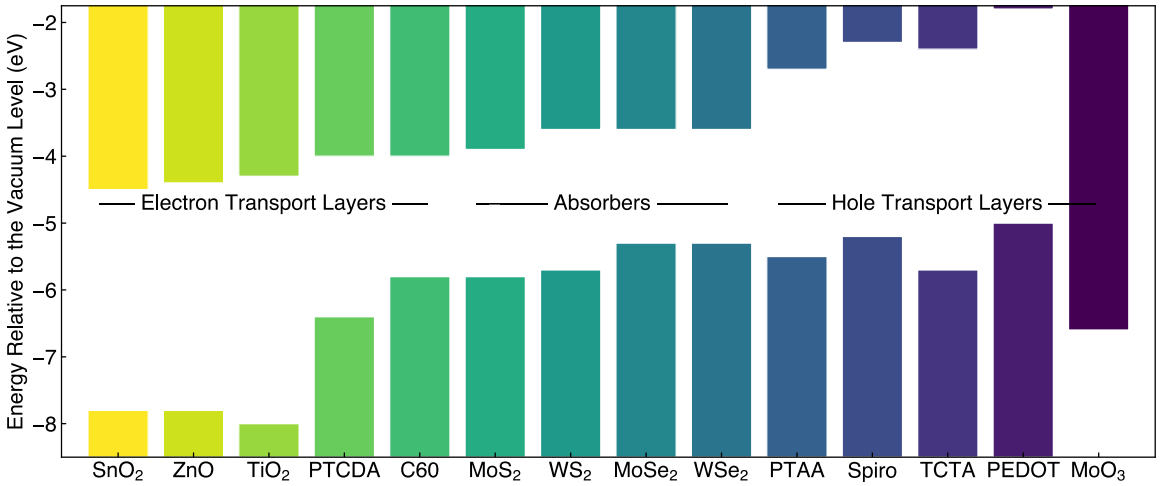

Figure 17. **Band alignment between TMDs and common selective contact layers.** Band alignments derived from (*57*, *58*, *79*, *83–86*).

As both the electron affinity and bandgap are similar between multilayer TMDs and common lead halide perovskites, many carrier-selective contacts that are used in perovskite solar cells are transferrable to TMD solar cells. We note that this assumes Anderson's rule for band alignment between two semiconductors, which is usually an approximation. Once researchers determine an appropriate selection of materials for carrier-selective contacts to TMDs, a more accurate picture should be developed through experimental measurement of band alignments, using techniques such as photoelectron spectroscopy.

To fabricate mechanically exfoliated TMD solar cells, the bottom selective contact must be smooth enough to serve as an exfoliation substrate. Figure 18 demonstrates that the morphology of the substrate greatly affects the yield and size of exfoliated flakes. Substrates with large, smooth facets maximize the van der Waals bonding between the substrate and the TMD, leading to many large-area exfoliated flakes. In contrast, substrates with sub-micron-scale roughness make weak contact with TMD flakes at many points, yielding small exfoliated flakes. We found that metal oxides deposited by most common deposition techniques and fullerene-like selective contacts were too rough to serve as substrates for exfoliation of sufficiently large-area TMDs. Since many common electron transport layers (ETLs) are either metal oxides or fullerenes, we used the hole transport layer (HTL) as the bottom selective contact in our devices. In particular, we found that exfoliation onto spin-coated polymeric and small molecule HTLs (such as PTAA, spiro-OMeTAD, TCTA, and PEDOT:PSS) yielded large-area flakes, suggesting that these spin-coated layers are smooth enough to form strong van der Waals bonds with TMDs.

The top selective contact must be deposited gently to avoid damaging the intrinsically passivated TMD surface (*32*, *76*). Deposition techniques such as electron-beam evaporation and sputtering are too energetic to preserve the surface, so metal oxides deposited by these techniques are not viable top contact materials. Thermal evaporation is a comparatively gentle deposition technique, which has been shown to leave a monolayer sulfur passivation layer intact on a GaAs surface (*87*). Therefore, thermally evaporated ETLs (such as C60, PTCDA, and other fullerenes) as well as spin-coated ETLs (such as SnO_2 nanoparticles, TiO_2 nanoparticles, and other metal oxide nanoparticles) could potentially serve as electron-transporting top contacts.

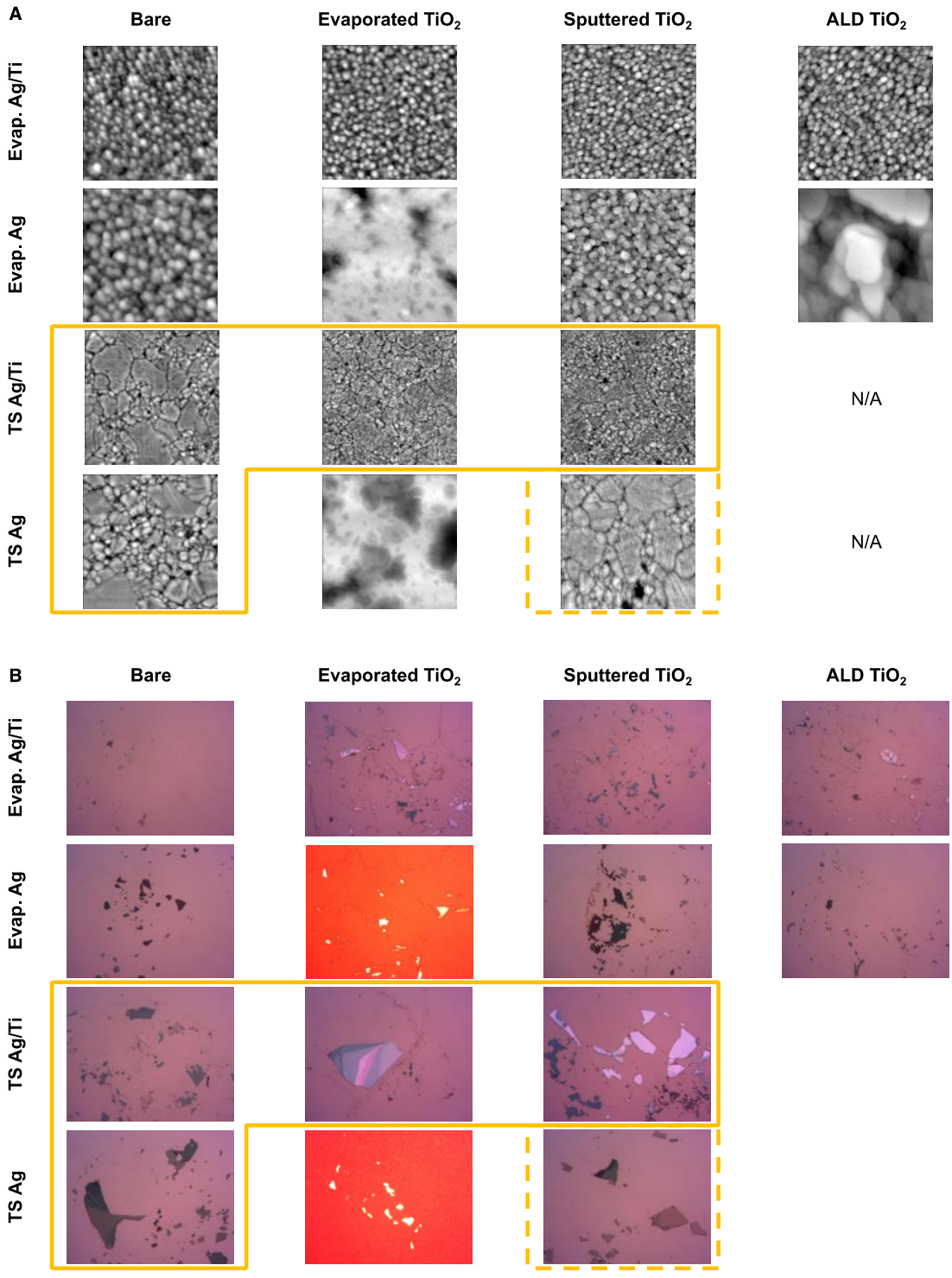

Figure 18. **Effect of substrate morphology on size of exfoliated flakes.** Four metal substrates were studied with three TiO_2 deposition techniques. (**A**) AFM scans (1 μm × 1 μm). (**B**) Optical microscope images (field of view ~130 μm × 175 μm). Solid yellow box represents the smoothest substrates, and correspondingly, the largest-area exfoliated flakes. Dashed yellow box represents an intermediate case. TS, template-stripped.

Fortuitously, the highest-efficiency inverted (or p-i-n) perovskite solar cells satisfy the dual constraints of 1) a spin-coated polymeric or small molecule bottom contact that is smooth enough to yield large-area exfoliated flakes and 2) a spin-coated or thermally-evaporated top contact that is gentle enough to preserve the intrinsically passivated TMD basal plane. These devices employ a 10-nm-thick spin-coated PTAA HTL as the bottom selective contact on top of an ITO-coated glass superstrate, and a 20-nm-thick thermally evaporated C60 ETL as the top selective contact (*80–82*). A silver top electrode is thermally evaporated as well as a 5-nm-thick BCP interlayer, which prevents a Schottky junction from forming between the C60 and the silver. Based on this, we choose PTAA as an HTL and C60 as an ETL for our initial carrier-selective contact TMD solar cells.

3.3 WS_2 Carrier-Selective Contact Solar Cells

Figure 19A presents a schematic of the WS_2 carrier-selective contact solar cell. This device consists of a template-stripped Au bottom electrode and substrate, a 10-nm-thick PTAA HTL, a 10-nm-thick exfoliated WS_2 flake, a 2-nm-thick C60 active layer, a 2-nm-thick BCP interlayer, and a 30-nm-thick Ag top electrode. The C60 and BCP layers are thinner in our devices than in the perovskite solar cells on which they are modeled for reasons that will be discussed in subsequent sections. Fabrication details are provided in Appendix B.

It is likely that the BCP outside of the contact area dissolves in the process, as BCP is soluble in acetone and most common solvents. We are unsure if the C60 survives outside of the top contact area. However, if C60 remains across the entire chip, shunting between the C60 and PTAA is not a concern, as a Au/PTAA/C60/Ag device would behave like a diode with a turn-on voltage beyond our measurement range in parallel with our solar cell.

Figure 19B shows an optical microscope image of the device measured in subsequent sections of this paper. Using atomic force microscopy, we measure the thickness of the WS_2 flake to be 10 nm (Figure 19C). Figure 19D presents a band diagram of this device under illumination and at short-circuit, simulated in Sentaurus TCAD. The device simulation parameters can be found in Table 2.

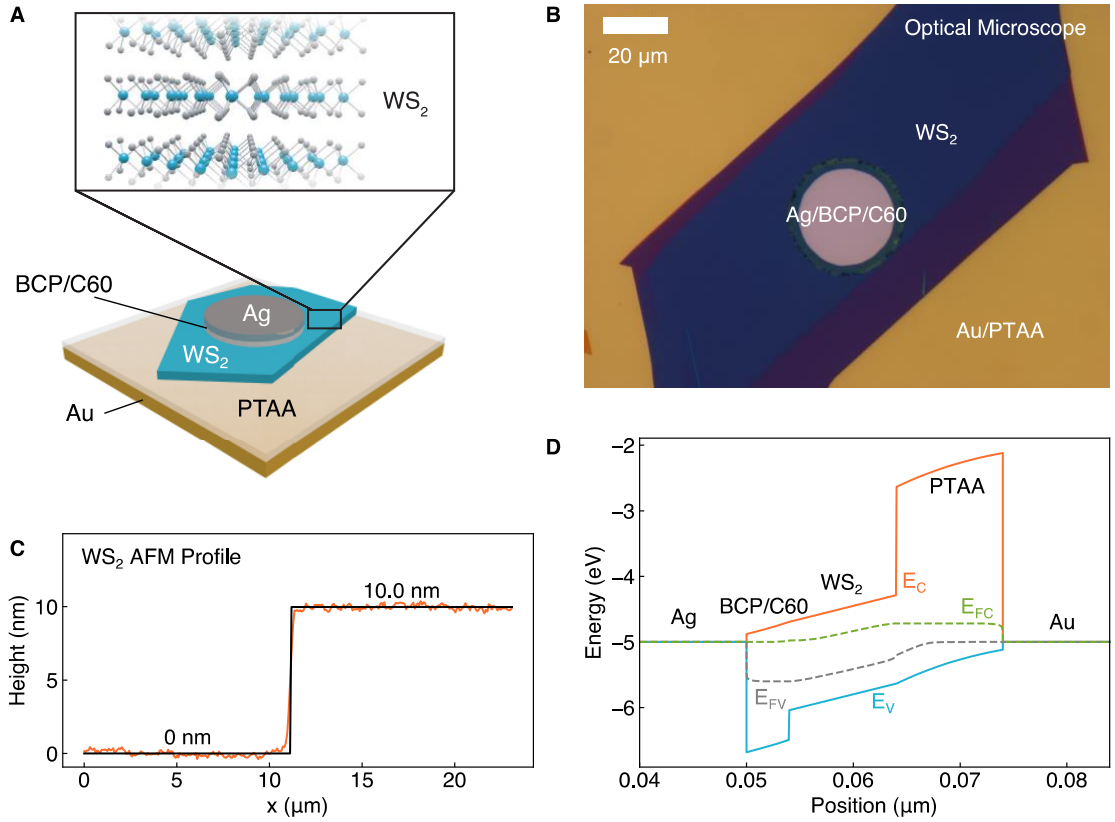

Figure 19. **Device geometry of carrier-selective contact WS_2 solar cells.** (**A**) Schematic of device structure. (**B**) Optical microscope image of device. (**C**) AFM profile showing thickness of WS_2. (**D**) Band diagram under illumination and at short-circuit simulated in Sentaurus TCAD.

3.4 Device Geometry Shows Potential for Effective Current Collection

We collect light-beam induced current (LBIC, or photocurrent) maps with a 633 nm laser in a confocal microscope (Figure 20A). The photocurrent map demonstrates that the device collects current laterally from an area that extends well beyond the contact, in contrast to previous Schottky-junction WS_2 solar cells (*76*). We hypothesize that the PTAA/Au bottom contact across the entire flake aids in collection of holes, which are the minority carriers, while the majority carrier density (electron density) is high enough for sufficient lateral conductivity to the Ag disk. In Schottky-junction devices previously fabricated by our group, where the photocurrent was limited to the top contact area, the top contact was the hole contact, and the minority carrier (hole) conductivity was not high enough for lateral conductivity to the Au disk (*76*).

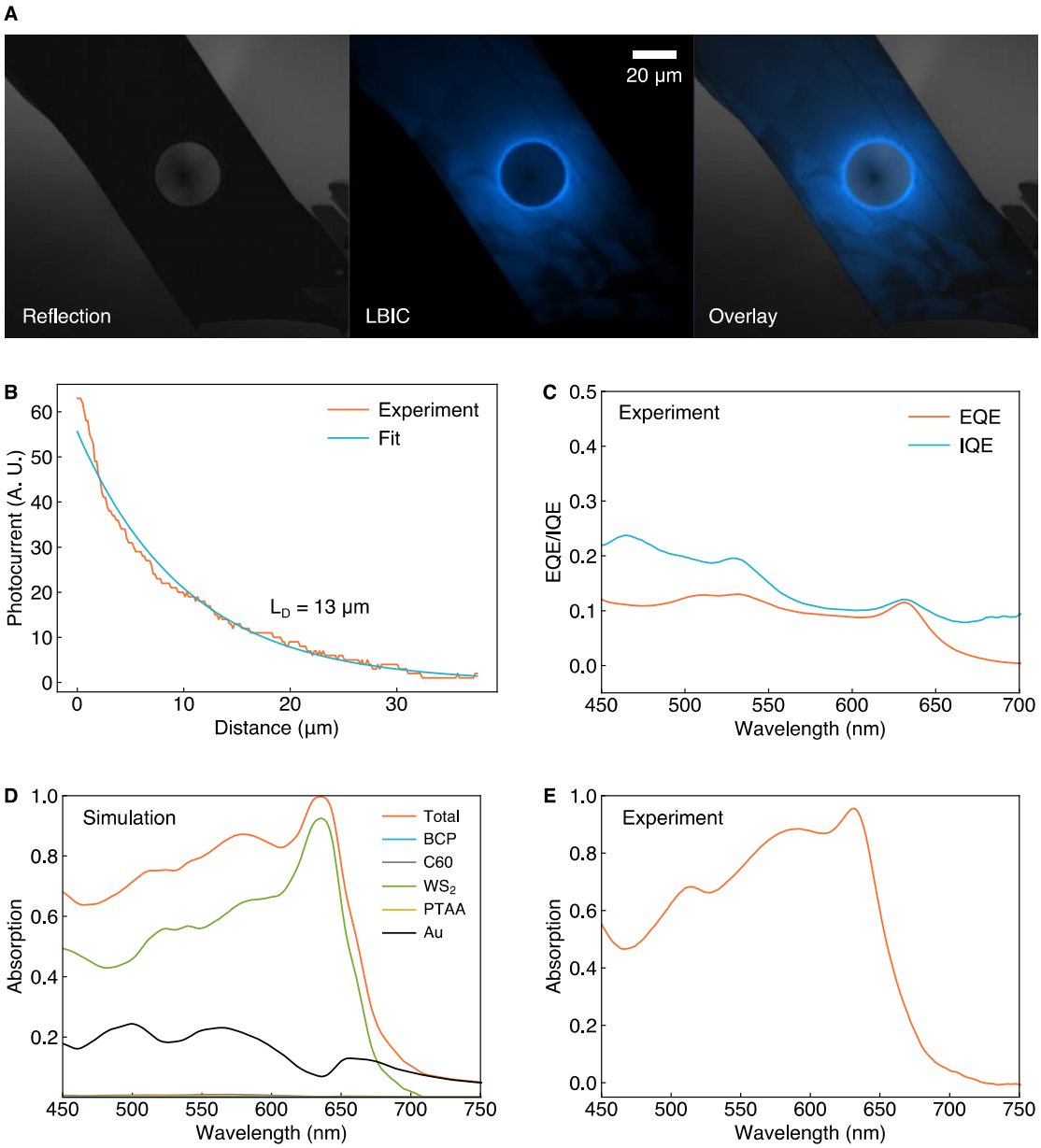

Figure 20. **Optical characterization of carrier-selective contact WS_2 solar cells.** (**A**) Reflection, photocurrent, and reflection/photocurrent overlay maps for the device. (**B**) Lateral diffusion length of electrons in the device, calculated by exponentially fitting the photocurrent profile. (**C**) Measured external quantum efficiency (EQE) and calculated internal quantum efficiency (IQE). (**D**) Absorption in the device by layer, assuming illumination off the top contact, calculated using the transfer matrix method. (**E**) Experimentally measured absorption.

Moving away from the disk, the photocurrent drops exponentially, which enables extraction of a diffusion length of 13 µm (Figure 20B). We calculate a majority carrier

lifetime of 600 ns from this diffusion length, which is longer than carrier lifetimes usually measured in TMDs because holes are readily extracted by the full-area bottom contact of the solar cell, increasing the effective lifetime for the electrons.

The external quantum efficiency (EQE) of the devices averages 10% above the A exciton when measured close to the top contact (Figure 20C). Due to the variability in photocurrent across the device, the EQE is position-dependent. We simulate the absorption in each layer of our device using the transfer matrix method (Figure 20D), with previously published optical constants for TMDs (*3*, *64*). The simulated absorption for the total device matches well with the experimentally measured absorption (Figure 20E). Both the simulated and measured absorption represent illumination away from the top contact, as the Ag disk completely shadows the device.

Dividing the EQE by the absorption implies an IQE of about 20% across the visible range. This IQE is relatively low due to the difficulty in lateral collection of electrons in this device geometry. The EQE, IQE, and short-circuit current of our devices could be substantially improved by using an ITO superstrate instead of Au, illuminating from the bottom through the ITO instead of from the top, and extending the Ag top contact beyond the flake area to serve as a back reflector. As long as there are no pinholes in the selective contacts, extending the Ag top contact beyond the flake should not cause shunting. According to transfer matrix calculations, such a device could have a short-circuit current density (J_{SC}) of 12.7 mA/cm^2 with a 15-nm-thick WS_2 active layer (Figure 21E).

We also measured devices with WSe_2 as the active layer (Figure 21). The photocurrent collection in these devices is less effective, as WSe_2 is nearly intrinsic and the lateral electron conductivity to the top contact is therefore lower (Figure 21A). In principle, n-type WSe_2 devices in this geometry, or intrinsic WSe_2 devices with ITO superstrates, could be highly efficient due to the lower bandgap (leading to higher absorption) and longer carrier lifetimes in WSe_2. According to transfer matrix calculations, such a device could have a J_{SC} of 25.0 mA/cm^2 with a 18-nm-thick WSe_2 active layer (Figure 21D).

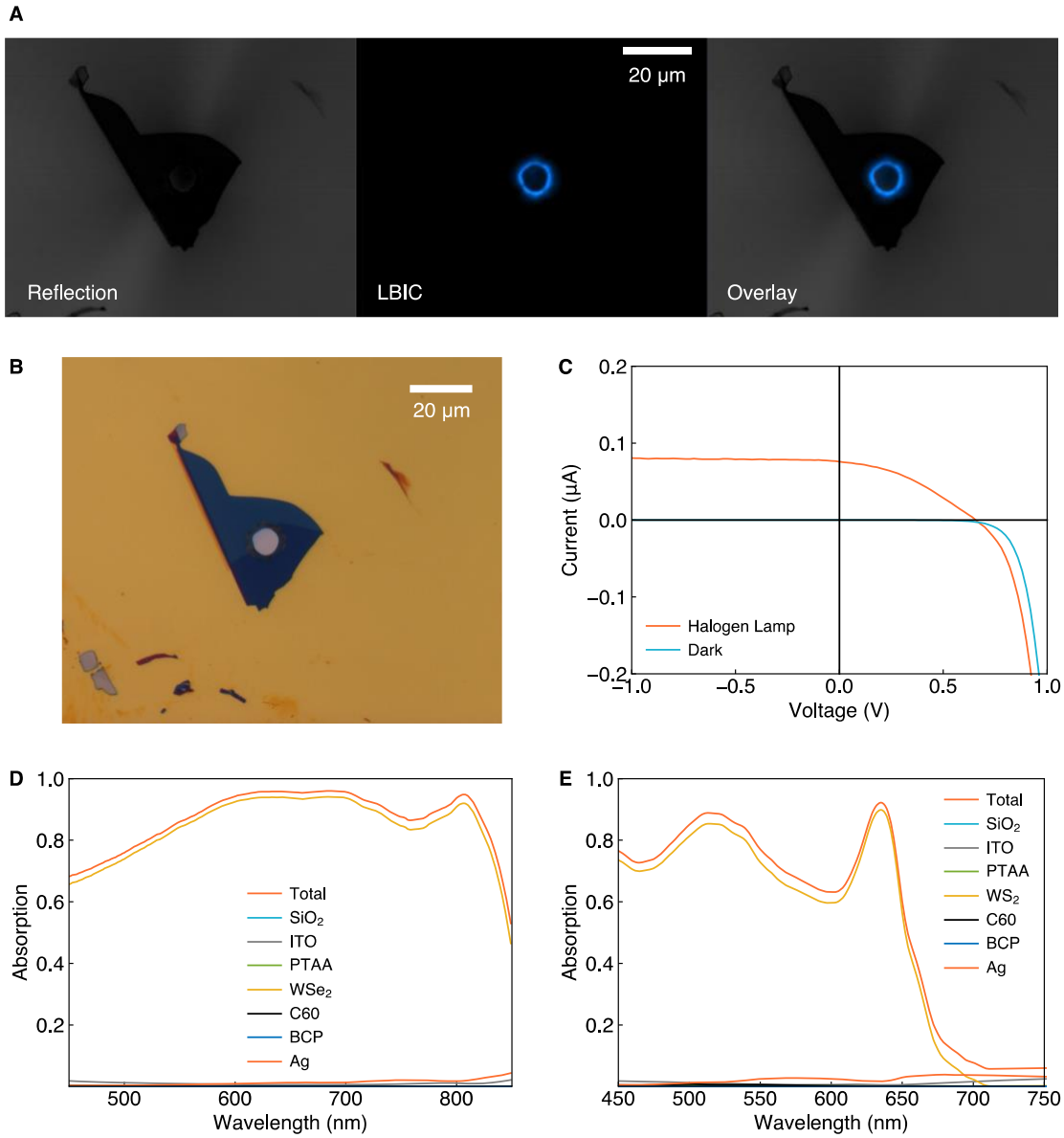

Figure 21. **WSe_2 device with the same geometry as the WS_2 device presented above.** (**A**) Photocurrent map. (**B**) Optical microscope image. (**C**) I-V characterization under illumination with a halogen lamp (~20 suns). (**D**) Absorption calculated with the transfer matrix method for a WSe_2 device with an idealized optical geometry, leading to a J_{SC} of 25.0 mA/cm^2. (E) Absorption calculated with the transfer matrix method for a WS_2 device with an idealized optical geometry, leading to a J_{SC} of 12.7 mA/cm^2.

3.5 Open-Circuit Voltage Exceeds 500 mV Under One-Sun Illumination

Under simulated AM1.5G illumination, we measure a V_{OC} of 523 mV in carrier-selective contact WS_2 solar cells (Figure 22A). We calculate a J_{SC} of 8.6 mA/cm^2 after dividing by

the device active area, as discussed below. We calculate a fill factor (FF) of 0.54, and a power conversion efficiency (PCE) of 2.4%. To our knowledge, this is the highest AM1.5G efficiency reported to date for WS_2 solar cells.

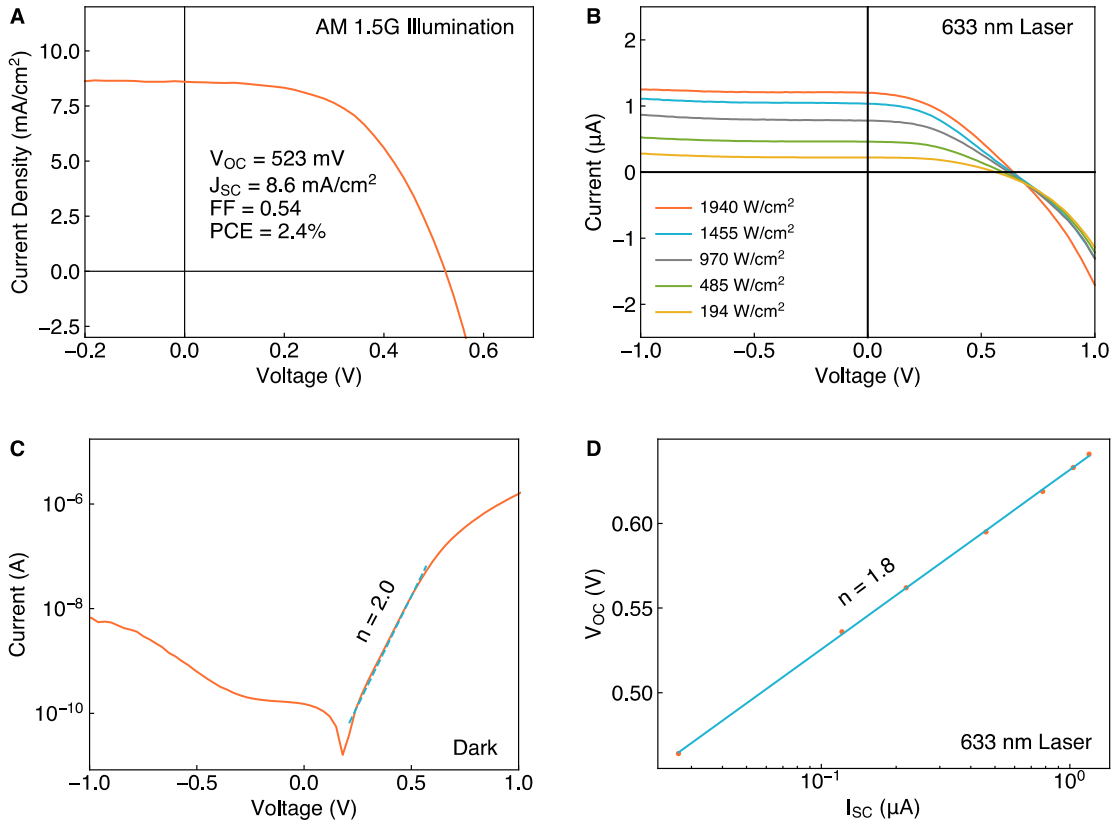

Figure 22. **Electrical characterization of a carrier-selective contact WS_2 solar cell.** (**A**) Photovoltaic performance of the device measured using an AM1.5G solar simulator. (**B**) Power-dependent I-V characteristics of the device taken under excitation with a 633 nm laser focused to a spot size of ~1 μm^2. (**C**) Dark current, fit with a nonideal diode equation with an ideality factor of 2. (**D**) Open-circuit voltage versus short-circuit current derived from (B), fit with a nonideal diode equation with an ideality factor of 1.8.

To fairly represent the potential of this device geometry, we use a device active area equal to an annulus with an inner radius of the metal disk diameter, and an outer radius of the metal disk diameter plus the measured majority carrier diffusion length (13 μm). Integrating the active layer absorption calculated using the transfer matrix method over the solar spectrum yields an implied J_{SC} of 10.1 mA/cm^2, so a J_{SC} of 8.6 mA/cm^2 would imply an active-layer IQE of 85% in devices with improved lateral current collection. This is

similar to the IQE measured in previous devices with primarily vertical transport (*34*, *39*, *76*).

If we instead assume the device active area is equal to the entire flake area, we calculate a J_{SC} of 1.5 mA/cm^2 and a power conversion efficiency of 0.42%. This is exactly equal to the implied J_{SC} calculated by integrating the EQE over the solar spectrum. This suggests that the measured EQE represents an average over the flake area, which is reasonable, as the spot size used for the EQE measurement is relatively large (~5–10 μm diameter). The diffusion-length-based definition of the active area is certainly an approximation, and the suggested device geometry described above (illuminated through an ITO superstrate, with an Ag back reflector covering the entire flake) would represent a more ideal geometry with a well-defined active area. Assuming the same V_{OC} and FF as the devices presented in Figure 22A, and the J_{SC} calculated using the transfer matrix method, these devices would have power conversion efficiencies of 3.4% and 7.1%, respectively.

Under illumination with a 633 nm laser focused to a ~1 μm^2 spot, we observe I-V curves with high fill factors even at high incident power densities (Figure 22B). Unlike previous Schottky-junction WS_2 devices, these devices do not exhibit photoshunting, suggesting that the selective contacts successfully impede hole conductivity through the electron contact and electron conductivity through the hole contact (*76*). By fitting V_{OC} versus ln(I_{SC}) from the power-dependent I-V curves in Figure 22B, we calculate an ideality factor n = 1.8 (Figure 22D). The ideality factor derived from fitting the relevant portion of the dark I-V curve is n = 2.0 ((Figure 22C). This ideality factor close to 2 suggests that Shockley-Read-Hall recombination, limited by both carrier types, is the dominant recombination process in these devices. Exciton-exciton annihilation can also affect recombination in transition metal dichalcogenides, but the expected range of carrier densities accessed here is below the carrier density threshold where this process becomes relevant, especially for multilayer TMDs with low exciton-exciton annihilation coefficients (*88*, *89*).

3.6 Matching Contact Conductance Leads to High Fill Factor

Initially, we fabricated carrier-selective contact WS_2 solar cells with 20 nm C60 ETLs and 5 nm BCP interlayers, following the perovskite literature (*80*, *82*). These devices had low fill factors and S-shaped I-V curves. S-shaped I-V curves can arise when either 1) a back-biased diode exists in the device, such as a Schottky barrier at a contact (*90*) or 2) asymmetric conductance between the electron and hole contact leads to a build-up of carriers and increased recombination within the device (*91*). We perform both simulations and experiments to show that in this case, asymmetric conductance leads to the S-shaped I-V curves that we observe in TMD solar cells (Figure 23).

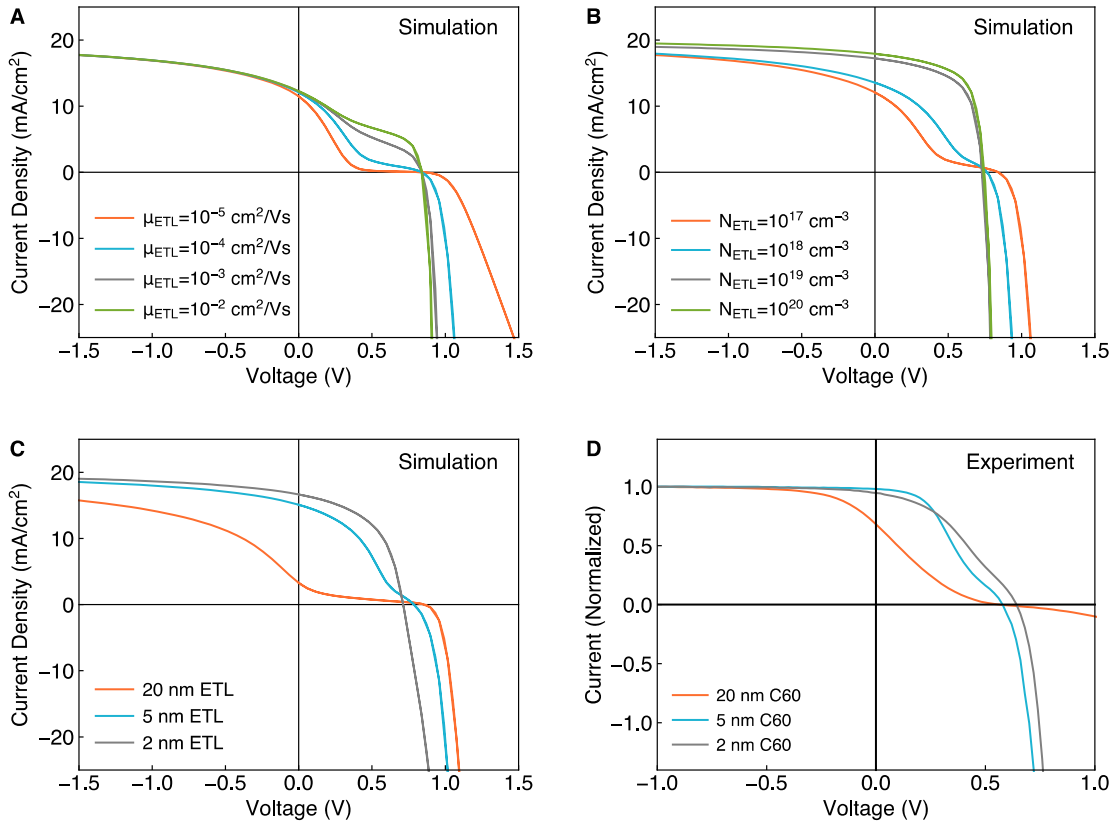

Figure 23. **Asymmetric contact conductance leads to S-shaped I-V curves.** Simulations in (A–C) performed in Sentaurus TCAD. Across all simulations, μ_{HTL} = 10^{-2} cm^2 V^{-1} s^{-1}, N_{HTL} = 10^{20} cm^{-3}, and HTL thickness is 10 nm. Where not otherwise specified, μ_{ETL} = 10^{-4} cm^2 V^{-1} s^{-1}, N_{ETL} = 10^{17} cm^{-3}, and ETL thickness is 10 nm. (**A**) Effects of varying ETL mobility on one-sun I-V curve. (**B**) Effects of varying ETL doping. (**C**) Effects of varying ETL thickness. (**D**) Experimentally measured I-V curves under halogen lamp illumination (~20 suns) with three different ETL thicknesses. Currents in (D) are normalized for comparison between devices with different active areas and WS_2 thicknesses.

We simulate our devices in Sentaurus TCAD, with the simulation parameters given in Table 2. In particular, we set the mobility and doping in the PTAA to 10^{-2} cm^2 V^{-1} s^{-1} and 10^{20} cm^{-3}, respectively, ensuring that transport through the hole contact is not limiting.

Table 2. **Parameters for device simulations in Sentaurus TCAD**. As the experimental band alignment between TMDs and PTAA/C60 is unknown, electron affinities are selected to minimize band offsets and to represent the ideal alignment for carrier-selective contact solar cells.

Parameter	**Value**	**Source**
WS_2 bandgap	1.35 eV	(*57*)
WS_2 electron affinity	3.9 eV	(*58*)
WS_2 electron effective mass	$0.63m_e$	(*59*)
WS_2 hole effective mass	$0.84m_e$	(*59*)
WS_2 doping	10^{14} cm^{-3}	HQ Graphene
WS_2 out-of-plane mobility (for holes & electrons)	0.01 cm^2/Vs	(*60*)
WS_2 DC permittivity	6.7	(*63*)
WS_2 Shockley-Read-Hall Lifetime	100 ps	Measured
C60 bandgap	1.8 eV	(*83*)
C60 electron affinity	3.9 eV	See caption
C60 DC permittivity	4.2 eV	(*83*)
PTAA bandgap	2.8 eV	(*83*)
PTAA electron affinity	2.25 eV	See caption
PTAA DC permittivity	3.5	(*83*)
Effective electron/hole density of states in CSCs	10^{20} cm^{-3}	(*83*)

Where not otherwise specified, we set the mobility and doping in the C60 to be 10^{-4} cm^2 V^{-1} s^{-1} and 10^{17} cm^{-3}, respectively, as previous studies have shown that a mobility mismatch factor larger than 100 leads to S-shaped I-V curves (*91*). We set the mobility and doping in the WS_2 to be 10^{-2} cm^2 V^{-1} s^{-1} and 10^{14} cm^{-3}, respectively, based on the doping concentration of the bulk crystal given by the crystal vendor and experimental measurements of out-of-plane mobility in TMDs (*60*). The PTAA, C60, and WS_2 thicknesses are all set to 10 nm.

The simulations show that increasing the conductance of the electron contact, by either increasing the electron mobility (Figure 23A) or the doping (Figure 23B), increases the fill factor. However, changing the mobility and the doping by one order of magnitude in the same direction does not have an identical effect, showing that the S-shape is not purely based on conductance ($G = q\mu NA/t$). This is likely because certain determinants of effective carrier collection depend more strongly on one parameter than another. For example, the ease of tunneling through a Schottky barrier from the selective contact into the electrode depends more strongly on the doping in the selective contact than on the mobility.

Varying the thickness of the suspected low-conductance contact is a powerful way to diagnose if this asymmetric-conductance effect is at play. Figure 23C shows the results of a simulation where the C60 thickness is varied, and Figure 23D shows the corresponding experimental results. In Figure 23D, the three I-V curves represent devices with different flake sizes and thicknesses, so we normalize all three I-V curves by their current density under negative bias for easier comparison. We find that we can greatly reduce the S-shape by reducing the C60 thickness from 20 nm to 2 nm, confirming that the conductance of the C60 limits the fill factor in devices with a thicker C60 layer. In our final devices, we use 2-nm-thick C60 ETLs and 2-nm-thick BCP interlayers to minimize fill factor losses.

The degree to which imbalanced carrier collection affects a device depends strongly on the carrier lifetime, as carrier recombination before collection becomes more likely as the carrier lifetime decreases. By simulating identical devices with different active-layer lifetimes, we show that solar cells with shorter active-layer lifetimes are more sensitive to

asymmetric contact conductance (Figure 24). Perovskites have a much longer lifetime than TMDs (~μs), explaining why 20-nm-thick C60 does not lead to a low fill factor in perovskite solar cells (*81*, *83*).

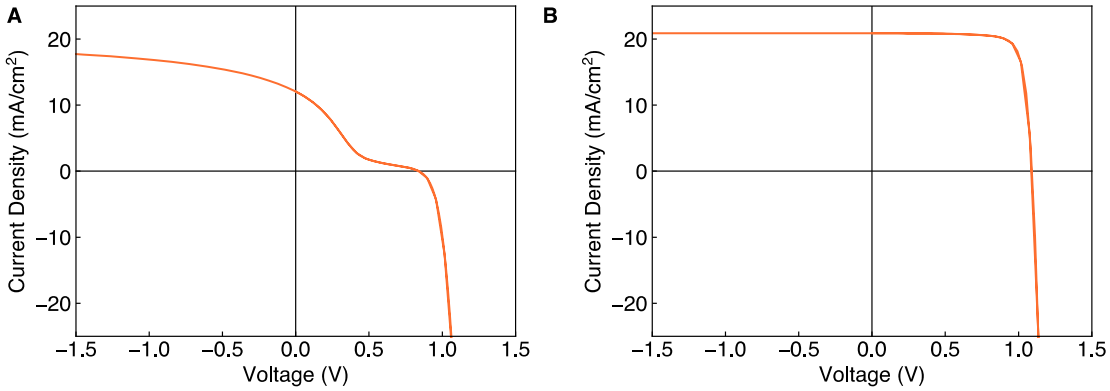

Figure 24. **Effect of lifetime in absorber layer on sensitivity to asymmetric contact conductance**. (A) Device simulated in main text, with a 100 ps lifetime. (B) Same device simulated with a 100 ns lifetime. For both simulations, μ_{HTL} = 10^{-2} cm^2 V^{-1} s^{-1} , N_{HTL} = 10^{20} cm^{-3}, and HTL thickness = 10 nm; μ_{ETL} = 10^{-4} cm^2 V^{-1} s^{-1}, N_{ETL} = 10^{17} cm^{-3}, and the ETL thickness is 10 nm.

3.7 Short Lifetimes Limit the Voltage of Intrinsic Transition Metal Dichalcogenide Photovoltaics

In carrier-selective contact devices with nearly intrinsic active layers, the carrier lifetime in the device limits the maximum achievable open-circuit voltage. The carrier concentration is related to the lifetime as $n, p = G\tau_{n,p}$, where G is the generation rate. This enables calculation of the maximum V_{OC} from:

$$V_{OC} = \frac{k_B T}{q} ln\left(\frac{(G\tau)^2}{n_i^2}\right)$$

assuming that $\tau_{n,p} = \tau$ and that the photogenerated carrier concentration exceeds the doping level. This is a reasonable assumption for multilayer TMDs, which are only lightly doped. For all four multilayer TMDs, we calculate a maximum V_{OC} based on lifetime and bandgap (Figure 25). We use the lifetimes reported in (*88*) for monolayer TMDs and the finding that the lifetimes in multilayer TMDs are usually about an order of magnitude

longer than lifetimes in monolayers (*92–94*). To calculate the generation rate, we assume that each TMD is 10 nm thick and has step-function absorption above its bandgap (as in the detailed balance efficiency limit). Since multilayer TMDs are indirect bandgap semiconductors, this represents an absolute upper limit on the generation rate, and the actual generation rate will be lower, especially in ultrathin solar cells. If the generation rate drops by an order of magnitude (resulting from either an increased thickness or nonideal optical design), the maximum V_{OC} drops by ~115 mV.

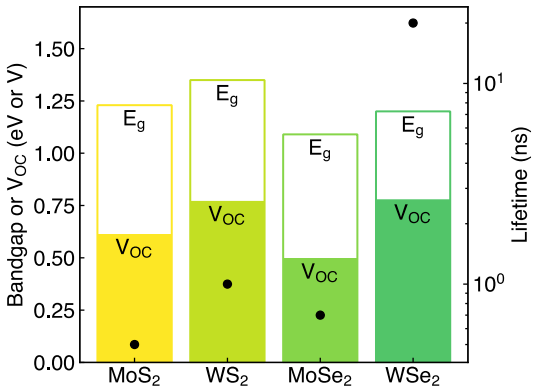

Figure 25. **Effect of carrier lifetime on the maximum open-circuit voltage of solar cells with intrinsic TMD absorber layers**. Lifetimes are plotted in black dots on the right axis. Maximum open-circuit voltages for multilayer TMDs are plotted against bandgaps on the left axis.

Figure 25 shows that in general, the short lifetimes in TMDs limit the V_{OC} in intrinsic multilayer TMD solar cells to 750 mV. This matches well with experimental observations, where one-sun voltages above 750 mV have not been reported in TMD photovoltaics (*38*). Of all four TMDs, WSe_2 has the longest lifetime and therefore the smallest $E_g - V_{OC}$ difference. Combined with its near-ideal bandgap and the small energetic separation between the indirect gap and the A exciton, WSe_2 therefore has the highest power conversion efficiency potential of any of the TMDs by a factor of 2 (~12%, as compared to ~6% for all other undoped multilayer TMDs).

To measure the lifetime in the carrier-selective contact WS_2 solar cells presented here, we measure the photoconductivity of devices with symmetric PTAA/Au top and bottom contacts (Figure 26). We calculate the minority carrier density from the photoconductivity, assuming an out-of-plane mobility of 10^{-2} cm^2 V^{-1} s^{-1}. Then, using a generation rate of

2.5×10^{22} cm^{-3} s^{-1} calculated by the transfer matrix method, we extract a minority carrier lifetime of 100 ps from photoconductivity measurements. We note that this does not agree with the majority carrier lifetime of 600 ns calculated from the diffusion length, although this can likely be explained by facile extraction of holes prolonging the effective lifetime for the electrons, as discussed above. A lifetime of 100 ps agrees with the reported lifetime for multilayer WS_2 (*89*). However, this differs from the lifetime of 1 ns assumed using the methodology in Figure 25, likely because the relation between monolayer and multilayer lifetimes is only an approximation (in particular, the lifetime vs. thickness trend in WS_2 appears to be opposite that in MoS_2 from some literature reports) (*89*, *94*). Given the generation rate calculated from the ideal short-circuit current of 10.1 mA/cm^2 for the carrier-selective contact WS_2 solar cell, and the 100 ps lifetime, the V_{OC} of the device geometry presented here is limited to 590 mV. Our measured V_{OC} of 523 mV therefore approaches the maximum possible V_{OC} for this device.

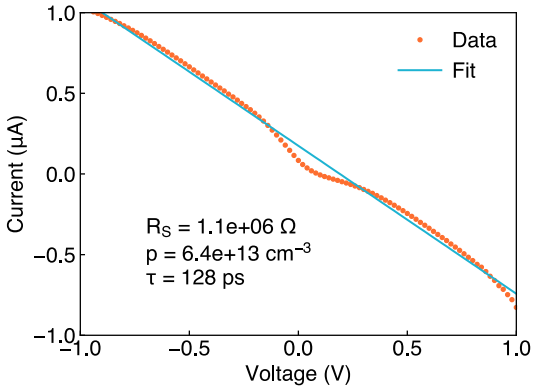

Figure 26. **Photoconductivity measurements of a symmetric WS_2 device**. Device has Au/PTAA contacts on top and bottom. Extracted lifetime is ~100 ps.

3.8 Conclusion

We show here that carrier-selective contact WS_2 solar cells based on efficient inverted perovskite device architectures, with PTAA HTLs and C60 ETLs, achieve a power conversion efficiency of 2.4% and an open-circuit voltage of 523 mV. This opens up the possibility of applying the entire library of low-cost carrier-selective contact materials developed in the perovskite photovoltaics field to TMD solar cells, and we identify selection criteria for carrier-selective contacts to mechanically exfoliated TMDs. In the

future, we note that fabricating larger-area TMD solar cells by chemical exfoliation of TMDs (*95–97*) or transfer of CVD-grown TMDs (*98–100*) could relax some of the constraints on top and bottom selective contact layers and open up a larger library of selective contacts to explore.

From photocurrent mapping, we measure a majority carrier diffusion length of 13 μm in carrier-selective contact WS_2 solar cells, and we suggest an improved device geometry that relies only on vertical carrier collection. Such a device would employ an Ag top contact/back reflector covering the entire TMD flake, and an ITO-coated glass bottom contact. As in perovskite solar cells, these devices would be illuminated from the bottom, through the ITO superstrate, which also serves as an effective anti-reflection coating for TMDs (*101*). We further suggest switching the TMD to WSe_2, which would provide the dual benefits of 1) increased absorption and 2) increased voltage due to a longer carrier lifetime. With this improved optical design and 18-nm-thick WSe_2 active layers, we show that devices with the same open-circuit voltage and fill factor as the WS_2 devices presented in this work could achieve a power conversion efficiency as high as 7%. This would represent an improvement over previous WSe_2 solar cells in terms of both thickness and efficiency (*39*).

Through comparing experiment to device simulations, we demonstrate that S-shaped I-V curves arise in devices with asymmetric carrier transport at the selective contacts. In such devices, varying the thickness of the carrier-selective contact layers is a powerful strategy for diagnosing the low-conductance contact. We use this strategy to identify that the C60 in our devices has a low conductance relative to the PTAA, and we eliminate the S-shaped I-V curves present in initial devices by decreasing the C60 thickness from 20 nm to 2 nm. We show that TMD solar cells are particularly sensitive to asymmetric contact conductance relative to perovskite solar cells due to their short carrier lifetimes.

We calculate the maximum possible V_{OC} for solar cells based on undoped, multilayer TMDs with 10-nm-thick active layers, assuming step-function absorption above the bandgap, and using literature values of carrier lifetimes. Due to the difficulty in sustaining high carrier populations and high quasi-Fermi level splitting in a material with a short

lifetime, we show that the V_{OC} is limited to ~750 mV for all four TMDs. This represents an upper limit, as devices with thicker TMDs and/or imperfect absorption above the bandgap will have lower generation rates and thus lower V_{OC}. We note that the lifetimes used here are shorter than the nonradiative lifetimes that we previously calculated from the van Roosbroeck-Shockley relation and photoluminescence quantum yield, because strong electron-hole coupling modifies the lifetime in layered semiconductors (*93*, *102*).

Normally, increasing the radiative efficiency (or photoluminescence quantum yield) of semiconductors increases their V_{OC}. Unity radiative efficiency has been demonstrated in superacid-treated monolayers (*19*). However, this approach has limited benefit in intrinsic monolayer TMD solar cells because these materials appear to have short *radiative* lifetimes, on the order of 10s of ns, which may impose a more stringent limit on V_{OC} than that imposed by radiative efficiency (*88*). That is, a monolayer TMD with unity radiative efficiency may still have a radiative lifetime of only a few ns, which would limit the voltage, even though the radiative efficiency itself would not. The radiative lifetimes in multilayer TMDs are not well characterized, and we suggest this as the subject of future work.

A path towards high-efficiency TMD photovoltaics could therefore include 1) increasing the lifetime to the radiative limit in multilayers; 2) doping the TMDs, which provides an V_{OC} limit increase of ~60 mV for each order of magnitude of doping; and 3) continuing to explore perovskite carrier-selective contacts for TMD solar cells with well-matched carrier transport at the contacts. We anticipate that with these modifications, ultrathin TMD solar cells could exceed power conversion efficiencies of 10%, which would make them promising for high-specific-power applications.

Chapter 4: Spatiotemporally Resolving Heat and Exciton Transport in Few-Layer Transition Metal Dichalcogenides

Strongly bound excitons lead to complex kinetics, spectra and transport in 2D transition metal dichalcogenides. StroboSCAT, a new pump-probe optical microscopy technique, provides unique insight into this excitonic behavior, as it allows for tracking the spatiotemporal evolution of excited charge carriers and transient spectra in the same setup. Here, we use stroboSCAT to spatiotemporally resolve heat and exciton transport in few-layer MoS_2. By probing at two different wavelengths, we find that we can observe both excitons and heat with a 705 nm probe, and heat alone with a 515 nm probe. We use temperature-dependent reflection contrast measurements to deconvolute the effects of excitons and heat, and we show that heat can dominate transient optical spectra even given small changes in temperature (10 K). We construct a kinetic model that predicts the diffusion and decay of both heat and excitons and use it to accurately fit our data. From this model, we show that exciton-exciton annihilation can dominate the kinetics even of few-layer TMDs with relatively low exciton-exciton annihilation coefficients. We develop a complete understanding of the stroboSCAT contrast we see in TMDs, preparing us to use this technique to study unanswered questions about exciton dissociation and out-of-plane transport in TMDs.

4.1 Introduction

Two-dimensional (2D) semiconducting transition metal dichalcogenides (TMDs), including MoS_2, WS_2, $MoSe_2$, and WSe_2, have been researched both as a platform for studying fundamental physics and as a basis for ultrathin optoelectronic devices (*17*, *18*). Among the newest of the TMD-based fundamental physics discoveries, Moiré superlattices have recently enabled correlated electronic states to be observed in twisted bilayers of 2D TMDs (*103–106*). With strong light-matter interactions and large absorption coefficients, 2D TMDs are also promising candidates for ultrathin and high-specific-power photovoltaics (*23*, *34*, *39*, *76*). Both the fundamental physics studies and the device applications benefit from strongly bound excitons in 2D TMDs (*107*). Yet these strongly

bound excitons also result in complex kinetics and transport that can be difficult to interpret.

To study the kinetics of TMDs, researchers often turn to time-resolved photoluminescence measurements (TRPL). Early in the growth of the 2D TMD research field, the Heinz group used TRPL measurements to show the existence of strong exciton-exciton annihilation (EEA) in monolayer MoS_2 (*108*). EEA is an excitonic analog of an Auger-Meitner-like process in which one exciton is annihilated by nonradiatively transferring its energy to another exciton. That excited (hot) exciton can then nonradiatively decay to the band edge and then radiatively (or nonradiatively) recombine from there. The rate equation that describes this process is:

$$\frac{dN_X}{dt} = R_A N_X^2$$

where N_X is the number of excitons and R_A is the exciton-exciton annihilation rate constant. For monolayer TMDs, R_A has been shown to be on the order of 10^{-2}–10^{1} cm^2/s (*88*, *108*–*110*). R_A can also depend strongly on the substrate, decreasing by over two orders of magnitude when a TMD is placed on a high-index substrate or encapsulated with hBN (*111*, *112*). The solution of the rate equation above is:

$$N_X(t) = \frac{N_0}{1 + R_A N_0 t}$$

where N_0 is the initial carrier distribution. This $1/x$-like equation displays a fast decay at earlier times, and a slower decay at later times. As such, some researchers have assigned bi-exponential or tri-exponential fits to TRPL data without taking into account the effects of EEA, where $1/x$-like fits could perhaps more accurately fit the data (*113*, *114*).

Techniques to study the kinetics along with the transient spectra of TMDs include transient absorption and transient reflection spectroscopy (*115*). These measurements have revealed ultrafast (< 1 ps) thermalization in TMDs (*109*, *116*, *117*); multiple effects of excitons on spectra including carrier-induced broadening, bandgap renormalization, exciton binding energy reduction, and Pauli blocking (*118*–*120*); multiple effects of heat on spectra

including temperature-induced bandgap shift and broadening (*110*); and even a Mott transition above carrier densities of 10^{14} cm^{-2} (*121*). Figure 27 depicts some of these transient optical effects.

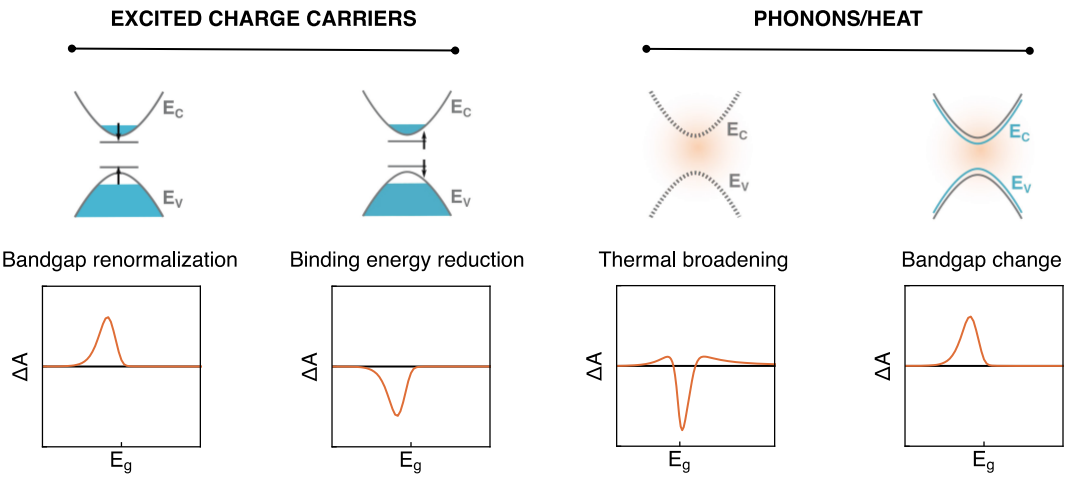

Figure 27. **Transient optical effects in two-dimensional semiconductors.** Excited charge carriers, in the form of bound excitons, can affect transient optical spectra via screening the exciton binding energy, which competes with bandgap renormalization. Heat can affect transient optical spectra via thermal broadening or via a temperature-induced bandgap shift.

With the competing effects of excitons and heat, and with multiple exciton peaks (A, B, and C) nearly overlapping spectrally, transient spectra in TMDs quickly become complicated to interpret (*118*). In one of the most complete analyses of transient spectra to date, the Heinz group tracked a single exciton peak—that of the A exciton—and identified the phenomena at play during the duration of the measurement (*110*). At early times, the presence of excited excitons dominates the changes to the A exciton peak. When excitons are present, two competing effects take place: they screen the Coulomb attraction between other excitons, reducing the exciton binding energy, but they also screen the Coulomb repulsion between like carriers, causing a reduction in the bandgap that is referred to as bandgap renormalization (*110*, *122–125*). The net effect of these two phenomena can be either a slight redshift or a blueshift in exciton peak positions. Here, the Heinz group observed a redshift in the A exciton peak, as well as broadening due to excitation-induced dephasing and suppression due to Pauli blocking. As a result of EEA, the majority of the excitons decay on the order of tens of picoseconds, depositing significant heat into the

lattice. Therefore, at late times, the presence of heat dominates the changes to the A exciton peak. This peak then experiences phonon-induced broadening and redshifting due to the temperature-dependent bandgap change (*110, 126*). Focusing in on a single peak in this way is a helpful way to deconvolute the many effects at play—and yet, the analysis is still complex.

To study diffusion and transport in TMDs, one powerful technique is time-resolved photoluminescence microscopy. Recently, these measurements have been used to show exciton halos forming in monolayer TMDs, where the excitons (and therefore the emitted photons) form a ring around a dark spot in the center (*112, 127, 128*). These exciton halos have been attributed to a Seebeck effect arising from local heating due to EEA. EEA occurs primarily in the center of the Gaussian pulse of excited carriers, where the exciton density is highest, causing a hot spot to form in the center. The resulting temperature gradient drives carriers out of the center region due to the Seebeck effect, in which thermal drift drives the motion of carriers from hotter into colder regions. However, photoluminescence can only be used to access bright carriers, and cannot probe heat or carriers that recombine nonradiatively. Further, multilayer TMDs in particular have low photoluminescence quantum yields, making time-resolved photoluminescence measurements of high enough sensitivity challenging.

We have so far outlined here a number of challenges in interpreting kinetics, transient spectra, and transport of TMDs related to their excitonic behavior. EEA can cause nonlinear rate equations for exciton decay, even at moderate exciton densities and small EEA coefficients. EEA can also generate a significant amount of heat, which can lead to non-diffusive carrier transport due to the Seebeck effect. Finally, since the absorption spectrum of TMDs exhibits multiple excitonic peaks rather than a single quasiparticle bandgap, transient spectra can become quite complex as the effects from neighboring excitonic peaks overlap spectrally.

Temporal separation, as employed by the Heinz group in (*110*), is a powerful way to deconvolute the effects of different types of energy carriers on kinetics, spectra, and transport. Adding spatial separation can be even more powerful. The stroboSCAT

technique, developed in 2018 by the Ginsberg group at UC Berkeley, allows researchers to simultaneously track kinetics and transport of excited carriers, and to measure spectra in the same setup (*129*). In stroboSCAT, a focused pump excites a pulse of carriers, and a widefield probe images those carriers at different delay times in an imaging mode that is sensitive to scattering rather than specular reflection. StroboSCAT boasts high sensitivity, access to dark carriers, and the ability to measure out-of-plane as well as in-plane transport. By examining the spatiotemporal evolution of stroboSCAT and spectroSCAT (spectrally resolved stroboSCAT) data, we deconvolute the effects of heat and excitons on the kinetics, spectra, and transport of excited carriers in few-layer TMDs. We demonstrate that even small amounts of heat can have a dominant effect on transient spectra, and that EEA is still important to consider in few-layer samples. By developing a thorough understanding of stroboSCAT data on few-layer TMDs, we prepare for this technique to be used to explore even more novel questions about TMDs.

4.2 The StroboSCAT Technique

Figure 28 shows the experimental setup for stroboSCAT. More details can be found in (*129*).

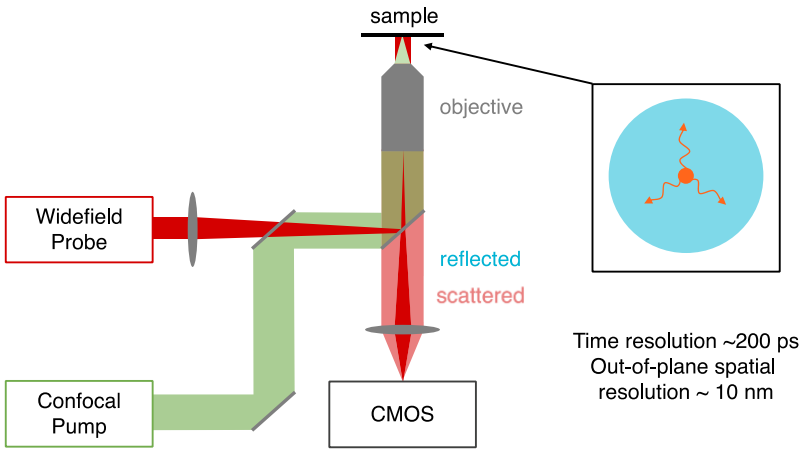

Figure 28. **Setup for stroboSCAT experiments.** A confocal pump beam fills the back focal plane of the objective, creating a focused spot at the sample that excites a Gaussian distribution of carriers. A widefield probe beam is focused at the back focal plane of the objective, imaging the full field of view at the sample.

A confocal pump beam is collimated to fill the back focal plane of the objective, creating a focused spot at the sample. A probe beam is focused on the back focal plane of the objective, creating a collimated, widefield beam at the sample. The pump beam therefore excites carriers in a localized spot, and the probe beam images the entire field of view. By changing the delay time between the pump and the probe, we collect a series of images of the generated carriers at different times after excitation (Figure 29). This enables us to observe the spatiotemporal evolution of an excited carrier population.

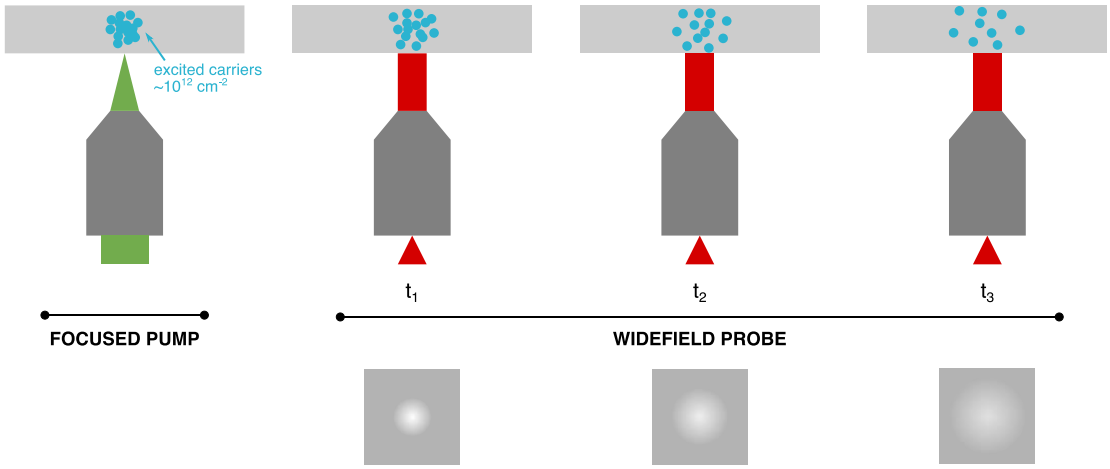

Figure 29. **How stroboSCAT works.** A focused pump excites a pulse of carriers with a Gaussian spatial distribution. A widefield probe comes in at a later time and scatters off the excited carriers, imaging their distribution. By changing the delay between the pump and the probe, stroboSCAT tracks the spatiotemporal evolution of the excited energy carriers.

StroboSCAT is based on interferometric scattering, or iSCAT, a technique for imaging small particles. Both iSCAT and stroboSCAT mainly image the interference of scattered light from the sample with light reflected at the substrate-sample interface, leading to high sensitivity. The iSCAT signal can be described as (*129*):

$$I_d = E_i^2[r^2 + |s|^2 + 2r|s|\,cos\,\phi]$$

where I_d is the signal on the detector, E_i is the incident electric field, r is the reflection coefficient at the sample-substrate interface and s is the scattering coefficient, and ϕ is the phase difference between scattered and reflected light. The interferometric cross term $2r|s|\,cos\,\phi$ dominates the iSCAT contrast. The phase difference ϕ is equal to (*129*):

$$\phi = \phi_{gouy} + \phi_{scat} + \frac{4\pi z n}{\lambda}$$

where ϕ_{gouy} is the focusing or Gouy phase, which is tuned to $-\pi \leq \phi_{\mathrm{gouy}} \leq -\pi/2$ in stroboSCAT to maximize contrast due to scattering; ϕ_{scat} is the scattering phase, which is generally negligible; and the final term represents a phase change due to the distance that the object has traveled away from the sample-substrate interface, since the scattered light path length will change if the scatterer moves in z. The differential stroboSCAT signal can therefore be approximated as (*129*):

$$\frac{I_{pumpON} - I_{pumpOFF}}{I_{pumpOFF}} = \frac{2\cos\phi\left(\left|s_{pumpON}\right| - \left|s_{pumpOFF}\right|\right)}{r}$$

where the $\cos\phi$ term will be approximately equal to –1 for processes occurring at the sample surface, but will vary for processes occurring deeper within the sample.

The higher sensitivity of stroboSCAT to scattered light relative to techniques like transient reflection has been confirmed through the following experiment: an aperture is placed at the back focal plane of the objective. Reflected light from the sample will primarily be oriented normal to the sample plane, and since the back focal plane of the objective is a Fourier transform of the imaging plane, the reflected light will be spatially located in the center of the back focal plane. Scattered light, which is scattered into the objective at large angles, will be spatially distributed across the entire back focal plane. When the aperture at the back focal plane of the objective is closed, it therefore first attenuates the scattered light, and only when it is almost fully closed will it block the reflected light. The stroboSCAT signal is almost fully attenuated by the aperture before the normally reflected beam is blocked, demonstrating that the stroboSCAT signal is dominated by scattering. Further, when the aperture is closed enough to allow only the normally reflected light to pass through, the signal is much lower than when scattering is included, demonstrating that scattering is detected to a higher sensitivity than reflection alone.

In their simplest form, stroboSCAT measurements appear as a Gaussian distribution of carriers expanding in space and decaying in time. Previously, stroboSCAT measurements

like these have been used to measure the diffusivity of electrons and heat in silicon, charge carriers in perovskites, and excitons in organic semiconductors (*129*). More complex stroboSCAT images arise when there is a correlation between morphology and transport, or when multiple types of carriers are simultaneously present in a sample. As such, stroboSCAT has also been used to demonstrate preferential transport along the long axis of grains in an organic semiconductor, and to demonstrate that grain boundaries block lateral carrier transport in perovskite films (*129*).

Compared to similar pump-probe microscopy techniques such as transient absorption microscopy or photoluminescence microscopy, stroboSCAT has a number of advantages (Figure 30).

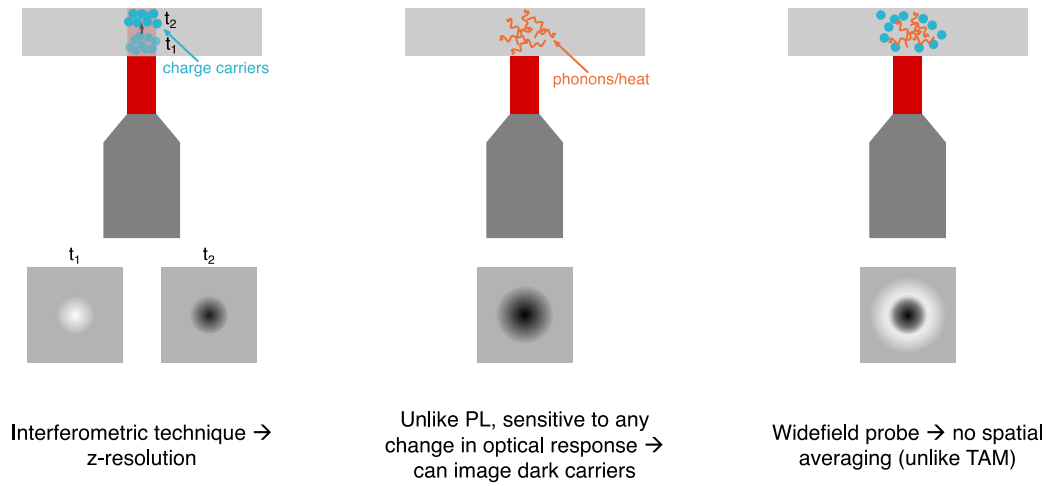

Figure 30. **Advantages of stroboSCAT.** Because stroboSCAT images the interference between the reflected light from the sample-substrate interface and the scattered light from the excited carriers, it is sensitive to out-of-plane transport of charge carriers. Unlike photoluminescence, it is sensitive to any change in complex refractive index, so it can image dark carriers. A widefield probe allows for rapid spatial imaging.

First, because the signal arises from the interference of the scattered light with the reflected light off the sample-substrate surface, stroboSCAT is sensitive to carrier transport in the out-of-plane or z-direction: after carriers have traveled a certain distance into the material (specified by $z = \lambda/4n$), there will be a π phase flip and the contrast will change sign. Second, stroboSCAT is sensitive to any excited carriers that change the complex refractive index, so it can image dark carriers and heat as well as carriers that recombine radiatively

(unlike photoluminescence). Third, the widefield probe enables rapid spatial imaging without scanning a probe beam or averaging over a large area of the sample. These three advantages make stroboSCAT a particularly suitable technique for studying TMDs, as 1) many of the outstanding questions about carrier transport in TMDs relate to out-of-plane transport between the van der Waals layers, 2) dark carriers play a dominant role in exciton decay kinetics, and 3) several interesting phenomena have been observed while imaging transport, including the exciton halos described above.

StroboSCAT can achieve lateral resolution on the order of a few nanometers, vertical resolution on the order of tens of nanometers, and time resolution on the order of 100 ps (with the currently implemented diode lasers). By using a white light probe and dispersing the wavelengths using a prism or a spectrometer, it can also provide spectral information, in a measurement configuration called spectroSCAT.

4.3 Interpreting StroboSCAT Data

To accurately interpret stroboSCAT data, we must develop a microscopic picture of the technique. This is pictorially shown in Figure 31.

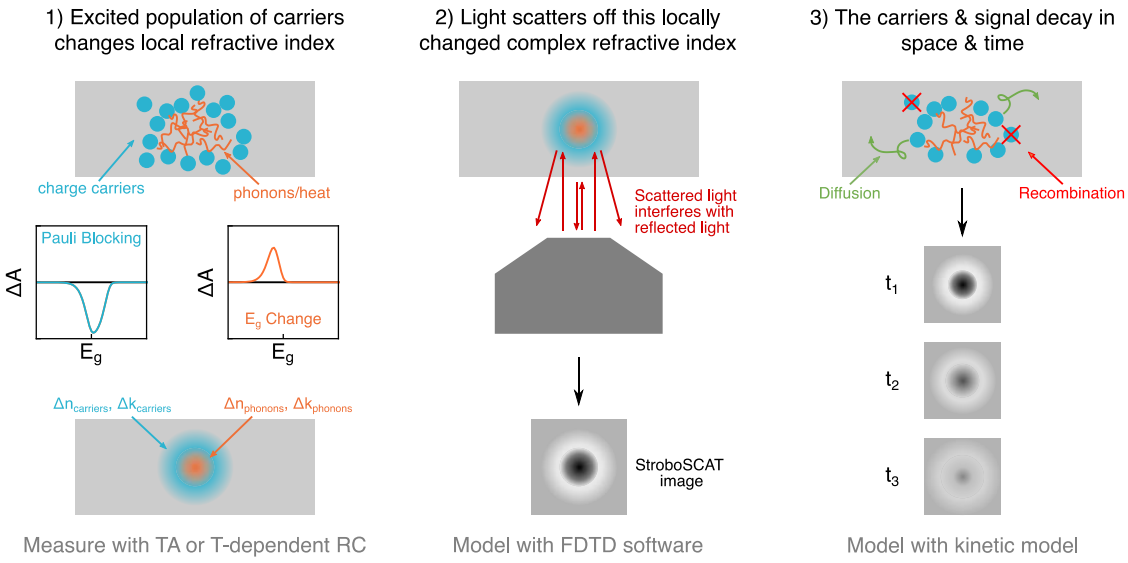

Figure 31. **Interpreting stroboSCAT measurements.** First, an excited population of carriers changes the local refractive index in the material. Second, light scatters off this locally changed complex refractive index. Third, the carriers and signal decay in space and time.

First, the pump beam excites a local pulse of carriers that spatially matches the Gaussian distribution of the pump beam. Since thermalization occurs on the order of hundreds of femtoseconds, all charge carriers are thermalized by the first stroboSCAT image at 100 ps, meaning that the charge carrier temperature is equal to the lattice temperature (*109, 116, 117*). The presence of each of the types of excited energy carriers that are present—electrons, holes, excitons, and phonons/heat—can change the local refractive index in different ways. For example, as discussed in Section 4.1, the presence of heat can broaden resonances and can shift the material's bandgap (*110, 126*). The presence of excitons can screen the Coulomb attraction between electrons and holes, reducing the exciton binding energy. As discussed in Section 4.1, this reduction in binding energy competes with bandgap renormalization, and can lead to either a net redshift or blueshift in exciton resonances (*110, 122–125*). Together, these different effects of excited carriers effectively lead to a different complex refractive index before excitation and after excitation. If, for example, two types of carriers are present with different spatial distributions, the new complex refractive index after excitation can vary with position on the sample.

It is important to note that the presence of excited carriers can affect the material's refractive index across a wide range of wavelengths, and not just near the resonance corresponding to that type of carrier. For example, although the A exciton in MoS_2 occurs close to 650 nm, the presence of A excitons in the system can affect *all* exciton resonances by screening the exciton binding energies. So, the presence of A excitons can appear not only as spectral features close to the A exciton, but also close to the B and C excitons. Similarly, heat does not only appear near phonon-polariton resonances in the infrared: it shifts the bandgap and therefore changes the complex refractive index across the visible range. Excited-state absorption or intraband absorption is another example of this, though it is usually not a dominant effect in TMDs.

The net effect of the presence of excited carriers on a material's complex refractive index can be measured by transient absorption, transient reflection, or spectroSCAT, all of which essentially measure the difference in the complex refractive index with and without the presence of excited carriers. In general, transient absorption is more sensitive to changes in k, and transient reflection and spectroSCAT are more sensitive to changes in n. However,

in the case of a transparent substrate covered by an ultrathin layer, reflectance (and therefore transient reflection/spectroSCAT) is also dominated by changes in k (*110*).

If different types of carriers are present and excited carriers affect spectra in multiple ways, as is often the case, distinguishing which types of excited carriers are being imaged can be challenging. The contributions from different types of carriers to transient spectra will be additive, so if two different populations affect transient spectra in opposite ways (e.g. one population decreases absorption below the bandgap and one increases it), they may cancel out and become difficult to deconvolute. Temperature-dependent reflection contrast can separate the effects of heat and charge carriers, and we performed these measurements on TMDs (Section 4.6). In stroboSCAT, different types of carriers can have different diffusivities and therefore spatial extents at later times, which can also help distinguish different types of carriers.

Second, the probe beam scatters off this locally changed refractive index. Where there are excited carriers—usually in a Gaussian distribution created by the pump laser—the refractive index will differ from the surrounding material. This region can be thought of as a Mie scatterer, which has a size on the order of the wavelength of the probe light. The scattered light from this Mie scatterer interferes with the reflected light off the sample-substrate interface to create a stroboSCAT image.

We find it more instructive to think of the probe scattering off a region with a locally changed refractive index rather than scattering off a group of individual light scatterers (i.e. individual excitons, or phonons). Individual excitons and phonons are deeply subwavelength particles that cannot individually scatter an appreciable amount of light—small even in comparison to molecular Rayleigh scatterers. The complex refractive index is a tool for understanding the collective effects of all of the carriers in a material. So, we find it most useful to think about the effects of excited carriers in terms of how they change the complex refractive index, and subsequently to relate the scattering to that locally changed complex refractive index.

An optical solver such as Lumerical FDTD would be needed to accurately calculate or predict the scattering that creates stroboSCAT images. Transfer matrix calculations cannot

predict this, since they calculate only reflected light, and the aperture experiment described in Section 4.2 demonstrates that scattered light dominates stroboSCAT contrast. If the change in complex refractive index due to excited carriers were known from transient reflection, transient absorption, or temperature-dependent reflection contrast, that refractive index could be used as an input to a Lumerical FDTD simulation. One could set up a Gaussian profile that had a different refractive index than the surrounding material, and calculate the scattered and reflected light relative to the ground state of the material. We did not do these calculations for the TMDs that we measured due to the complexity in decoupling the effects of the different carriers present, but we suggest it as the subject of future work.

Third, the carriers diffuse in space and decay in time, and the stroboSCAT contrast diffuses and decays accordingly. This can be modeled with a kinetic model that captures all relevant diffusion and decay channels for the carriers. We develop a kinetic model to model the spatiotemporal evolution of our StroboSCAT data in Section 4.7.

We have therefore developed a complete, microscopic picture of stroboSCAT contrast. In summary, in order to predict or model stroboSCAT images for a certain material, we need to 1) understand how an excited population of carriers changes the material's refractive index, through transient reflection, transient absorption, or temperature-dependent reflection contrast; 2) know how light scatters off this locally changed refractive index, through FDTD simulations; and 3) model how the carriers and therefore the signal diffuse in space and decay in time.

4.4 Fabricating hBN-Encapsulated Few-Layer MoS_2 Samples

To fabricate samples for stroboSCAT, we use the hot pick-up technique to fabricate hBN-encapsulated few-layer MoS_2 heterostructures on coverglass (*130*). Briefly, hBN and MoS_2 are exfoliated onto 285 nm of thermally oxidized SiO_2 on Si. We make stamps consisting of PDMS covered with a thin film of the thermoplastic polymer polycarbonate (PC). Using these stamps, we first pick up the top hBN, then the desired MoS_2 flake, and then the bottom hBN, all at 50ºC. We drop the stack off onto #1.5 coverglass, which serves as the substrate for all stroboSCAT measurements, at 180ºC, and then dissolve the PC in chloroform.

We characterize these samples using optical microscopy, Raman spectroscopy, and atomic force microscopy (AFM) (Figure 32). The few-layer MoS_2 flake is outlined in blue in Figure 32A. The AFM images in Figure 32B show that our samples have large, homogeneous, bubble-free areas, which are ideal for measuring in stroboSCAT. The separation between the two MoS_2 Raman peaks demonstrates that these samples are about 4 layers thick (Figure 32C–D). We also fabricate bare MoS_2 samples by exfoliating directly onto PDMS and then transferring onto coverglass.

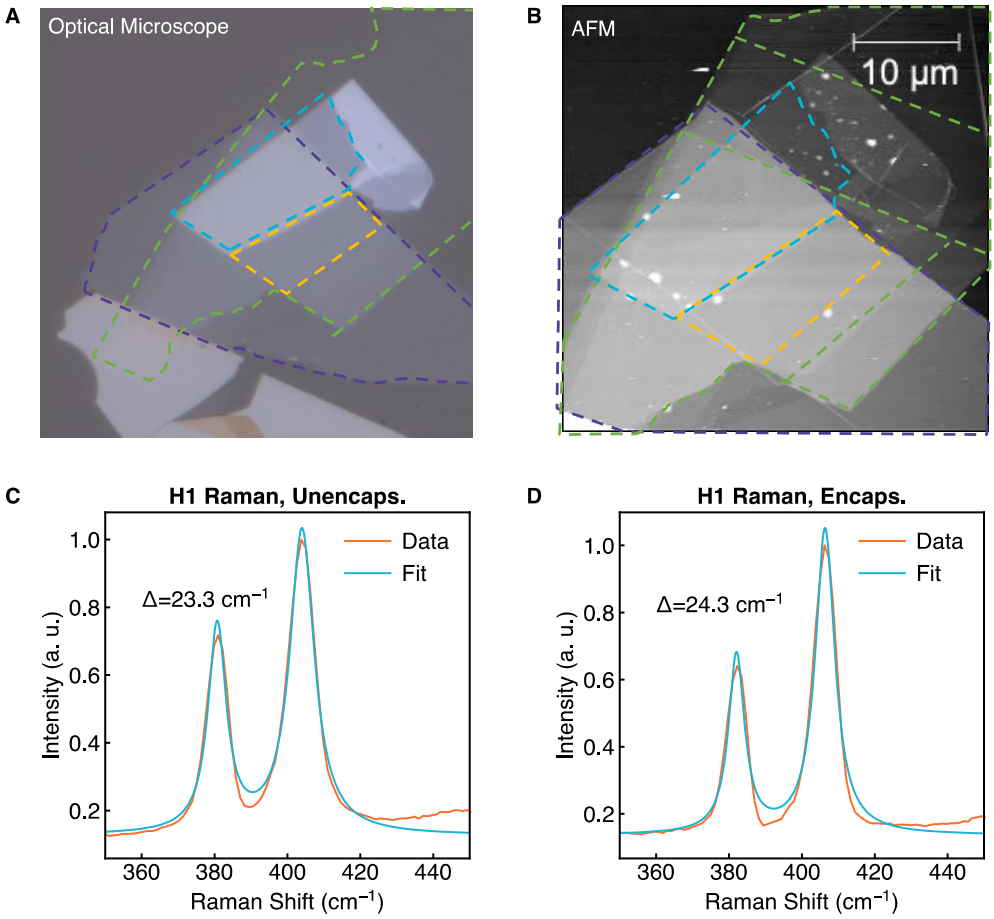

Figure 32. **Encapsulated few-layer MoS_2 samples.** (**A**) Optical microscope image of hBN-encapsulated MoS_2. (**B**) Atomic force microscopy scan of sample. (**C, D**) Raman spectroscopy of unencapsulated (**C**) and encapsulated (**D**) region, demonstrating MoS_2 thickness of 4 layers.

4.5 StroboSCAT Measurements on Few-Layer MoS_2

Figure 33 presents stroboSCAT data on both bare and encapsulated few-layer MoS_2 samples, measured by the Ginsberg group. The pump beam has a wavelength of 440 nm, a width of 72 ps, and a repetition rate of 10 MHz. The excitation power density is 35 μJ/cm^2 for the encapsulated sample and 20 μJ/cm^2 for the bare sample, from which we calculate a peak carrier density in the center of the Gaussian pulse of 1.85×10^{13} cm^{-2}. This is below the Mott transition threshold of 10^{14} cm^{-2} (*121*). The probe beam has a wavelength of either 515 nm or 705 nm and a width of 108 or 60 ps, respectively.

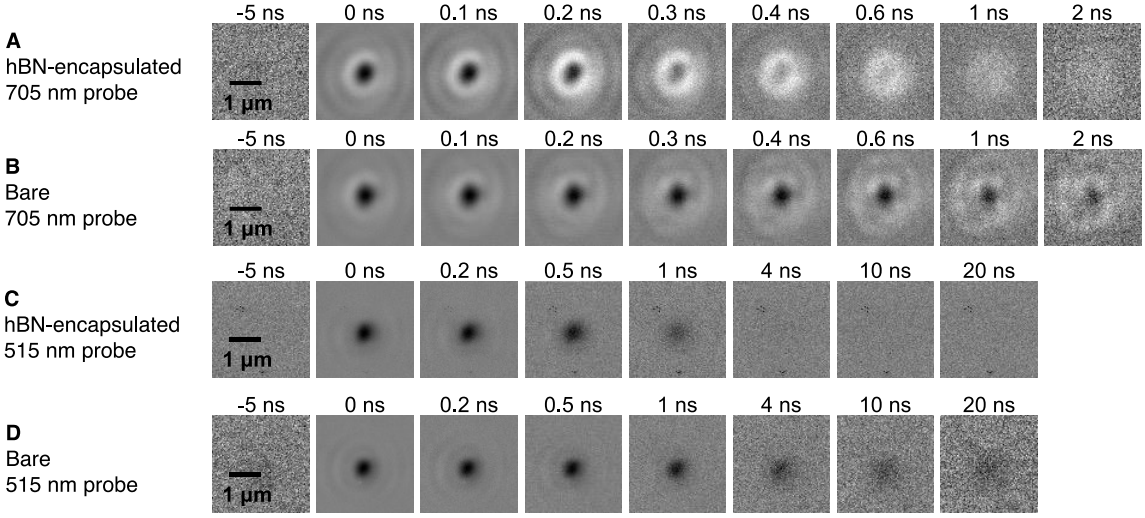

Figure 33. **Raw stroboSCAT images.** (**A**) StroboSCAT data on an hBN-encapsulated few-layer MoS_2 sample, imaged with a 705 nm probe. (**B**) StroboSCAT data on a bare (unencapsulated) few-layer MoS_2 sample, imaged with a 705 nm probe. (**C**) StroboSCAT data on an hBN-encapsulated few-layer MoS_2 sample, imaged with a 515 nm probe. (**D**). StroboSCAT image of a bare few-layer MoS_2 sample, imaged with a 515 nm probe. All StroboSCAT images are normalized to show maximum contrast, and absolute intensity should not be compared between images.

Figure 33A presents the stroboSCAT data for the hBN-encapsulated MoS_2 probed at 705 nm, and Figure 33B presents the same data but for the bare (unencapsulated) sample. Figure 33C presents the data for the hBN-encapsulated sample probed at 515 nm, and Figure 33D presents the same data but for the bare sample. We notice that two types of contrast—bright and dark—are present in the data probed at 705 nm, and one type of contrast—dark only—is present in the data probed at 515 nm. Each stroboSCAT image is

normalized to the put the maximum positive/negative contrast at each contrast bound, so that the background is represented as grey in the middle of the scale, which makes the decay over time more clearly visible. Therefore, the magnitude of the contrast cannot be directly compared between two images. There are some irregularities in the bare, 705-nm data, due to bubbles in the sample, but these disappear upon radial averaging (Figure 34). The bright contrast in the 705 nm data has a larger spatial extent than the dark contrast. These images immediately appear reminiscent of the exciton halos described in Section 4.1, although it is also possible that we are simply observing the sum of a wider positive Gaussian with a smaller amplitude and a narrower negative Gaussian with a larger amplitude. This will be addressed in Section 4.6. At both probe wavelengths, the dark contrast decays faster in the hBN-encapsulated sample than in the bare sample.

If two signs of contrast are present at a single probe wavelength, there must be two populations present which have opposite effects on the complex refractive index at that probe wavelength. (There is an exception to this: when probed near a zero-crossing in a transient spectra, it is possible for a single population to flip contrast sign as it decays. See, for example, Figure 36B around 625 nm, where the contrast would start out negative at high temperatures and become positive at low temperatures. However, we do not see a contrast flip at later times in our stroboSCAT data as the populations decay, so we rule that out here.) The dark contrast appears to have the same radial extent, diffusivity, and kinetics at both 705 nm and at 515 nm, so it is likely caused by the same type of excited energy carrier. Since transient spectra fluctuate between positive and negative as a function of wavelength, it would be possible for a single type of excited energy carrier to have the opposite contrast sign at a different probe wavelength (e.g. the type of carrier that causes dark contrast at 705 nm could cause bright contrast at 515 nm), but this does not appear to be the case here.

We tentatively assign the dark contrast to heat at both probe wavelengths and the bright contrast to excitons at 705 nm. There are two main pieces of evidence for this. First heat would decay more quickly in hBN-encapsulated samples, as hBN serves as an effective heat sink for TMDs, so this explains the faster decay of dark contrast at both probe wavelengths (*131*). Second, excitons have a higher diffusivity than heat in TMDs,

explaining the larger spatial extent of the bright population at 705 nm (*127*, *128*, *131–134*). Below and in Section 4.6, we further substantiate this contrast assignment.

The radially averaged profiles in Figure 34, which are no longer normalized to show maximum contrast, show the same trends. We clearly observe a faster decay of dark contrast in the hBN-encapsulated samples. Again, this corroborates the assumptions that 1) the dark contrast is heat and 2) the dark contrast is caused by the same population at both probe wavelengths. These profiles have been corrected for the different point-spread functions of the two probe lasers, and after these corrections, we can directly compare the spatial extent of the bright contrast to that of the dark contrast. The radius of the dark contrast is similar at both probe wavelengths, and it is much smaller than the radius of the bright contrast. This quantitatively corroborates the assumption that the bright and the dark populations at 705 nm represent two different populations.

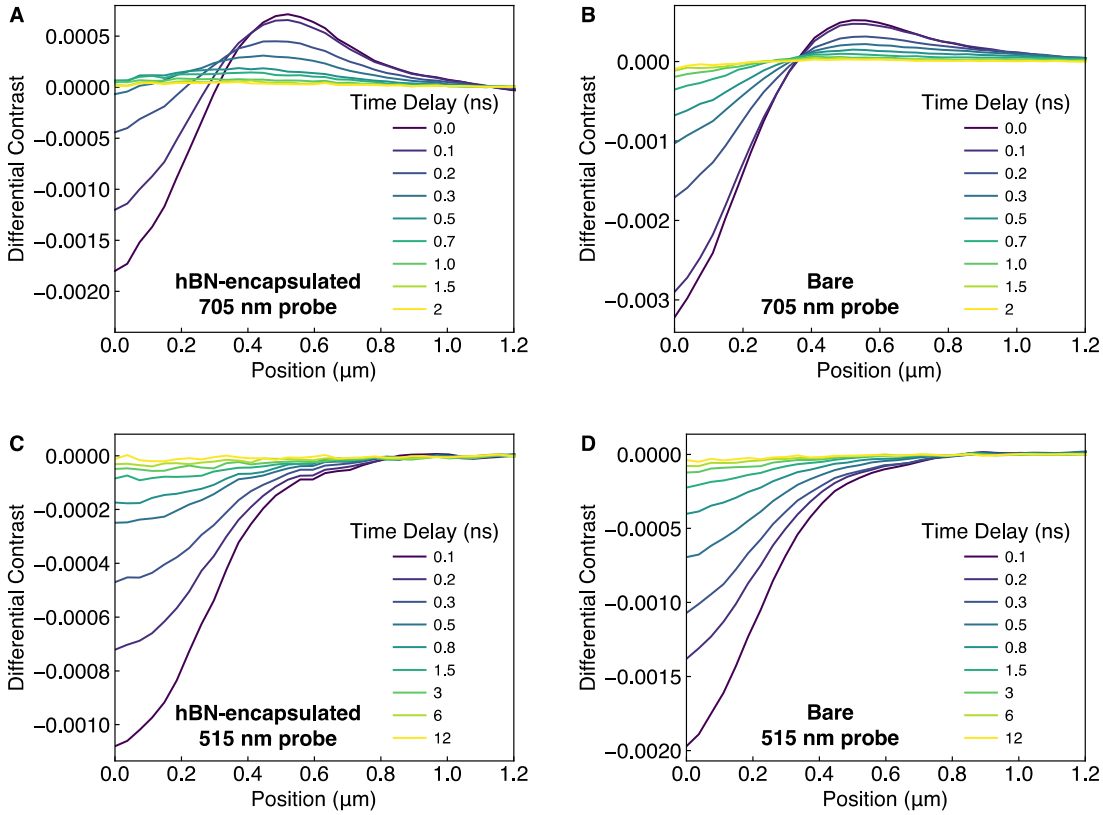

Figure 34. **Radially averaged StroboSCAT profiles.** (**A, B**) Profiles for hBN-encapsulated (**A**) and bare (**B**) samples imaged with the 705 nm probe. (**C, D**) Profiles for hBN-encapsulated (**C**) and bare (**D**) samples imaged with the 515 nm probe. Radial profiles have been corrected for the different point-spread-functions of the two probes.

Figure 35 shows the kinetics of the bright contrast and the dark contrast separately. To extract the kinetics of the bright contrast only, we subtract the dark contrast observed at 515 nm from the profiles observed at 705 nm. However, we must scale the dark contrast at 515 nm by a scaling factor η, since an excited carrier population can affect the transient complex refractive index differently at different wavelengths. This scaling parameter and the subtraction are discussed in detail in Section 4.6. The time decays in Figure 35 appear almost biexponential but can be more accurately described by 1/x fits (they appear rounded rather than sharply stepping from one lifetime to another). This is characteristic of EEA, discussed in Section 4.1. This corroborates the assumption that the bright contrast corresponds to excitons. Surprisingly, the dark contrast shows similar kinetics to the bright contrast. We explain this with a kinetic model, described in Section 4.7.

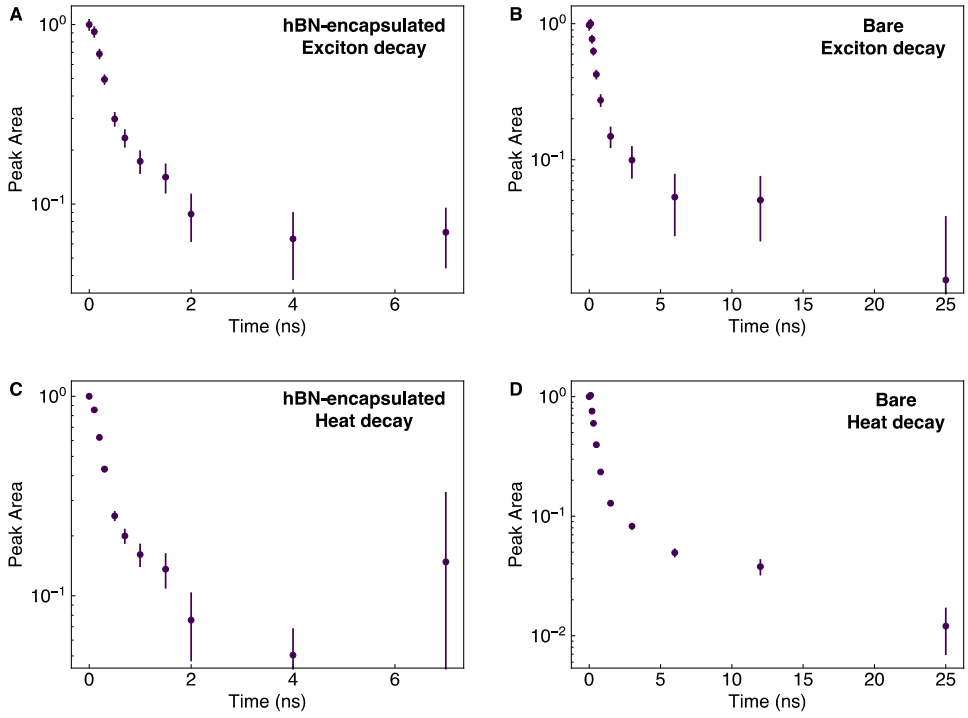

Figure 35. **StroboSCAT contrast time decays.** (**A, B**) Bright contrast decays for hBN-encapsulated (**A**) and bare (**B**) samples imaged with the 705 nm probe. These are calculated by subtracting the 515 nm probe data, multiplied by the scaling factor η, from the 705 nm probe data. (**C, D**) Dark contrast decays for hBN-encapsulated (**C**) and bare (**D**) samples imaged with the 515 nm probe.

4.6 Deconvoluting Heat and Excitons with Temperature-Dependent Reflection Contrast Measurements

To further corroborate our contrast assignment, we turn to spectroSCAT, which provides spectral as well as spatiotemporal information. SpectroSCAT allows the Ginsberg group to measure a transient reflection spectrum at the same delay times and excitation conditions as stroboSCAT. Rather than using a monochromatic probe beam, they use a white light probe, and they place a prism in front of the CCD to disperse the wavelengths of light. This results in the CCD image shown in Figure 36A. By binning over the pixels in the vertical dimension, they can calculate a spectroSCAT spectrum. It is also useful to examine the whole CCD image, as the vertical dimension provides spatial information. The center of the CCD (y = 70) images the center of our sample, and the edges of the CCD image the edges of our sample.

SpectroSCAT contrast is flipped relative to stroboSCAT contrast due to the extra focusing (Gouy) phase in stroboSCAT, which is tuned to $-\pi \leq \phi_{gouy} \leq -\pi/2$ to maximize contrast due to scattering. This makes the cosine term in the stroboSCAT signal negative relative to the spectroSCAT signal (see Section 4.2). Thus, yellow (positive) in the spectroSCAT image in Figure 36A corresponds to dark stroboSCAT contrast, and blue (negative) corresponds to bright stroboSCAT contrast. Close to 700 nm, a vertical slice of the CCD image appears similar to our stroboSCAT data probed at 705 nm, with positive spectroSCAT signal (dark stroboSCAT contrast) in the center, and negative spectroSCAT signal (bright stroboSCAT contrast) on the edges.

SpectroSCAT employs a focused white light probe, in contrast to the collimated probe beam in stroboSCAT, so the two configurations represent different probe beam angles of incidence on the sample. The fact that we see the same contrast behavior near 700 nm in spectroSCAT and stroboSCAT suggests that the bright ring around the dark center that we observe in stroboSCAT is not related to a thin-film optical effect, but rather represents two different populations being present in the sample.

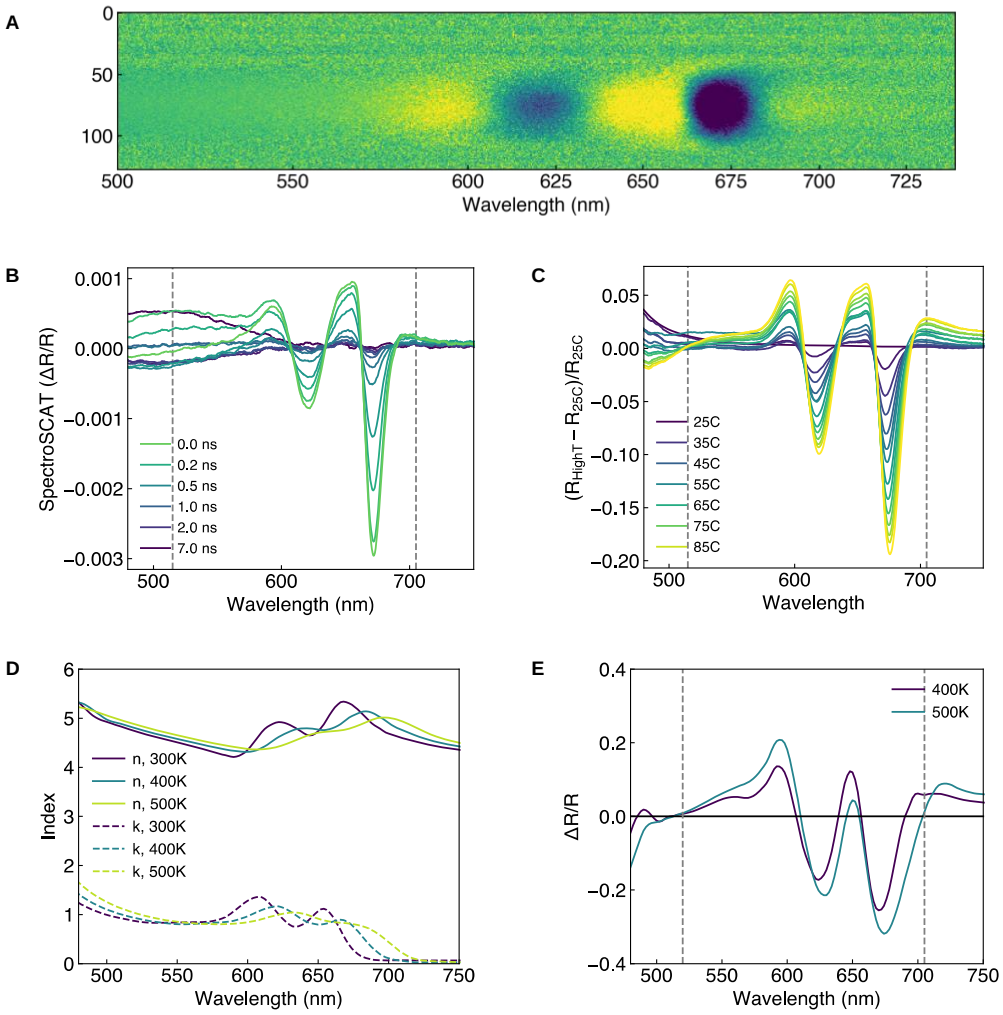

Figure 36. **Spectrally resolved measurements and deconvoluting heat from excitons.** (**A**) CCD image taken during spectroSCAT. The y axis represents position on the sample. (**B**) SpectroSCAT $\Delta R/R$ spectrum, calculated by vertically binning the CCD image in (**A**). (**C**) Temperature-dependent reflectance contrast spectrum, showing heat-only contribution to $\Delta R/R$. (**D**) Temperature-dependent complex refractive index, taken from (*126*). (**E**) $\Delta R/R$ as calculated from the temperature-dependent complex refractive index in (**D**).

The spectroSCAT spectrum, calculated by binning over the columns of pixels in the CCD image, is shown in Figure 36B. Again, we see that the spectroSCAT signal at 705 nm is positive, corresponding to a dominant dark center in stroboSCAT. Below about 560 nm, fluctuations in the power of the white light source cause the data to be unreliable. Further, comparison with the temperature-dependent data in Figure 36C revealed that the wavelength was not correctly calibrated for the CCD in spectroSCAT. To perform a rough calibration, we matched peak positions between Figure 36B and Figure 36C and applied a

linear correction to the raw spectroSCAT wavelength. To address these issues, future studies would employ a stabilized white light source and an independent wavelength calibration for the spectroSCAT CCD.

To isolate the effects of heat on the spectroSCAT signal, we perform temperature-dependent reflection contrast (RC) measurements, shown in Figure 36C. We use thermal grease to attach a resistive heating element and a thermocouple directly to the coverglass of the encapsulated MoS_2 sample shown in Figure 32. Using a white light source, we measure a reflection contrast spectrum by measuring reflection from the sample and the substrate, subtracting a background spectrum from each, then dividing the sample reflectance by the substrate reflectance. We vary the temperature from 25ºC to 85ºC in steps of 5ºC, allowing the sample to stabilize for 5 minutes between measurements. To compare temperature-dependent RC data to spectroSCAT data, we must calculate the quantity:

$$\frac{\Delta R}{R} = \frac{R_{PumpON} - R_{PumpOFF}}{R_{PumpOFF}} = \frac{R_{HighT} - R_{25C}}{R_{25C}}$$

However, the temperature-dependent RC measurements are different than the spectroSCAT measurements because 1) they measure reflection contrast relative to the substrate rather than absolute reflectance, and 2) spectroSCAT and stroboSCAT use an oil immersion objective with an oil that is index-matched to the coverglass, whereas temperature-dependent RC measurements use a dry objective. Imaging in air rather than through an index-matched oil adds an extra reflection off the front of the coverglass, which is conveniently approximately equal to half the substrate reflectance (half because the substrate reflectance includes reflections off the front and the back side of the coverglass). Upon subtracting half the substrate reflectance from each R in the above equation, then dividing both the top and the bottom by the substrate reflectance to convert to reflectance contrast, we arrive at:

$$\frac{\Delta R}{R} = \frac{RC_{HighT} - RC_{25C}}{RC_{25C} - 1/2}$$

This calculation represents the contribution of heat to the spectroSCAT contrast and is plotted in Figure 36C. Similar to spectroSCAT, these measurements are not reliable below 560 nm, since the lamp power was low in that spectral range and the exact value of the background counts had a large effect on the signal. In future temperature-dependent RC measurements, we suggest taking a background spectrum before each reflectance measurement rather than using a single background spectrum for the entire dataset.

Despite these experimental challenges, comparing the spectroSCAT data to the temperature-dependent RC data leads to a number of key insights. First, the temperature-dependent reflectance contrast looks remarkably similar to the spectroSCAT spectrum, suggesting that heat dominates the stroboSCAT contrast that we see at all wavelengths. Second, this experiment definitively confirms that the dark stroboSCAT contrast at 705 nm is heat. The temperature-dependent RC measurements show that heat results in positive spectroSCAT contrast, and therefore negative stroboSCAT contrast, at 705 nm. Since temperature-dependent RC is always positive at 705 nm, and $\Delta R/R$ monotonically decreases as temperature decreases, the bright contrast at 705 nm must be another population, making our assignment of bright contrast to excitons plausible.

In theory, it should be possible to extract an exciton-only $\Delta R/R$ spectrum by directly subtracting the temperature-dependent RC data from the spectroSCAT data. In practice, this is not possible given our current datasets, since we use the peaks from the temperature-dependent RC data to calibrate the wavelength for the spectroSCAT data. Therefore, if there are small peak shifts between the two spectra due to the presence of excitons, these will be hard to detect since our wavelength calibration assumes that the two spectra are the same. This subtraction also requires precise knowledge of the expected temperature change in the sample in spectroSCAT measurements, which is estimated to be about 10 K and will be discussed in Section 4.7. It should also be possible to extract an exciton-only spectrum by binning vertically over only the edges of the CCD image in Figure 36A, and this edge spectrum should be similar to the subtracted exciton-only $\Delta R/R$ spectrum. Correctly calibrating the spectroSCAT wavelength and performing the temperature-dependent RC subtraction to arrive at an exciton-only $\Delta R/R$ spectrum could be the subject of future work.

Because of the unreliable data at lower wavelengths in both spectroSCAT and temperature-dependent RC measurements, these measurements do not definitively show anything about the stroboSCAT data taken with the 515 nm probe. It is unclear whether the temperature-dependent RC data is even positive or negative at that wavelength, as 515 nm appears to be close to a point where the $\Delta R/R$ signal crosses zero. Across the entire spectrum, the points at which the zero-crossings occur redshift as temperature increases, so at the lower temperatures of ~10K that we expect, it is more likely that the 515 nm probe lies on the positive side of the zero-crossing. We continue to be relatively sure that the dark contrast at 515 nm is heat because of our prior reasoning (the radial extent of the dark at 515 nm matches the radial extent of the dark at 705 nm, and the dark contrast decays more quickly in the hBN-encapsulated samples at both probe wavelengths), as well as the new evidence that heat dominates the transient spectrum across all wavelengths.

To extract exciton-only stroboSCAT data, we can subtract the 515-nm probe data from the 705-nm probe data after multiplying by a scaling factor η. This scaling factor represents the ratio between the contribution of heat to $\Delta R/R$ at 705 nm, and the contribution of heat to $\Delta R/R$ at 515 nm. With more precise data at lower wavelengths, we could calculate η by directly dividing the temperature-dependent RC signal at 705 nm from the temperature-dependent RC signal at 515 nm. Since we do not have reliable data at 515 nm, we instead examine the data at 560 nm. We know that the temperature-dependent RC signal at 515 nm must be positive if heat is dark at that probe wavelength, and inspecting Figure 36C suggests that the signal at 515 nm is smaller than the signal at 560 nm. Therefore, the η that we calculate at 560 nm should place a lower bound on η at 515 nm. Performing this calculation sets the bound $\eta > 2$. Looking at the data, this makes sense: the temperature-dependent RC at 705 nm is much greater in magnitude than the temperature-dependent RC around 515 nm, even though the signal at both wavelengths is caused by the same amount of heat. So, to subtract the contribution of heat from the 705 nm data, we must multiply the 515 nm data by a number greater than 1.

One final caveat: it is possible that η is not constant, but rather is temperature-dependent. For example, if we imagine probing near a point where the RC signal crosses zero (e.g. at a probe wavelength of 625 nm), η relative to probing at 705 nm could actually start negative

at higher temperatures, asymptote to minus infinity as the signal approached zero, then return along an asymptote from infinity to a positive number at lower temperatures. We know that we are not encountering this exact situation since the 515 nm contrast does not flip signs, but η could still be temperature-dependent further away from a zero-crossing. Assuming that 515 nm lies just red of a zero-crossing where the RC signal goes from negative at shorter wavelengths to positive at longer wavelengths, it is most likely that η would be larger at higher temperatures and smaller at lower temperatures, which we will consider to explain discrepancies in our modeling.

The temperature-dependent RC measurements match well with the $\Delta R/R$ that would be predicted from the temperature-dependent complex refractive index for MoS_2 as measured by Liu et al. (*126*). Figure 36D shows the temperature-dependent complex refractive index extracted from their paper. This clearly shows the two expected effects of heat on complex refractive index: 1) the bandgap redshifts, and 2) the exciton resonances broaden. Figure 36E shows $\Delta R/R$ as calculated from that complex refractive index. Comparing this $\Delta R/R$ spectrum to the complex refractive index reveals the physical mechanism behind each peak. The sharp lowest-energy negative peak is due to the increase in *k* or absorption (and therefore decrease in reflection) below the A exciton resonance as the bandgap shifts down with temperature. The lowest-energy positive peak is most likely due to an increase in reflection below the A exciton resonance due to the slightly higher n at higher temperatures.

The physical mechanism behind the exciton contrast is harder to predict without an exciton-only transient reflectance spectrum. However, it is possible that the tradeoff between bandgap renormalization and binding energy reduction—that leads to a slight redshift in exciton peak position for a monolayer—instead leads to a blueshift for a multilayer. As heat causes a redshift, this would lead to excitons and heat having the opposite effect on the complex refractive index at most probe wavelengths. Even a redshift of a different magnitude for excitons compared to heat could cause a different transient reflectance spectrum. To collect an exciton-only $\Delta R/R$ spectrum to complement our heat-only $\Delta R/R$ spectrum, we suggest performing spectroSCAT at a pump power that is nearly resonant with the A exciton to minimize sample heating from charge carrier thermalization, and at

a low excitation density to minimize sample heating from EEA. Alternatively, we suggest electrically injecting excitons into the sample and measuring exciton density-dependent RC.

4.7 Modeling StroboSCAT Contrast with a Kinetic Model

As the final step in interpreting our stroboSCAT data, the Rabani group uses a kinetic model to predict the spatiotemporal evolution of both heat and excitons. The equation that describes the spatiotemporal evolution of excitons is:

$$\frac{dN(r,t)}{dt} = -R_A N^2 - \frac{1}{\tau_x} N + D_x \nabla^2 N + \sigma s \nabla^2 T$$

The first term refers to EEA, where R_A is the EEA coefficient in cm^2/s. The second term describes linear recombination of excitons, where τ_x is the exciton lifetime, including both radiative and nonradiative processes. The third term describes conventional diffusion, where D_x is the diffusivity. The fourth term describes the Seebeck effect, where excitons move in response to a temperature gradient, which can result in the exciton halos described in Section 4.1. Following (*127*), σs is the conductivity multiplied by the reduced Seebeck coefficient $s = S/q$.

The equation that describes the spatiotemporal evolution of heat is:

$$\frac{dT(r,t)}{dt} = \alpha N^2 + \beta N - \frac{1}{\tau_T}[T - T_0] + D_T \nabla^2 T$$

The first term represents the heat deposited in the lattice by EEA, where α is the temperature increase per EEA event and subsequent cooling of the hot exciton. We calculate this temperature increase from $\alpha = R_A E_g / c$, where E_g is the bandgap and c is the heat capacity from (*133*). The second term represents the heat deposited in the lattice by nonradiative recombination. We calculate β, the temperature increase per nonradiative recombination event, as $\beta = (1 - QY) E_g / \tau_x c$, where QY is the quantum yield (which we set to be 1%, here). The third term represents the decay of heat as it dissipates to the

surroundings, where τ_T is the heat lifetime. Finally, the fourth term represents the diffusion of heat, where D_T is the heat diffusivity.

We describe the initial carrier population with a time-dependent generation term that has the temporal width of the pump pulse and a Gaussian spatial distribution. We describe the initial temperature by taking into account the thermalization of carriers after excitation with a high-energy pump pulse.

With so many potential fitting parameters, it can be helpful to narrow down the parameter space before starting an optimization process. We therefore make the approximation that there is no spatial dependence and no diffusion, and we can then solve the two differential equations above analytically. The solutions are derived in Appendix C: Analytical StroboSCAT Solution.

After using experimental values to define realistic upper and lower bounds on each of the fitting parameters, and using the analytical solutions to develop a reasonable initial guess to feed into the optimizer, we use Matlab's Optimization Toolbox to fit our experimental stroboSCAT data. Table 3 shows the final fitting parameters.

Table 3. **StroboSCAT fitting parameters**.

Parameter	Value	Unit
μ_X	77	cm^2/Vs
R_A	4.5×10^{-5}	cm^2/s
τ_X	2.6	ns
τ_T	295	ps
η	4.5	

The fitting parameters Table 3 all fall within a reasonable range given experimental values. Mobilities in the range of 10s–100s of cm^2/Vs have been reported in TMDs (*92*, *117*). Similar to the case of encapsulated TMDs or TMDs placed on a high-index substrate discussed in Section 4.1, the EEA coefficient can be multiple orders of magnitude smaller in few-layer TMDs than in monolayer TMDs (*89*). Therefore, our estimate of 10^{-4}–10^{-5} cm^2/s is a reasonable range for the EEA coefficient in encapsulated few-layer MoS_2.

Previous studies have shown that R_A is still important in few-layer samples, which agrees with the 1/x-like decays that we observe in Figure 35 (*135*). Studies on other TMDs have reported that the exciton lifetime for multilayer TMDs is about 10 times longer than the monolayer lifetime, because the large oscillator strength for excitons in monolayers translates to a short radiative lifetime (*92*, *93*). Given that the exciton lifetime for monolayer MoS_2 is around 100 ps, a lifetime on the order of a few ns is reasonable for multilayer MoS_2 (*94, 108, 109*). Similar lifetimes have previously been observed in multilayer TMDs (*89*, *114*, *135, 136*). One possible hypothesis for these long lifetimes is that surface recombination limits the lifetimes in multilayer TMDs, and in thicker samples the surface is less accessible and therefore longer lifetimes are possible (*94*). The momentum-indirect nature of the lowest-energy exciton in multilayer TMDs may also increase the lifetime. The heat lifetime is similar to the previously reported 100 ps timescale for cooling of the lattice via interfacial transfer to the surroundings (*110*). The diffusivity in TMDs has been reported to be on the order of 1 cm^2/s at low excitation densities (*127*, *128*, *134*). A mobility of 77 $cm^2V^{-1}s^{-1}$ translates to a diffusivity of about 0.2 cm^2/s, in good agreement with diffusivities reported elsewhere. Finally, the thermal diffusivity is 0.15 K cm^{-2} s^{-1}, in agreement with the diffusivity calculated from thermal conductivities and heat capacities reported elsewhere (*131–133*).

We find that we can accurately fit the data with a Seebeck coefficient of zero, and we do not see halos in our modeled exciton population. This is not surprising, as R_A is about 2 orders of magnitude lower for multilayer samples than for monolayer samples, and the formation of halos is highly dependent on R_A. Previous work has shown that hBN-encapsulated samples have lower EEA coefficients and therefore exhibit no exciton halos, so we would not expect to see halos in our hBN-encapsulated, multilayer samples (*112*).

We find that the equations above cannot perfectly fit the 515-nm probe data for the hBN-encapsulated sample, as there appears to be a longer-lived component to the kinetics (Figure 35). We therefore add a phenomenological $t^{-1/2}$ term to represent heat diffusion in the hBN being laterally limited at later times, after the interfacial transfer takes place.

The model matches the data very well, as shown in Figure 37. We note that the y-axis scale varies over several orders of magnitude, and the fits are within error (for the heat data) or close to within error (for the exciton data). This corroborates our assignment of excitons to bright contrast at 705 nm, and heat to dark contrast at both 520 nm and 705 nm.

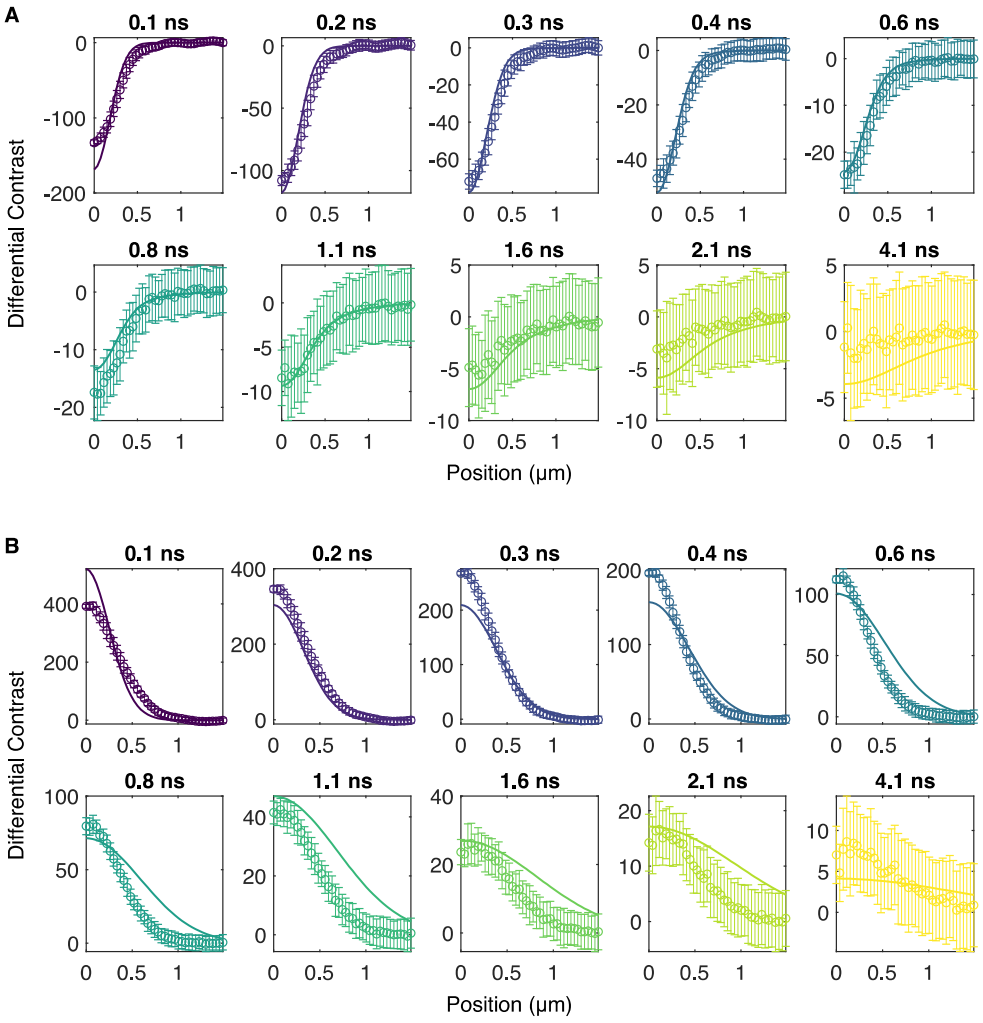

Figure 37. **Modeling StroboSCAT data with a kinetic model.** Differential contrast (y axis) is multiplied by 10^5 relative to Figure 34. Heat-only and exciton-only populations are calculated by applying η to the experimental data, where η = 4.5 yielded the best fits. (**A**) Results of the fits to the heat-only data, measured with the 515 nm probe. (**B**) Results of the fits to the exciton-only data, calculated by subtracting η times the 515-nm (heat-only) data from the 705-nm data.

We see some disagreement between the model and the data for the exciton profiles, though we anticipate that this could be addressed with further optimization of the fitting (e.g.

accounting for the initial exciton population being generated by a pump that is not perfectly diffraction-limited). The possibility of a temperature-dependent η could also explain discrepancies between the data and the fits. With the η derived from the fitting, we can now fully decouple the spatiotemporal evolution of excitons from heat, and we use this to calculate the kinetics of the two separate populations shown in Figure 35.

Following our modeling, we note two interesting findings that may be helpful to TMD researchers. First, EEA can have a dominant effect on kinetics even when R_A is quite small, as it is in multilayer, hBN-encapsulated samples. Second, heat can have a dominant effect on transient spectra even when the absolute temperature is small. Our model predicts a maximum temperature change of less than 10K, and yet temperature clearly dominates the spectroSCAT data (Figure 36).

4.8 Conclusion

In summary, we use stroboSCAT and spectroSCAT to track the spatiotemporal and spectral evolution of heat and excitons in few-layer MoS_2. We observe both bright and dark contrast when probing at 705 nm, and only dark contrast when probing at 515 nm. We assign dark contrast to heat at both probe wavelengths, since the dark contrast decays faster in hBN-encapsulated samples, and we assign bright contrast at 705 nm to excitons since it diffuses faster than dark contrast. We use temperature-dependent RC measurements to corroborate our contrast assignment and to show that heat dominates the spectroSCAT signal at all wavelengths. Finally, we develop a kinetic model that matches the data well and allows us to completely decouple the contributions of excitons and heat to the stroboSCAT signal.

We find that heat must be carefully considered when looking at transient optical spectra, as heat dominates our signal even though the change in lattice temperature is only around 10 K. Although stroboSCAT probes later times relative to other pump-probe techniques, heat may have a large influence even at early times and even with a near-resonant pump due to fast EEA. Many studies assume that transient optical spectra are exciton-dominated, leading to possible misinterpretations of transient spectra that actually may be dominated by heat (*137*, *138*).

We also find that EEA can dominate kinetics in TMDs, even in hBN-encapsulated multilayer samples that have a relatively small EEA coefficient. It is important to point out that the 1/x-like decay characteristic of EEA can look a lot like a biexponential, and we caution researchers against fitting TRPL decays in TMDs without considering EEA. Further, we note that stroboSCAT could be a promising technique for measuring lifetimes in semiconductors with low radiative efficiency, including the multilayer TMDs.

The stroboSCAT technique is relatively new, and this work contributes significant advances towards fully understanding the technique. These advances will not only help in future stroboSCAT studies of TMDs, but also in stroboSCAT studies of other materials.

First, we outline a process for performing stroboSCAT measurements to maximize data accuracy and ease of interpretation, as follows. 1) A spectroSCAT spectrum should be collected to determine the ideal probe wavelengths, which should be far away from any zero-crossings of the $\Delta R/R$ spectrum. 2) A wavelength calibration should be performed directly following the spectroSCAT measurement. 3) A stroboSCAT measurement should be taken at the specified probe wavelength. 4) The point-spread-function of the probe laser should be measured directly following the stroboSCAT measurement, as well as the size of the pump imaged at the differential focal plane. 5) If heat is expected to play a dominant role, temperature-dependent RC measurements can be taken to examine the role of heat only. A background spectrum should be collected before each spectrum. 6) If charge carriers are expected to play a dominant role, spectroSCAT measurements can be taken with a low-fluence, resonant pump. Alternatively, carriers can be electrically injected and a carrier-dependent RC measurement can be collected.

Second, we outline a microscopic interpretation for stroboSCAT and a corresponding process for modeling and interpreting stroboSCAT data, as follows. 1) An excited population of energy carriers (heat, excitons, electrons, holes) changes the local complex refractive index in the material. This can be measured with spectroSCAT or transient absorption/reflection, and the effects of different types of carriers can be decoupled as discussed above. 2) The probe beam scatters off this locally changed refractive index, which acts as a Mie scatterer. This can be modeled with an optical solver like Lumerical

FDTD, but cannot be modeled with a method like the transfer matrix method that only calculates reflection. 3) The excited carriers decay in time and diffuse in space, causing the stroboSCAT signal to spread and decay. This can be modeled with a kinetic model, and the spatial and temporal separation between different contrast signs can aid in the assignment of contrast to carrier type.

In the process of this project, we have discovered a number of upgrades that make the stroboSCAT technique even more powerful. A stabilized white light source could help with collecting reliable spectroSCAT data at lower wavelengths. Using ultrafast lasers could improve the time resolution of the system. Integrating a heating stage as well as a Keithley source-measure unit would allow for temperature-dependent and carrier density-dependent RC measurements to be taken directly in the stroboSCAT setup. The Ginsberg group is currently working to implement many of these upgrades.

Armed with a complete understanding of in-plane transport and kinetics in relatively simple TMD architectures, we are now prepared to employ stroboSCAT to explore other interesting unanswered questions about TMDs. When we initially started this project, we aimed to gain an understanding of out-of-plane transport and exciton dissociation in TMDs (*60*, *136*). We wanted to know whether excitons dissociated at interfaces or in the bulk of TMD photovoltaics, and how out-of-plane transport occurred through the van der Waals gap. With a thorough understanding of the excited carrier types and contrast in few-layer MoS_2, we can now turn to using stroboSCAT to answer these novel questions.

Chapter 5: Conclusions and Outlook

5.1 Summary

In this thesis, we demonstrate that two-dimensional (2D) transition metal dichalcogenides (TMDs) are promising candidates for ultrathin photovoltaics. We start with the simplest solar cell architecture, a Schottky-junction solar cell, consisting of a WS_2 absorber layer sandwiched between Au and Ag contacts. We demonstrate a power conversion efficiency of 0.5% in this device, and develop a new metal transfer process with broad applications to nanomaterials-based devices. We then move on to the solar cell architecture with the highest efficiency potential, a carrier-selective contact solar cell, consisting of a WS_2 absorber layer sandwiched between a PTAA hole-selective contact and a C60 electron-selective contact. We demonstrate a power conversion efficiency of 2.4% in this device, suggesting that low-cost perovskite carrier selective contacts are transferrable to TMDs. With straightforward improvements to optical design and WSe_2 active layers, we calculate that a similar solar cell could achieve a power conversion efficiency of 7%.

We show that the short lifetime in TMDs limits the carrier density that can be sustained under illumination, and therefore limits the open-circuit voltage in intrinsic multilayer TMD solar cells to 750 mV. We measure the lifetime in multilayer TMDs both with photoconductivity measurements and with stroboSCAT, a new pump-probe optical microscopy technique. We also use stroboSCAT to explore other fundamental properties of TMDs, such as the effect of exciton-exciton annihilation on excited carrier kinetics and the effect of heat on optical spectra.

Throughout this thesis, we highlight several areas for improvement in TMD solar cells. Increasing the radiative efficiency could boost the voltage, though more characterization of the radiative lifetime in multilayer TMDs is needed. Doping the TMDs could increase the open-circuit voltage beyond the current limit for intrinsic TMDs of 750 mV, and exploring a more complete library of carrier-selective contacts for TMDs could enable open-circuit voltages close to the theoretical limits. Switching from multilayer to monolayer TMDs could also be a promising subject for future TMD photovoltaics research,

as monolayers are direct bandgap semiconductors and can achieve unity radiative efficiency upon passivation. Finally, for scalable TMD solar cells, devices will need to fabricated with large-area synthesis techniques, such as chemical vapor deposition or chemical exfoliation, rather than mechanical exfoliation. We expand upon these four future research areas below.

5.2 Defining Practical Limits on Power Conversion Efficiencies

It is possible to calculate a practical efficiency limit based on detailed balance considerations for each TMD and as a function of thickness. The important experimental inputs necessary to calculate this limit are: 1) the absorption of the TMD, especially the sub-bandgap absorption (*139*); 2) the lifetime, as described above; and 3) the photoluminescence quantum yield or external radiative efficiency (*140*). Absorption can be measured with a combination of direct measurement of above-gap absorption and indirect measurement of below-gap absorption via fitting the photoluminescence spectrum. Lifetimes can be measured using time-resolved photoluminescence, for high radiative efficiency TMDs like monolayers, or using a technique such as stroboSCAT that can probe dark carriers. In a symmetric device geometry, lifetimes can be measured with photoconductivity measurements. Photoluminescence quantum yield can be measured in a microscope using a Lambertian scatterer as a reference, as described previously (*19*).

For monolayer TMDs, the photoluminescence quantum yield can be enhanced via the superacid treatment, and the radiative lifetimes are well characterized. For multilayer TMDs, the radiative lifetimes can be approximately extracted from the nonradiative lifetimes and the photoluminescence quantum yield. The observed lifetimes will set a practical limit, and the radiative lifetimes will set an upper limit, on the open-circuit voltage in TMD solar cells, as described above.

This experimental study could be complemented with theory. Two areas of future theoretical research could be using theory to corroborate the calculated radiative lifetimes in indirect-bandgap multilayer samples, and exploring the physical mechanism for the superacid treatment.

5.3 Optimizing Device Architectures via Doping and Selective Contact Exploration

More work is required to optimize TMD solar cell device architectures. The entire library of carrier-selective contacts for perovskite solar cells could be explored for TMDs, and band alignments could be measured using techniques such as ultraviolet photoelectron spectroscopy and x-ray photoelectron spectroscopy. A similar technique to (*83*) could be used to screen potential selective contact materials, where the photoluminescence intensity is measured before and after application of the selective contact. More detailed modeling could also be performed in Sentaurus TCAD, including further exploration of the S-shaped I-V curves caused by asymmetric contact transport and examination of the effect of low out-of-plane mobility on TMD solar cells.

As discussed in Chapter 3, doped TMDs can exceed the voltage limit imposed by the carrier lifetime. Thus, doping for TMDs could be explored in more detail. This could include existing techniques, such as MoO_3 doping (*38*), as well as more novel techniques, such as proximity doping (*141*).

5.4 Moving to Monolayers

Monolayer TMD solar cells have been explored less than multilayer TMD solar cells, although they could have a number of advantages. Monolayer TMDs are direct bandgap semiconductors, eliminating the loss that comes from low absorption near the indirect edge in multilayer TMDs. They also can achieve near-unity radiative efficiency, eliminating the loss from nonradiative recombination. However, even the *radiative* lifetimes of monolayer TMDs are quite short due to strong electron-hole coupling, and this may put a stringent limit on the voltage achievable in undoped monolayer TMDs regardless of their radiative efficiency. Further, a monolayer usually only absorbs 5–10% of the incident light, so device architectures must be carefully designed for high absorption. This may be possible with planar optical cavities (*142*) or with nanostructured dielectric resonators (*143*). Monolayer TMDs also impose limitations on the type of carrier collection that can be used, as tunneling can occur through a monolayer if states are available for tunneling on either side. In theory, vertical carrier-selective contact devices should avoid this issue.

5.5 Large-Area Solar Cells

All of the solar cells described in this thesis are microscopically small. Practical applications for TMD photovoltaics will require large-area solar cells, and we suggest this as a final area of future research. One possible synthesis method is chemical exfoliation of TMDs, where a TMD crystal is broken into small nanosheets by e.g. sonication or intercalation, and these nanosheets are coated onto a substrate to form a macroscopic TMD layer (*95–97*). Another possible synthesis method that would work for monolayers as well as multilayers is chemical vapor deposition and transfer (*98–100*).

5.6 Outlook

Achieving large-area TMD solar cells with power conversion efficiencies greater than 10% is within reach. This will require a combination of deepened understanding of the fundamental physics at play (i.e. lifetimes and how to approach the radiative limit), engineering of device architectures (i.e. doping and careful screening of selective contacts), and chemistry and materials growth to achieve large-area samples (i.e. using chemical vapor deposition or chemical exfoliation). It remains to be seen whether ultrathin TMD solar cells will have real-world applications, but for the promise is certainly there, particularly for high-specific power photovoltaics.

Bibliography

1. Halas Group, Unit Conversions, (available at https://halas.rice.edu/unit-conversions).

2. Wikipedia, Mathematical descriptions of opacity, (available at https://en.wikipedia.org/wiki/Mathematical_descriptions_of_opacity).

3. S. J. Byrnes, Multilayer optical calculations. (2016) (available at https://arxiv.org/abs/1603.02720v5).

4. GATS, Spectral Calculator, (available at https://www.spectralcalc.com/info/about).

5. Wikipedia, Idealized greenhouse model, (available at https://en.wikipedia.org/wiki/Idealized_greenhouse_model).

6. IPCC, "Summary for Policymakers. In: Global Warming of 1.5°C." (2018).

7. Our World in Data, CO2 Emissions, (available at https://ourworldindata.org/co2-emissions).

8. US EPA, Sources of Greenhouse Gas Emissions, (available at https://www.epa.gov/ghgemissions/sources-greenhouse-gas-emissions).

9. Carbon Visuals, New York's Carbon Emissions - In Real Time (2014), (available at http://www.carbonvisuals.com/projects/new-yorks-carbon-emissions-in-real-time).

10. IEA, Cement – Analysis (2021), (available at https://www.iea.org/reports/cement).

11. IEA, Iron and Steel – Analysis (2021), (available at https://www.iea.org/reports/iron-and-steel).

12. S. Griffith, *Electrify* (MIT Press, 2021).

13. N. Climate.gov, Climate Change: Atmospheric Carbon Dioxide (2021), (available at https://www.climate.gov/news-features/understanding-climate/climate-change-atmospheric-carbon-dioxide).

14. J. D. Jenkins, E. N. Mayfield, R. Jones, J. Farbes, N. Patankar, Q. Xu, A. Jacobson, Summary Report: The Climate Impact of Congressional Infrastructure and Budget Bills. *REPEAT Proj.* (2022), doi:10.5281/zenodo.6311986.

15. D. M. Powell, R. Fu, K. Horowitz, P. A. Basore, M. Woodhouse, T. Buonassisi, The capital intensity of photovoltaics manufacturing: barrier to scale and opportunity for innovation. *Energy Environ. Sci.* **8**, 3395–3408 (2015).

16. M. Bernardi, M. Palummo, J. C. Grossman, Extraordinary Sunlight Absorption and

One Nanometer Thick Photovoltaics Using Two-Dimensional Monolayer Materials. *Nano Lett.* **13**, 3664–3670 (2013).

17. K. F. Mak, C. Lee, J. Hone, J. Shan, T. F. Heinz, Atomically Thin MoS_2: A New Direct-Gap Semiconductor. *Phys. Rev. Lett.* **105**, 136805 (2010).

18. A. Splendiani, L. Sun, Y. Zhang, T. Li, J. Kim, C.-Y. Chim, G. Galli, F. Wang, Emerging Photoluminescence in Monolayer MoS_2. *Nano Lett.* **10**, 1271–1275 (2010).

19. M. Amani, D.-H. Lien, D. Kiriya, J. Xiao, A. Azcatl, J. Noh, S. R. Madhvapathy, R. Addou, S. KC, M. Dubey, K. Cho, R. M. Wallace, S.-C. Lee, J.-H. He, J. W. Ager, X. Zhang, E. Yablonovitch, A. Javey, Near-unity photoluminescence quantum yield in MoS_2. *Science* **350**, 1065–1068 (2015).

20. W. Shockley, H. J. Queisser, Detailed balance limit of efficiency of p-n junction solar cells. *J. Appl. Phys.* **32**, 510–519 (1961).

21. D. Jariwala, A. R. Davoyan, G. Tagliabue, M. C. Sherrott, J. Wong, H. A. Atwater, Near-Unity Absorption in van der Waals Semiconductors for Ultrathin Optoelectronics. *Nano Lett.* **16**, 5482–5487 (2016).

22. L. Huang, G. Li, A. Gurarslan, Y. Yu, R. Kirste, W. Guo, J. Zhao, R. Collazo, Z. Sitar, G. N. Parsons, M. Kudenov, L. Cao, Atomically Thin MoS_2 Narrowband and Broadband Light Superabsorbers. *ACS Nano* **10**, 7493–7499 (2016).

23. D. Jariwala, A. R. Davoyan, J. Wong, H. A. Atwater, Van der Waals Materials for Atomically-Thin Photovoltaics: Promise and Outlook. *ACS Photonics* **4**, 2962–2970 (2017).

24. A. Pospischil, M. M. Furchi, T. Mueller, Solar-energy conversion and light emission in an atomic monolayer p–n diode. *Nat. Nanotechnol.* **9**, 257–261 (2014).

25. B. W. H. Baugher, H. O. H. Churchill, Y. Yang, P. Jarillo-Herrero, Optoelectronic devices based on electrically tunable p–n diodes in a monolayer dichalcogenide. *Nat. Nanotechnol.* **9**, 262–267 (2014).

26. J. S. Ross, P. Klement, A. M. Jones, N. J. Ghimire, J. Yan, D. G. Mandrus, T. Taniguchi, K. Watanabe, K. Kitamura, W. Yao, D. H. Cobden, X. Xu, Electrically tunable excitonic light-emitting diodes based on monolayer WSe_2 p–n junctions. *Nat. Nanotechnol.* **9**, 268–272 (2014).

27. C.-H. Lee, G.-H. Lee, A. M. van der Zande, W. Chen, Y. Li, M. Han, X. Cui, G. Arefe, C. Nuckolls, T. F. Heinz, J. Guo, J. Hone, P. Kim, Atomically thin p–n junctions with van der Waals heterointerfaces. *Nat. Nanotechnol.* **9**, 676–681 (2014).

28. M. M. Furchi, A. Pospischil, F. Libisch, J. Burgdörfer, T. Mueller, Photovoltaic

Effect in an Electrically Tunable van der Waals Heterojunction. *Nano Lett.* **14**, 4785–4791 (2014).

29. R. Cheng, D. Li, H. Zhou, C. Wang, A. Yin, S. Jiang, Y. Liu, Y. Chen, Y. Huang, X. Duan, Electroluminescence and Photocurrent Generation from Atomically Sharp WSe_2/MoS_2 Heterojunction p–n Diodes. *Nano Lett.* **14**, 5590–5597 (2014).

30. M.-L. Tsai, M.-Y. Li, J. R. D. Retamal, K.-T. Lam, Y.-C. Lin, K. Suenaga, L.-J. Chen, G. Liang, L.-J. Li, J.-H. He, Single Atomically Sharp Lateral Monolayer p-n Heterojunction Solar Cells with Extraordinarily High Power Conversion Efficiency. *Adv. Mater.* **29**, 1701168 (2017).

31. Y. Jin, D. H. Keum, S.-J. An, J. Kim, H. S. Lee, Y. H. Lee, A Van Der Waals Homojunction: Ideal p-n Diode Behavior in $MoSe_2$. *Adv. Mater.* **27**, 5534–5540 (2015).

32. Y. Liu, J. Guo, E. Zhu, L. Liao, S.-J. Lee, M. Ding, I. Shakir, V. Gambin, Y. Huang, X. Duan, Approaching the Schottky–Mott limit in van der Waals metal–semiconductor junctions. *Nature* **557**, 696–700 (2018).

33. M. Fontana, T. Deppe, A. K. Boyd, M. Rinzan, A. Y. Liu, M. Paranjape, P. Barbara, Electron-hole transport and photovoltaic effect in gated MoS_2 schottky junctions. *Sci. Rep.* **3**, 1634 (2013).

34. J. Wong, D. Jariwala, G. Tagliabue, K. Tat, A. R. Davoyan, M. C. Sherrott, H. A. Atwater, High Photovoltaic Quantum Efficiency in Ultrathin van der Waals Heterostructures. *ACS Nano* **11**, 7230–7240 (2017).

35. H.-M. Li, D. Lee, D. Qu, X. Liu, J. Ryu, A. Seabaugh, W. J. Yoo, Ultimate thin vertical p–n junction composed of two-dimensional layered molybdenum disulfide. *Nat. Commun.* **6**, 6564 (2015).

36. S. Wi, H. Kim, M. Chen, H. Nam, L. J. Guo, E. Meyhofer, X. Liang, Enhancement of Photovoltaic Response in Multilayer MoS_2 Induced by Plasma Doping. *ACS Nano* **8**, 5270–5281 (2014).

37. T. Akama, W. Okita, R. Nagai, C. Li, T. Kaneko, T. Kato, Schottky solar cell using few-layered transition metal dichalcogenides toward large-scale fabrication of semitransparent and flexible power generator. *Sci. Rep.* **7**, 11967 (2017).

38. K. Nassiri Nazif, A. Kumar, J. Hong, N. Lee, R. Islam, C. J. McClellan, O. Karni, J. van de Groep, T. F. Heinz, E. Pop, M. L. Brongersma, K. C. Saraswat, High-Performance p–n Junction Transition Metal Dichalcogenide Photovoltaic Cells Enabled by MoO_x Doping and Passivation. *Nano Lett.* **21**, 3443–3450 (2021).

39. K. Nassiri Nazif, A. Daus, J. Hong, N. Lee, S. Vaziri, A. Kumar, F. Nitta, M. E. Chen, S. Kananian, R. Islam, K.-H. Kim, J.-H. Park, A. S. Y. Poon, M. L.

Brongersma, E. Pop, K. C. Saraswat, High-specific-power flexible transition metal dichalcogenide solar cells. *Nat. Commun.* **12**, 7034 (2021).

40. P. Würfel, U. Wurfel, *Physics of Solar Cells* (Wiley, Weinheim, Germany, ed. 3, 2016).

41. M. O. Reese, S. Glynn, M. D. Kempe, D. L. McGott, M. S. Dabney, T. M. Barnes, S. Booth, D. Feldman, N. M. Haegel, Increasing markets and decreasing package weight for high-specific-power photovoltaics. *Nat. Energy* **3**, 1002–1012 (2018).

42. Z. Yang, L. Liao, F. Gong, F. Wang, Z. Wang, X. Liu, X. Xiao, W. Hu, J. He, X. Duan, WSe_2/GeSe heterojunction photodiode with giant gate tunability. *Nano Energy* **49**, 103–108 (2018).

43. L. Wang, I. Meric, P. Y. Huang, Q. Gao, Y. Gao, H. Tran, T. Taniguchi, K. Watanabe, L. M. Campos, D. A. Muller, J. Guo, P. Kim, J. Hone, K. L. Shepard, C. R. Dean, One-Dimensional Electrical Contact to a Two-Dimensional Material. *Science* **342**, 614–617 (2013).

44. E. J. Telford, A. Benyamini, D. Rhodes, D. Wang, Y. Jung, A. Zangiabadi, K. Watanabe, T. Taniguchi, S. Jia, K. Barmak, A. N. Pasupathy, C. R. Dean, J. Hone, Via Method for Lithography Free Contact and Preservation of 2D Materials. *Nano Lett.* **18**, 1416–1420 (2018).

45. Y. Wang, J. C. Kim, R. J. Wu, J. Martinez, X. Song, J. Yang, F. Zhao, A. Mkhoyan, H. Y. Jeong, M. Chhowalla, Van der Waals contacts between three-dimensional metals and two-dimensional semiconductors. *Nature* **568**, 70–74 (2019).

46. Y. Liu, P. Stradins, S.-H. Wei, Van der Waals metal-semiconductor junction: Weak Fermi level pinning enables effective tuning of Schottky barrier. *Sci. Adv.* **2**, e1600069 (2016).

47. M. M. Furchi, F. Höller, L. Dobusch, D. K. Polyushkin, S. Schuler, T. Mueller, Device physics of van der Waals heterojunction solar cells. *npj 2D Mater. Appl.* **2**, 3 (2018).

48. K. M. McPeak, S. V. Jayanti, S. J. P. Kress, S. Meyer, S. Iotti, A. Rossinelli, D. J. Norris, Plasmonic Films Can Easily Be Better: Rules and Recipes. *ACS Photonics* **2**, 326–333 (2015).

49. M. A. Kats, R. Blanchard, P. Genevet, F. Capasso, Nanometre optical coatings based on strong interference effects in highly absorbing media. *Nat. Mater.* **12**, 20–24 (2013).

50. X. Feng, M. A. Meitl, A. M. Bowen, Y. Huang, R. G. Nuzzo, J. A. Rogers, Competing Fracture in Kinetically Controlled Transfer Printing. *Langmuir* **23**, 12555–12560 (2007).

51. F. Pizzocchero, L. Gammelgaard, B. S. Jessen, J. M. Caridad, L. Wang, J. Hone, P. Bøggild, T. J. Booth, The hot pick-up technique for batch assembly of van der Waals heterostructures. *Nat. Commun.* **7**, 11894 (2016).

52. U. Wurfel, A. Cuevas, P. Wurfel, Charge Carrier Separation in Solar Cells. *IEEE J. Photovoltaics* **5**, 461–469 (2015).

53. C. Waldauf, M. C. Scharber, P. Schilinsky, J. A. Hauch, C. J. Brabec, Physics of organic bulk heterojunction devices for photovoltaic applications. *J. Appl. Phys.* **99**, 104503 (2006).

54. H. J. Snaith, The perils of solar cell efficiency measurements. *Nat. Photonics* **6**, 337–340 (2012).

55. H. J. Snaith, How should you measure your excitonic solar cells? *Energy Environ. Sci.* **5**, 6513 (2012).

56. S. B. Desai, S. R. Madhvapathy, M. Amani, D. Kiriya, M. Hettick, M. Tosun, Y. Zhou, M. Dubey, J. W. Ager, D. Chrzan, A. Javey, Gold-Mediated Exfoliation of Ultralarge Optoelectronically-Perfect Monolayers. *Adv. Mater.* **28**, 4053–4058 (2016).

57. K. K. Kam, B. A. Parkinson, Detailed photocurrent spectroscopy of the semiconducting group VIB transition metal dichalcogenides. *J. Phys. Chem.* **86**, 463–467 (1982).

58. K. Keyshar, M. Berg, X. Zhang, R. Vajtai, G. Gupta, C. K. Chan, T. E. Beechem, P. M. Ajayan, A. D. Mohite, T. Ohta, Experimental Determination of the Ionization Energies of $MoSe_2$, WS_2, and MoS_2 on SiO_2 Using Photoemission Electron Microscopy. *ACS Nano* **11**, 8223–8230 (2017).

59. D. Wickramaratne, F. Zahid, R. K. Lake, Electronic and thermoelectric properties of few-layer transition metal dichalcogenides. *J. Chem. Phys.* **140**, 124710 (2014).

60. M. Massicotte, P. Schmidt, F. Vialla, K. G. Schädler, A. Reserbat-Plantey, K. Watanabe, T. Taniguchi, K. J. Tielrooij, F. H. L. Koppens, Picosecond photoresponse in van der Waals heterostructures. *Nat. Nanotechnol.* **11**, 42–46 (2016).

61. D. Li, R. Cheng, H. Zhou, C. Wang, A. Yin, Y. Chen, N. O. Weiss, Y. Huang, X. Duan, Electric-field-induced strong enhancement of electroluminescence in multilayer molybdenum disulfide. *Nat. Commun.* **6**, 7509 (2015).

62. G. Cao, A. Shang, C. Zhang, Y. Gong, S. Li, Q. Bao, X. Li, Optoelectronic investigation of monolayer MoS_2/WSe_2 vertical heterojunction photoconversion devices. *Nano Energy* **30**, 260–266 (2016).

63. A. Laturia, M. L. Van de Put, W. G. Vandenberghe, Dielectric properties of

hexagonal boron nitride and transition metal dichalcogenides: from monolayer to bulk. *npj 2D Mater. Appl.* **2**, 6 (2018).

64. Y. Li, A. Chernikov, X. Zhang, A. Rigosi, H. M. Hill, A. M. van der Zande, D. A. Chenet, E.-M. Shih, J. Hone, T. F. Heinz, Measurement of the optical dielectric function of monolayer transition-metal dichalcogenides: MoS_2, $MoSe_2$, WS_2, and WSe_2. *Phys. Rev. B* **90**, 205422 (2014).

65. W. Zhao, Z. Ghorannevis, L. Chu, M. Toh, C. Kloc, P.-H. Tan, G. Eda, Evolution of Electronic Structure in Atomically Thin Sheets of WS_2 and WSe_2. *ACS Nano* **7**, 791–797 (2013).

66. H. Zeng, G.-B. Liu, J. Dai, Y. Yan, B. Zhu, R. He, L. Xie, S. Xu, X. Chen, W. Yao, X. Cui, Optical signature of symmetry variations and spin-valley coupling in atomically thin tungsten dichalcogenides. *Sci. Rep.* **3**, 1608 (2013).

67. M. Amani, P. Taheri, R. Addou, G. H. Ahn, D. Kiriya, D.-H. Lien, J. W. Ager, R. M. Wallace, A. Javey, Recombination Kinetics and Effects of Superacid Treatment in Sulfur- and Selenium-Based Transition Metal Dichalcogenides. *Nano Lett.* **16**, 2786–2791 (2016).

68. X. Zhang, T. H. Choudhury, M. Chubarov, Y. Xiang, B. Jariwala, F. Zhang, N. Alem, G.-C. Wang, J. A. Robinson, J. M. Redwing, Diffusion-Controlled Epitaxy of Large Area Coalesced WSe_2 Monolayers on Sapphire. *Nano Lett.* **18**, 1049–1056 (2018).

69. X. Zhang, F. Zhang, Y. Wang, D. S. Schulman, T. Zhang, A. Bansal, N. Alem, S. Das, V. H. Crespi, M. Terrones, J. M. Redwing, Defect-Controlled Nucleation and Orientation of WSe_2 on hBN: A Route to Single-Crystal Epitaxial Monolayers. *ACS Nano* **13**, 3341–3352 (2019).

70. K. Kang, S. Xie, L. Huang, Y. Han, P. Y. Huang, K. F. Mak, C.-J. Kim, D. Muller, J. Park, High-mobility three-atom-thick semiconducting films with wafer-scale homogeneity. *Nature* **520**, 656–660 (2015).

71. K. Kang, K.-H. Lee, Y. Han, H. Gao, S. Xie, D. A. Muller, J. Park, Layer-by-layer assembly of two-dimensional materials into wafer-scale heterostructures. *Nature* **550**, 229–233 (2017).

72. L. Wang, L. Huang, W. C. Tan, X. Feng, L. Chen, X. Huang, K.-W. Ang, 2D Photovoltaic Devices: Progress and Prospects. *Small Methods* **2**, 1700294 (2018).

73. E. McVay, A. Zubair, Y. Lin, A. Nourbakhsh, T. Palacios, Impact of Al_2O_3 Passivation on the Photovoltaic Performance of Vertical WSe_2 Schottky Junction Solar Cells. *ACS Appl. Mater. Interfaces* **12**, 57987–57995 (2020).

74. K. Nassiri Nazif, A. Kumar, M. T. Moreira de Menezes, K. Saraswat, Towards high

V_{oc}, thin film, homojunction WS_2 solar cells for energy harvesting applications., 7 (2019).

75. X. Mao, J. Zou, H. Li, Z. Song, S. He, Magnetron sputtering fabrication and photoelectric properties of WSe_2 film solar cell device. *Appl. Surf. Sci.* **444**, 126–132 (2018).

76. C. M. Went, J. Wong, P. R. Jahelka, M. Kelzenberg, S. Biswas, M. S. Hunt, A. Carbone, H. A. Atwater, A new metal transfer process for van der Waals contacts to vertical Schottky-junction transition metal dichalcogenide photovoltaics. *Sci. Adv.* **5**, eaax6061 (2019).

77. S. A. Svatek, C. Bueno-Blanco, D. Y. Lin, J. Kerfoot, C. Macías, M. H. Zehender, I. Tobías, P. García-Linares, T. Taniguchi, K. Watanabe, P. Beton, E. Antolín, High open-circuit voltage in transition metal dichalcogenide solar cells. *Nano Energy* **79**, 105427 (2021).

78. M. Shanmugam, C. A. Durcan, B. Yu, Layered semiconductor molybdenum disulfide nanomembrane based Schottky-barrier solar cells. *Nanoscale* **4**, 7399 (2012).

79. Q. Fu, X. Tang, B. Huang, T. Hu, L. Tan, L. Chen, Y. Chen, Recent Progress on the Long-Term Stability of Perovskite Solar Cells. *Adv. Sci.* **5**, 1700387 (2018).

80. X. Zheng *et al.*, Managing grains and interfaces via ligand anchoring enables 22.3%-efficiency inverted perovskite solar cells. *Nat. Energy* **5**, 131–140 (2020).

81. E. Gutierrez-Partida, H. Hempel, S. Caicedo-Dávila, M. Raoufi, F. Peña-Camargo, M. Grischek, R. Gunder, J. Diekmann, P. Caprioglio, K. O. Brinkmann, H. Köbler, S. Albrecht, T. Riedl, A. Abate, D. Abou-Ras, T. Unold, D. Neher, M. Stolterfoht, Large-Grain Double Cation Perovskites with 18 μs Lifetime and High Luminescence Yield for Efficient Inverted Perovskite Solar Cells. *ACS Energy Lett.* **6**, 1045–1054 (2021).

82. F. Li, X. Deng, F. Qi, Z. Li, D. Liu, D. Shen, M. Qin, S. Wu, F. Lin, S.-H. Jang, J. Zhang, X. Lu, D. Lei, C.-S. Lee, Z. Zhu, A. K.-Y. Jen, Regulating Surface Termination for Efficient Inverted Perovskite Solar Cells with Greater Than 23% Efficiency. *J. Am. Chem. Soc.* **142**, 20134–20142 (2020).

83. M. Stolterfoht, P. Caprioglio, C. M. Wolff, J. A. Márquez, J. Nordmann, S. Zhang, D. Rothhardt, U. Hörmann, Y. Amir, A. Redinger, L. Kegelmann, F. Zu, S. Albrecht, N. Koch, T. Kirchartz, M. Saliba, T. Unold, D. Neher, The impact of energy alignment and interfacial recombination on the internal and external open-circuit voltage of perovskite solar cells. *Energy Environ. Sci.* **12**, 2778–2788 (2019).

84. T. G. Allen, J. Bullock, X. Yang, A. Javey, S. De Wolf, Passivating contacts for crystalline silicon solar cells. *Nat. Energy* **4**, 914–928 (2019).

85. B. Dänekamp, N. Droseros, D. Tsokkou, V. Brehm, P. P. Boix, M. Sessolo, N. Banerji, H. J. Bolink, Influence of hole transport material ionization energy on the performance of perovskite solar cells. *J. Mater. Chem. C* **7**, 523–527 (2019).

86. Y. Hirose, Structural and electronic properties of an organic/inorganic semiconductor interface: PTCDA/GaAs(100). *J. Vac. Sci. Technol. B Microelectron. Nanom. Struct.* **12**, 2616 (1994).

87. P. R. Jahelka, R. D. Glaudell, H. A. Atwater, US20210391486A1 - Systems and Methods for Non-Epitaxial High Schottky-Barrier Heterojunction Solar Cells (2021), (available at https://patents.google.com/patent/US20210391486A1/en).

88. D.-H. Lien, S. Z. Uddin, M. Yeh, M. Amani, H. Kim, J. W. Ager, E. Yablonovitch, A. Javey, Electrical suppression of all nonradiative recombination pathways in monolayer semiconductors. *Science* **364**, 468–471 (2019).

89. L. Yuan, L. Huang, Exciton dynamics and annihilation in WS_2 2D semiconductors. *Nanoscale* **7**, 7402–7408 (2015).

90. W. Tress, K. Leo, M. Riede, Influence of Hole-Transport Layers and Donor Materials on Open-Circuit Voltage and Shape of I-V Curves of Organic Solar Cells. *Adv. Funct. Mater.* **21**, 2140–2149 (2011).

91. W. Tress, A. Petrich, M. Hummert, M. Hein, K. Leo, M. Riede, Imbalanced mobilities causing S-shaped IV curves in planar heterojunction organic solar cells. *Appl. Phys. Lett.* **98**, 063301 (2011).

92. Q. Cui, F. Ceballos, N. Kumar, H. Zhao, Transient Absorption Microscopy of Monolayer and Bulk WSe_2. *ACS Nano* **8**, 2970–2976 (2014).

93. H. Wang, C. Zhang, W. Chan, C. Manolatou, S. Tiwari, F. Rana, Radiative lifetimes of excitons and trions in monolayers of the metal dichalcogenide MoS_2. *Phys. Rev. B* **93**, 045407 (2016).

94. H. Wang, C. Zhang, F. Rana, Surface Recombination Limited Lifetimes of Photoexcited Carriers in Few-Layer Transition Metal Dichalcogenide MoS_2. *Nano Lett.* **15**, 8204–8210 (2015).

95. C. Backes, T. M. Higgins, A. Kelly, C. Boland, A. Harvey, D. Hanlon, J. N. Coleman, Guidelines for Exfoliation, Characterization and Processing of Layered Materials Produced by Liquid Exfoliation. *Chem. Mater.* **29**, 243–255 (2017).

96. C.-X. Hu, Y. Shin, O. Read, C. Casiraghi, Dispersant-assisted liquid-phase exfoliation of 2D materials beyond graphene. *Nanoscale* **13**, 460–484 (2021).

97. F. Liu, Mechanical exfoliation of large area 2D materials from vdW crystals. *Prog. Surf. Sci.* **96**, 100626 (2021).

98. M. Wu, Y. Xiao, Y. Zeng, Y. Zhou, X. Zeng, L. Zhang, W. Liao, Synthesis of two-dimensional transition metal dichalcogenides for electronics and optoelectronics. *InfoMat* **3**, 362–396 (2021).

99. M. Wang, H. Li, T.-J. Ko, M. Sumaiya Shawkat, E. Okogbue, C. Yoo, S. S. Han, M. A. Islam, K. H. Oh, Y. Jung, Manufacturing strategies for wafer-scale two-dimensional transition metal dichalcogenide heterolayers. *J. Mater. Res.* **35**, 1350–1368 (2020).

100. J. R. Brent, N. Savjani, P. O'Brien, Synthetic approaches to two-dimensional transition metal dichalcogenide nanosheets. *Prog. Mater. Sci.* **89**, 411–478 (2017).

101. K. M. Islam, R. Synowicki, T. Ismael, I. Oguntoye, N. Grinalds, M. D. Escarra, In-Plane and Out-of-Plane Optical Properties of Monolayer, Few-Layer, and Thin-Film MoS_2 from 190 to 1700 nm and Their Application in Photonic Device Design. *Adv. Photonics Res.* **2**, 2000180 (2021).

102. W. van Roosbroeck, W. Shockley, Photon-Radiative Recombination of Electrons and Holes in Germanium. *Phys. Rev.* **94**, 1558–1560 (1954).

103. E. C. Regan, D. Wang, C. Jin, M. I. Bakti Utama, B. Gao, X. Wei, S. Zhao, W. Zhao, Z. Zhang, K. Yumigeta, M. Blei, J. D. Carlström, K. Watanabe, T. Taniguchi, S. Tongay, M. Crommie, A. Zettl, F. Wang, Mott and generalized Wigner crystal states in WSe_2/WS_2 moiré superlattices. *Nature* **579**, 359–363 (2020).

104. Y. Shimazaki, I. Schwartz, K. Watanabe, T. Taniguchi, M. Kroner, A. Imamoğlu, Strongly correlated electrons and hybrid excitons in a moiré heterostructure. *Nature* **580**, 472–477 (2020).

105. Y. Tang, L. Li, T. Li, Y. Xu, S. Liu, K. Barmak, K. Watanabe, T. Taniguchi, A. H. MacDonald, J. Shan, K. F. Mak, Simulation of Hubbard model physics in WSe_2/WS_2 moiré superlattices. *Nature* **579**, 353–358 (2020).

106. L. Wang, E.-M. Shih, A. Ghiotto, L. Xian, D. A. Rhodes, C. Tan, M. Claassen, D. M. Kennes, Y. Bai, B. Kim, K. Watanabe, T. Taniguchi, X. Zhu, J. Hone, A. Rubio, A. N. Pasupathy, C. R. Dean, Correlated electronic phases in twisted bilayer transition metal dichalcogenides. *Nat. Mater.* **19**, 861–866 (2020).

107. G. Wang, A. Chernikov, M. M. Glazov, T. F. Heinz, X. Marie, T. Amand, B. Urbaszek, Colloquium : Excitons in atomically thin transition metal dichalcogenides. *Rev. Mod. Phys.* **90**, 021001 (2018).

108. D. Sun, Y. Rao, G. A. Reider, G. Chen, Y. You, L. Brézin, A. R. Harutyunyan, T. F. Heinz, Observation of Rapid Exciton–Exciton Annihilation in Monolayer Molybdenum Disulfide. *Nano Lett.* **14**, 5625–5629 (2014).

109. H. Wang, C. Zhang, F. Rana, Ultrafast Dynamics of Defect-Assisted Electron–Hole

Recombination in Monolayer MoS_2. *Nano Lett.* **15**, 339–345 (2015).

110. C. Ruppert, A. Chernikov, H. M. Hill, A. F. Rigosi, T. F. Heinz, The Role of Electronic and Phononic Excitation in the Optical Response of Monolayer WS_2 after Ultrafast Excitation. *Nano Lett.* **17**, 644–651 (2017).

111. A. J. Goodman, D.-H. Lien, G. H. Ahn, L. L. Spiegel, M. Amani, A. P. Willard, A. Javey, W. A. Tisdale, Substrate-Dependent Exciton Diffusion and Annihilation in Chemically Treated MoS_2 and WS_2. *J. Phys. Chem. C* **124**, 12175–12184 (2020).

112. J. Zipfel, M. Kulig, R. Perea-Causín, S. Brem, J. D. Ziegler, R. Rosati, T. Taniguchi, K. Watanabe, M. M. Glazov, E. Malic, A. Chernikov, Exciton diffusion in monolayer semiconductors with suppressed disorder. *Phys. Rev. B* **101**, 115430 (2020).

113. H. Shi, R. Yan, S. Bertolazzi, J. Brivio, B. Gao, A. Kis, D. Jena, H. G. Xing, L. Huang, Exciton Dynamics in Suspended Monolayer and Few-Layer MoS_2 2D Crystals. *ACS Nano* **7**, 1072–1080 (2013).

114. T. Wang, Y. Zhang, Y. Liu, J. Li, D. Liu, J. Luo, K. Ge, Layer-Number-Dependent Exciton Recombination Behaviors of MoS_2 Determined by Fluorescence-Lifetime Imaging Microscopy. *J. Phys. Chem. C* **122**, 18651–18658 (2018).

115. N. S. Ginsberg, W. A. Tisdale, Spatially Resolved Photogenerated Exciton and Charge Transport in Emerging Semiconductors. *Annu. Rev. Phys. Chem.* **71**, 1–30 (2020).

116. Z. Nie, R. Long, L. Sun, C.-C. Huang, J. Zhang, Q. Xiong, D. W. Hewak, Z. Shen, O. V Prezhdo, Z.-H. Loh, Ultrafast Carrier Thermalization and Cooling Dynamics in Few-Layer MoS_2. *ACS Nano* **8**, 10931–10940 (2014).

117. J. H. Strait, P. Nene, F. Rana, High intrinsic mobility and ultrafast carrier dynamics in multilayer metal-dichalcogenide MoS_2. *Phys. Rev. B* **90**, 245402 (2014).

118. S. Sim, J. Park, J.-G. Song, C. In, Y.-S. Lee, H. Kim, H. Choi, Exciton dynamics in atomically thin MoS_2: Interexcitonic interaction and broadening kinetics. *Phys. Rev. B* **88**, 075434 (2013).

119. R. Perea-Causín, S. Brem, E. Malic, Microscopic Modeling of Pump–Probe Spectroscopy and Population Inversion in Transition Metal Dichalcogenides. *Phys. status solidi* **257**, 2000223 (2020).

120. R. Schmidt, G. Berghäuser, R. Schneider, M. Selig, P. Tonndorf, E. Malić, A. Knorr, S. Michaelis de Vasconcellos, R. Bratschitsch, Ultrafast Coulomb-Induced Intervalley Coupling in Atomically Thin WS_2. *Nano Lett.* **16**, 2945–2950 (2016).

121. A. Chernikov, C. Ruppert, H. M. Hill, A. F. Rigosi, T. F. Heinz, Population inversion and giant bandgap renormalization in atomically thin WS_2 layers. *Nat.*

Photonics **9**, 466–470 (2015).

122. A. Steinhoff, M. Rösner, F. Jahnke, T. O. Wehling, C. Gies, Influence of Excited Carriers on the Optical and Electronic Properties of MoS_2. *Nano Lett.* **14**, 3743–3748 (2014).

123. E. A. A. Pogna, M. Marsili, D. De Fazio, S. Dal Conte, C. Manzoni, D. Sangalli, D. Yoon, A. Lombardo, A. C. Ferrari, A. Marini, G. Cerullo, D. Prezzi, Photo-Induced Bandgap Renormalization Governs the Ultrafast Response of Single-Layer MoS_2. *ACS Nano* **10**, 1182–1188 (2016).

124. P. D. Cunningham, A. T. Hanbicki, K. M. McCreary, B. T. Jonker, Photoinduced Bandgap Renormalization and Exciton Binding Energy Reduction in WS_2. *ACS Nano* **11**, 12601–12608 (2017).

125. E. J. Sie, A. Steinhoff, C. Gies, C. H. Lui, Q. Ma, M. Rösner, G. Schönhoff, F. Jahnke, T. O. Wehling, Y.-H. Lee, J. Kong, P. Jarillo-Herrero, N. Gedik, Observation of Exciton Redshift–Blueshift Crossover in Monolayer WS_2. *Nano Lett.* **17**, 4210–4216 (2017).

126. H.-L. Liu, T. Yang, J.-H. Chen, H.-W. Chen, H. Guo, R. Saito, M.-Y. Li, L.-J. Li, Temperature-dependent optical constants of monolayer MoS_2, $MoSe_2$, WS_2, and WSe_2: spectroscopic ellipsometry and first-principles calculations. *Sci. Rep.* **10**, 15282 (2020).

127. R. Perea-Causín, S. Brem, R. Rosati, R. Jago, M. Kulig, J. D. Ziegler, J. Zipfel, A. Chernikov, E. Malic, Exciton Propagation and Halo Formation in Two-Dimensional Materials. *Nano Lett.* **19**, 7317–7323 (2019).

128. M. Kulig, J. Zipfel, P. Nagler, S. Blanter, C. Schüller, T. Korn, N. Paradiso, M. M. Glazov, A. Chernikov, Exciton Diffusion and Halo Effects in Monolayer Semiconductors. *Phys. Rev. Lett.* **120**, 207401 (2018).

129. M. Delor, H. L. Weaver, Q. Yu, N. S. Ginsberg, Imaging material functionality through three-dimensional nanoscale tracking of energy flow. *Nat. Mater.* **19**, 56–62 (2020).

130. D. G. Purdie, N. M. Pugno, T. Taniguchi, K. Watanabe, A. C. Ferrari, A. Lombardo, Cleaning interfaces in layered materials heterostructures. *Nat. Commun.* **9**, 5387 (2018).

131. A. Arrighi, E. del Corro, D. N. Urrios, M. V. Costache, J. F. Sierra, K. Watanabe, T. Taniguchi, J. A. Garrido, S. O. Valenzuela, C. M. Sotomayor Torres, M. Sledzinska, Heat dissipation in few-layer MoS_2 and MoS_2/hBN heterostructure. *2D Mater.* **9**, 015005 (2022).

132. S. Sahoo, A. P. S. Gaur, M. Ahmadi, M. J.-F. Guinel, R. S. Katiyar, Temperature-

Dependent Raman Studies and Thermal Conductivity of Few-Layer MoS_2. *J. Phys. Chem. C* **117**, 9042–9047 (2013).

133. D. F. Smith, D. Brown, A. S. Dworkin, D. J. Sasmor, E. R. Van Artsdalen, Low Temperature Heat Capacity and Entropy of Molybdenum Trioxide and Molybdenum Disulfide. *J. Am. Chem. Soc.* **78**, 1533–1536 (1956).

134. S. Z. Uddin, H. Kim, M. Lorenzon, M. Yeh, D.-H. Lien, E. S. Barnard, H. Htoon, A. Weber-Bargioni, A. Javey, Neutral Exciton Diffusion in Monolayer MoS_2. *ACS Nano* **14**, 13433–13440 (2020).

135. K. T. Vogt, S. F. Shi, F. Wang, M. W. Graham, Ultrafast Photocurrent and Absorption Microscopy of Few-Layer Transition Metal Dichalcogenide Devices That Isolate Rate-Limiting Dynamics Driving Fast and Efficient Photoresponse. *J. Phys. Chem. C* **124**, 15195–15204 (2020).

136. M. Massicotte, F. Vialla, P. Schmidt, M. B. Lundeberg, S. Latini, S. Haastrup, M. Danovich, D. Davydovskaya, K. Watanabe, T. Taniguchi, V. I. Fal'ko, K. S. Thygesen, T. G. Pedersen, F. H. L. Koppens, Dissociation of two-dimensional excitons in monolayer WSe_2. *Nat. Commun.* **9**, 1633 (2018).

137. T. Borzda, C. Gadermaier, N. Vujicic, P. Topolovsek, M. Borovsak, T. Mertelj, D. Viola, C. Manzoni, E. A. A. Pogna, D. Brida, M. R. Antognazza, F. Scotognella, G. Lanzani, G. Cerullo, D. Mihailovic, Charge Photogeneration in Few-Layer MoS_2. *Adv. Funct. Mater.* **25**, 3351–3358 (2015).

138. S. K. Bera, D. Mandal, K. V Adarsh, in *AIP Conference Proceedings* (2021; https://doi.org/10.1063/5.0060839), vol. 2369, p. 020111.

139. J. Wong, S. T. Omelchenko, H. A. Atwater, Impact of Semiconductor Band Tails and Band Filling on Photovoltaic Efficiency Limits. *ACS Energy Lett.* **6**, 52–57 (2021).

140. U. Rau, U. W. Paetzold, T. Kirchartz, Thermodynamics of light management in photovoltaic devices. *Phys. Rev. B* **90**, 035211 (2014).

141. W. Zagozdzon-Wosik, P. B. Grabiec, G. Lux, Silicon doping from phosphorus spin-on dopant sources in proximity rapid thermal diffusion. *J. Appl. Phys.* **75**, 337–344 (1994).

142. J. Wong, thesis, California Institute of Technology (2022).

143. R. A. Pala, S. Butun, K. Aydin, H. A. Atwater, Omnidirectional and broadband absorption enhancement from trapezoidal Mie resonators in semiconductor metasurfaces. *Sci. Rep.* **6**, 31451 (2016).

144. J. Rogelj, G. Luderer, R. C. Pietzcker, E. Kriegler, M. Schaeffer, V. Krey, K. Riahi, Energy system transformations for limiting end-of-century warming to below 1.5°C.

Nat. Clim. Change **5**, 519–527 (2015).

145. J. Rogelj *et al.*, Scenarios towards limiting global mean temperature increase below 1.5°C. *Nat. Clim. Change* **8**, 325–332 (2018).

146. E. Larson, C. Greig, J. Jenkins, E. Mayfield, A. Pascale, C. Zhang, J. Drossman, R. Williams, S. Pacala, R. Socolow, E. Baik, R. Birdsey, R. Duke, R. Jones, B. Haley, E. Leslie, K. Paustian, A. Swan, Net-Zero America: Potential Pathways, Infrastructure, and Impacts Report. *Princeton University* (2021).

147. D. W. Keith, Why Capture CO_2 from the Atmosphere? *Science* **325**, 1654–1655 (2009).

148. S. J. Davis *et al.*, Net-zero emissions energy systems. *Science* **360**, eaas9793 (2018).

149. K. Anderson, G. Peters, The trouble with negative emissions. *Science* **354**, 182–183 (2016).

150. P. Williamson, Emissions reduction: Scrutinize CO_2 removal methods. *Nature* **530**, 153–155 (2016).

151. J. Fuhrman, H. McJeon, P. Patel, S. C. Doney, W. M. Shobe, A. F. Clarens, Food–energy–water implications of negative emissions technologies in a +1.5°C future. *Nat. Clim. Change* **10**, 920–927 (2020).

152. D. McLaren, N. Markusson, The co-evolution of technological promises, modelling, policies and climate change targets. *Nat. Clim. Change* **10**, 392–397 (2020).

153. C. Holz, L. S. Siegel, E. Johnston, A. P. Jones, J. Sterman, Ratcheting ambition to limit warming to 1.5°C–trade-offs between emission reductions and carbon dioxide removal. *Environ. Res. Lett.* **13**, 064028 (2018).

154. J. Strefler, N. Bauer, E. Kriegler, A. Popp, A. Giannousakis, O. Edenhofer, Between Scylla and Charybdis: Delayed mitigation narrows the passage between large-scale CDR and high costs. *Environ. Res. Lett.* **13**, 044015 (2018).

155. A. Kätelhön, R. Meys, S. Deutz, S. Suh, A. Bardow, Climate change mitigation potential of carbon capture and utilization in the chemical industry. *Proc. Natl. Acad. Sci. U. S. A.* **166**, 11187–11194 (2019).

156. R. Hanna, A. Abdulla, Y. Xu, D. G. Victor, Emergency deployment of direct air capture as a response to the climate crisis. *Nat. Commun.* **12**, 368 (2021).

157. G. Realmonte, L. Drouet, A. Gambhir, J. Glynn, A. Hawkes, A. C. Köberle, M. Tavoni, An inter-model assessment of the role of direct air capture in deep mitigation pathways. *Nat. Commun.* **10**, 3277 (2019).

158. D. W. Keith, G. Holmes, D. St. Angelo, K. Heidel, A Process for Capturing CO_2

from the Atmosphere. *Joule* **2**, 1573–1594 (2018).

159. R. Socolow, M. Desmond, R. Aines, J. Blackstock, O. Bolland, T. Kaarsberg, N. Lewis, M. Mazzotti, A. Pfeffer, K. Sawyer, J. Siirola, B. Smit, J. Wilcox, Direct Air Capture of CO_2 with Chemicals: A Technology Assessment for the APS Panel on Public Affairs. (2011) (available at http://www.aps.org/policy/reports/popa-reports/loader.cfm?csModule=security/getfile&PageID=244407).

160. S. Fuss, C. D. Jones, F. Kraxner, G. P. Peters, P. Smith, M. Tavoni, D. P. van Vuuren, J. G. Canadell, R. B. Jackson, J. Milne, J. R. Moreira, N. Nakicenovic, A. Sharifi, Y. Yamagata, Research priorities for negative emissions. *Environ. Res. Lett.* **11**, 115007 (2016).

161. P. Smith *et al.*, Biophysical and economic limits to negative CO_2 emissions. *Nat. Clim. Change* **6**, 42–50 (2016).

162. M. D. Eisaman, K. Parajuly, A. Tuganov, C. Eldershaw, N. Chang, K. A. Littau, CO_2 extraction from seawater using bipolar membrane electrodialysis. *Energy Environ. Sci.* **5**, 7346–7352 (2012).

163. C.-F. de Lannoy, M. D. Eisaman, A. Jose, S. D. Karnitz, R. W. DeVaul, K. Hannun, J. L. B. Rivest, Indirect ocean capture of atmospheric CO_2: Part I. Prototype of a negative emissions technology. *Int. J. Greenh. Gas Control* **70**, 243–253 (2018).

164. M. D. Eisaman, J. L. B. Rivest, S. D. Karnitz, C.-F. de Lannoy, A. Jose, R. W. DeVaul, K. Hannun, Indirect ocean capture of atmospheric CO_2: Part II. Understanding the cost of negative emissions. *Int. J. Greenh. Gas Control* **70**, 254–261 (2018).

165. I. A. Digdaya, I. Sullivan, M. Lin, L. Han, W. H. Cheng, H. A. Atwater, C. Xiang, A direct coupled electrochemical system for capture and conversion of CO_2 from oceanwater. *Nat. Commun.* **11**, 1–10 (2020).

166. R. Sharifian, R. M. Wagterveld, I. A. Digdaya, C. Xiang, D. A. Vermaas, Electrochemical carbon dioxide capture to close the carbon cycle. *Energy Environ. Sci.* **14**, 781–814 (2021).

167. National Academies of Sciences Engineering and Medicine, A Research Strategy for Ocean-based Carbon Dioxide Removal and Sequestration. *Natl. Acad. Press* (2021), doi:10.17226/26278.

168. D. C. Jones, T. Ito, Y. Takano, W.-C. Hsu, Spatial and seasonal variability of the air-sea equilibration timescale of carbon dioxide. *Global Biogeochem. Cycles* **28**, 1163–1178 (2014).

169. K. Caldeira, M. Akai, P. Brewer, B. Chen, P. Haugan, T. Iwama, P. Johnston, H. Kheshgi, Q. Li, T. Ohsumi, H. Pörtner, C. Sabine, Y. Shirayama, J. Thomson, Ocean

Storage In: IPCC Special Report on Carbon dioxide Capture and Storage. (2005).

170. R. E. Zeebe, D. A. Wolf-Gladrow, *CO_2 in seawater: Equilibrium, Kinerics, Isotopes* (Elsevier Science B.V., 2001).

171. Reuters Staff, Inside the world's biggest water desalination plants. *Reuters* (2020), (available at https://www.reuters.com/article/us-saudi-water-desalination/inside-the-worlds-biggest-water-desalination-plants-idUSKBN26Y1HD).

172. N. Voutchknov, *Desalination Engineering: Planning and Design* (The McGraw-Hill Companies, 2013).

173. W. D. Seider, J. D. Seader, D. R. Lewin, S. Widagdo, *Product and Process Design Principles* (John Wiley & Sons, Inc., 2009).

174. J. (NETL) Black, Capital Cost Scaling Methodology. (2013).

175. Department of Energy, Carbon Negative Shot (2021), (available at https://www.energy.gov/fecm/carbon-negative-shot).

176. J. Fordney, LADWP Signs Historic Solar/Storage Purchase Contract (2019), (available at https://www.newsdata.com/california_energy_markets/regional_roundup/ladwp-signs-historic-solar-storage-purchase-contract/article_e98114ca-d63a-11e9-961f-df1879f50836.html).

177. NREL, Electricity ATB Technologies and Data Overview (2021), (available at https://atb.nrel.gov/electricity/2021/index).

178. 8minute, Energy Storage - Innovative, flexible & affordable solutions (2021), (available at https://www.8minute.com/energy-storage/).

Appendix A: Technoeconomic Analysis of a Direct Ocean Carbon Capture System Coupled with a Chemical Kinetics Model of Steady-State Rates of CO_2 Extraction

Limiting climate change to 1.5 ºC will require the use of negative emissions technologies along with aggressive mitigation strategies. Direct oceanwater capture is a promising new carbon capture strategy that leverages the large liquid/gas exchange system at the oceanwater/air interface. Here, we develop a technoeconomic analysis of an offshore, stand-alone direct oceanwater capture system where relatively pure CO_2 gas is extracted from oceanwater using an electrochemical pH swing method based on bipolar membrane electrodialysis. We couple this technoeconomic analysis with a chemical kinetics model of reactions among dissolved inorganic carbon species to calculate steady-state rates of CO_2 extraction under realistic operating conditions. We determine the lowest-cost operating point, corresponding to an influent pH of 4 and a CO_2 partial pressure of 6.7 Torr in the membrane contactor, and calculate a CO_2 cost of $175/ton at the megaton/year scale. We determine that key drivers for low-cost CO_2 are low electrodialyzer operating voltage (<2.5 V per cell), high membrane contactor vacuum pressure (>1 Torr), and low pH influent to the membrane contactor (~4). This work demonstrates pathways to cost-effective CO_2 capture at the gigaton scale.

A.1 Introduction

To avert the worst effects of the climate crisis, particularly in the Global South and in island nations, it is imperative that governments and societies limit warming to 1.5ºC (*6*, *144*). Most modeled emission pathways consistent with this target incorporate negative emissions technologies (NETs) to varying degrees (*6*, *144–146*). These models agree that we will need CO_2 removal on the scale of gigatons per year by mid-century (*6*, *144–146*). In the short-term, NETs can offset emissions from hard-to-decarbonize sectors, and in the long-term, NETs can eventually reverse human impact on the global carbon cycle (*144*, *147*, *148*).

It is important to note that the 1.5ºC emission pathways that incorporate NETs also prescribe a steep decline in fossil fuel use, and that NETs are yet unproven at the scale suggested by these pathways (*6*, *144–146*, *149–151*). For these reasons, the potential future availability of NETs should not be interpreted as a license to continue burning fossil fuels. Carbon capture is currently in danger of being used as a "technology of prevarication," allowing government leaders to delay current action by pointing to the technological promise of NETs (*149*, *151*, *152*). As scientists working on carbon capture, it is therefore our responsibility to call for an accelerated phase-out of fossil fuels, which will significantly increase the chance of keeping the 1.5ºC target in reach regardless of the future availability of NETs (*153*, *154*). Further, many NETs are energy-intensive and their net carbon removal is only sensible when powered by renewable technologies—yet the climate change mitigation potential of other uses of renewable energy, such as displacement of fossil fuel-based energy and the electrification of buildings and transit, is currently much greater (*155*).

Despite these caveats, it is critical to continue researching NETs as we simultaneously adopt aggressive mitigation strategies. Investing in NETs now will kickstart the scale-up process necessary for these technologies to reach the scale and affordability projected by models that achieve a 1.5ºC target (*156*, *157*).

The most common NETs include bioenergy with carbon capture and sequestration (BECCS), afforestation and reforestation (AR), and direct air capture (DAC) (*147*, *150*, *158–160*). Gigaton-scale deployment of any of these common technologies has been predicted to have unintended consequences (*150*, *151*, *161*). Water use and primary energy requirements increase substantially when BECCS, AR, and DAC are deployed at scale—DAC could require as much as a quarter of current global energy use (*151*, *161*). Food costs increase by a factor of seven with large-scale deployment of BECCS and AR without DAC, and by a factor of three with large-scale deployment of BECCS and AR with DAC, due to competition for land use (*151*).

The land use demands of existing NETs make Direct Ocean Capture (DOC) of carbon a particularly promising new technology (*162–167*). The world's oceans are the largest

global carbon sink, storing 50 times more carbon than our atmosphere (*168*). Oceans have absorbed about 40% of all anthropogenic carbon emissions to date, due to equilibration between CO_2 in the atmosphere and the carbonate system in oceanwater that takes place on a short time scale (<1 year) (*168*, *169*). Total carbon in oceanwater exists as dissolved inorganic carbon (DIC), which mostly takes the form of bicarbonate (HCO_3^-) at the native ocean pH of ~8.1 (*170*). Acidifying oceanwater to pH ~4–5 shifts the DIC equilibrium toward dissolved CO_2(aq), which can then be extracted as gaseous CO_2 (*170*). By volume, DIC in oceanwater is ~120 times more concentrated than CO_2 in the atmosphere (*169*, *170*). In addition, DOC may have unique access to off-shore sequestration sites. These factors combined may it possible to capture CO_2 from the ocean on a larger scale and/or for less cost than from the air.

Previous technoeconomic analysis of CO_2 cost from a DOC system that used an electrochemical pH swing method indicated a CO_2 cost ranging from $436/ton for co-location with a desalination plant to $1839/ton for a stand-alone plant (*164*). Co-location with desalination plants limits the ultimate scale of CO_2 capture, as the oceanwater flow rate of the largest current desalination plant would only correspond to capture of about 40 kilotons of CO_2 per year (*171*). Even if the entire global freshwater demand were met by desalination, the DOC capacity for colocation with desalination would only be about a third of a gigaton of CO_2 per year. For a stand-alone, onshore DOC system, CO_2 costs are dominated by intake and outfall costs, which can be significantly reduced by using a stand-alone, offshore DOC system with a shallow intake (*164*).

Here, we present a technoeconomic analysis (TEA) of a stand-alone, offshore oceanwater CO_2 capture system. This system employs bipolar membrane electrodialysis (BPMED) to generate acid that is used to acidify the oceanwater and shift the carbonate balance toward dissolved CO_2. This dissolved CO_2 is then extracted as gaseous CO_2 in a gas–liquid membrane contactor (*165*). The decarbonized oceanwater is neutralized with the alkaline stream from the electrodialyzer, and this combined effluent is discharged back to the ocean. Depending on the effluent discharge location, the time scale for the mixing between the atmospheric CO_2 and the discharged oceanwater from the DOC system can be as short as 2–4 months, resulting a net CO_2 drawdown from atmosphere (*168*).

We couple the TEA with a chemical kinetics model of a membrane contactor to examine performance under realistic steady-state operating conditions and identify lowest-cost operating points. When the influent pH to the membrane contactor is 4, we find that the lowest-cost operating point occurs at a CO_2 partial pressure of 6.7 Torr and an extraction efficiency of 86%. We explore the sensitivity of CO_2 cost to several input parameters, such as electrodialyzer current density, electrodialyzer voltage, pH of acidified oceanwater flowing into the membrane contactor, and membrane contactor vacuum pressure. We project a levelized CO_2 cost of $861/metric ton at the 10-kton/year scale, and a levelized CO_2 cost of $175/metric ton at the megaton/year scale.

A.2 Acidifying Oceanwater Yields Higher Extraction Efficiency

The concentration of DIC in oceanwater is ~2 mM, and its equilibrium speciation can be determined based on pH. At high pH, carbonate is the dominant species, at intermediate pH, bicarbonate is the dominant species, and at low pH, dissolved CO_2 is the dominant species. Acidifying oceanwater from its native pH value of ~8.1 to a value closer to 4 therefore shifts the DIC balance away from bicarbonate and toward dissolved CO_2 (Figure 38A).

Charge balance dictates the amount of H^+ that must be added to native oceanwater to decrease its pH to values more acidic than 8.1:

$$[\mathrm{H^+}]_{\mathrm{added}} = \Delta[\mathrm{H^+}] - (\Delta[\mathrm{HCO_3^-}] + 2\Delta[\mathrm{CO_3^{2-}}] + \Delta[\mathrm{OH^-}])$$

where Δ represents the change in the concentration of the indicated species from its concentration at pH 8.1 to its concentration at the target pH value. For example, for pH 4 conditions the value of $[\mathrm{H^+}]_{\mathrm{added}}$ is positive, but it is not equal to the concentration of protons *at* pH 4, because some protons exist at the initial pH of 8.1 and most of the protons added convert bicarbonate to dissolved CO_2 rather than remaining in solution (i.e. protonating water).

Conversion of dissolved CO_2 into gaseous CO_2 is a kinetically facile processes. Thus, in Figure 38 we approximate that extractable CO_2 is equal to the equilibrium dissolved CO_2

at a given pH, although below we show that under rapid liquid flow rates and modest vacuum pressures even this amount of CO_2 is unlikely to be captured as gaseous CO_2. Figure 38B shows CO_2 extraction efficiency as a function of pH, calculated by dividing the concentration of extractable CO_2 (i.e. CO_2(aq)) by the DIC concentration. Extraction efficiency approaches 100% below pH 4, as all DIC exists in the form of dissolved CO_2. At less acidic pH values, increasing the efficiency for capturing carbon requires chemical conversion of DIC into dissolved CO_2, which we describe further below.

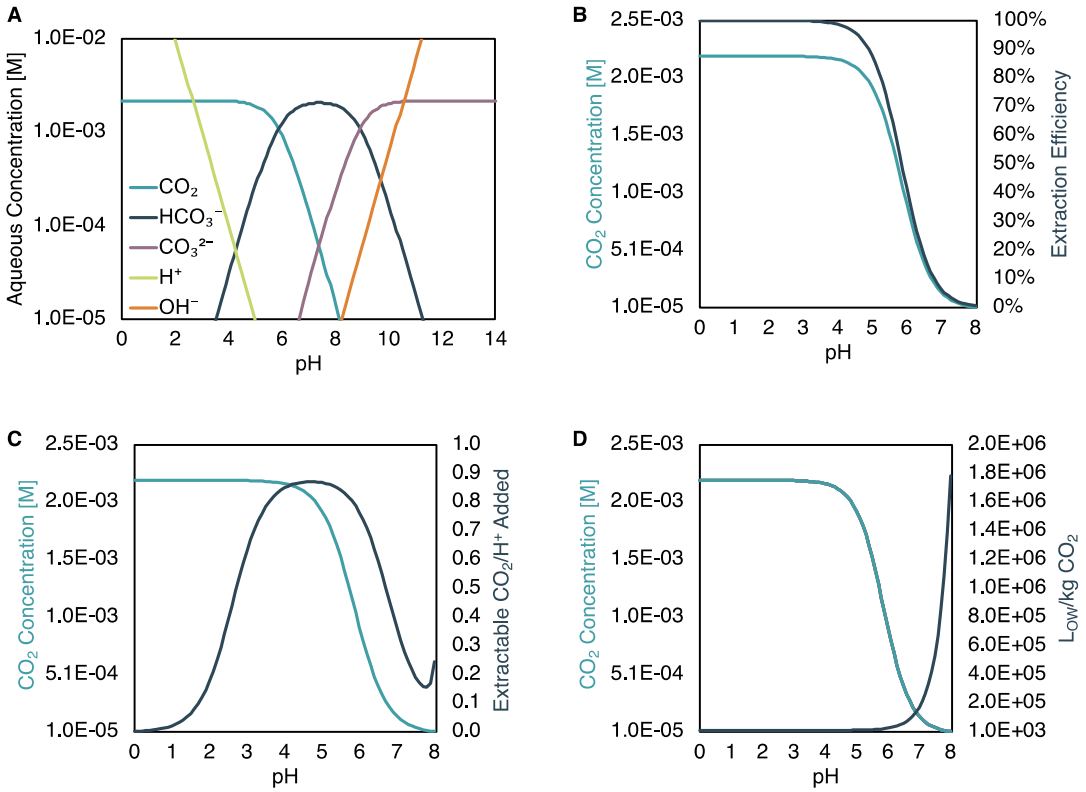

Figure 38. **The effect of membrane contactor influent pH on CO_2 extraction efficiency**. (**A**) Bjerrum plot showing DIC speciation in oceanwater. (**B**) CO_2 extraction efficiency, assuming that the equilibrium concentration of dissolved CO_2 equals the extractable CO_2. (**C**) Extractable dissolved CO_2 per proton added, as a function of pH. (**D**) Volume of oceanwater that must be processed (L), per mass of CO_2 extracted (kg), as a function of pH.

An important consideration for the projected cost of carbon under most TEA conditions is the ratio of the amount of extractable CO_2 to the amount of added protons, i.e. $[CO_2]_{extracted}/[H^+]_{added}$ (Figure 3C). This is because the cost of electricity for

electrodialytic production of acid and base is significant. For pH 4–6, the data in Figure 38C peaks, because almost every proton added converts a bicarbonate molecule to a dissolved CO_2 molecule. Below pH 4, the dissolved CO_2 concentration saturates and added protons only acidify the solution, so extractable CO_2 per protons added drops. Above pH 6, where proton concentration is $<10^{-6}$ M, a significant fraction of the added protons converts carbonate into bicarbonate (in the nanomolar range), so extractable CO_2 per protons added is also small. When extractable CO_2 per protons added is high, we are most effectively utilizing the electrodialyzer, suggesting an ideal operating pH regime of 4 – 6.

The extraction efficiency alone defines the maximum volume of intake oceanwater needed to extract a given amount of CO_2 (Figure 38D). As the pH of the influent to the membrane contactor decreases from its value for native oceanwater of ~8.1, the maximum volume needed decreases exponentially. This greatly reduces the costs associated with intake and screening of oceanwater.

A.3 Direct Oceanwater Carbon Capture System

Figure 39 presents a schematic of the offshore, stand-alone DOC system. The system can be broken down into six main process steps: 1) intake, 2) screening, 3) filtration, 4) water softening, 5) electrodialysis, and 6) CO_2 stripping. In the oceanwater intake step (step 1), centrifugal pumps bring oceanwater from 10 meters below the ocean surface onto the DOC platform. The oceanwater then passes through screens (step 2) that exclude marine life and eliminate particulates greater than 1 mm in size (*172*). The oceanwater then passes through cartridge filters (step 3) that eliminate particulates, colloidal foulants, and organic foulants greater than 5 μm in size that would otherwise degrade the membrane contactors and the membranes in the electrodialyzer (*172*). After filtration, a fraction of the oceanwater (~1%, for the base case) passes through steps 4–5 in the electrodialysis stream to produce an acidic stream and an alkaline stream (1.2 M HCl and 1.2 M NaOH in the base case). The oceanwater in the electrodialysis stream undergoes precipitation and ion exchange to remove divalent cations (Mg^{2+}, Ca^{2+}) that would otherwise combine with hydroxide ions to create mineral scalants in the alkaline chamber of the electrodialyzer (*164*). This stream serves as influent for the acid, base, and dilute chambers of the electrodialyzer, in a feed-

and-bleed mode. The electrodialyzer produces an acidic effluent stream containing 1.2 M or 3.7 wt.% HCl and an alkaline effluent stream containing 1.2 M or 4.3 wt.% NaOH. The acidified stream from the electrodialyzer is added to the remaining oceanwater from step 3, acidifying it to the target pH (pH 4, for the base case) and shifting the DIC equilibrium toward dissolved CO_2. In the CO_2 stripping step (step 6), the oceanwater passes through a gas–liquid membrane contactor where vacuum pumping is used to strip CO_2 from the acidified oceanwater. Finally, the alkaline effluent stream from the electrodialyzer is added to the decarbonized effluent stream from the membrane contactor to neutralize previously added acid, which is then returned to the ocean.

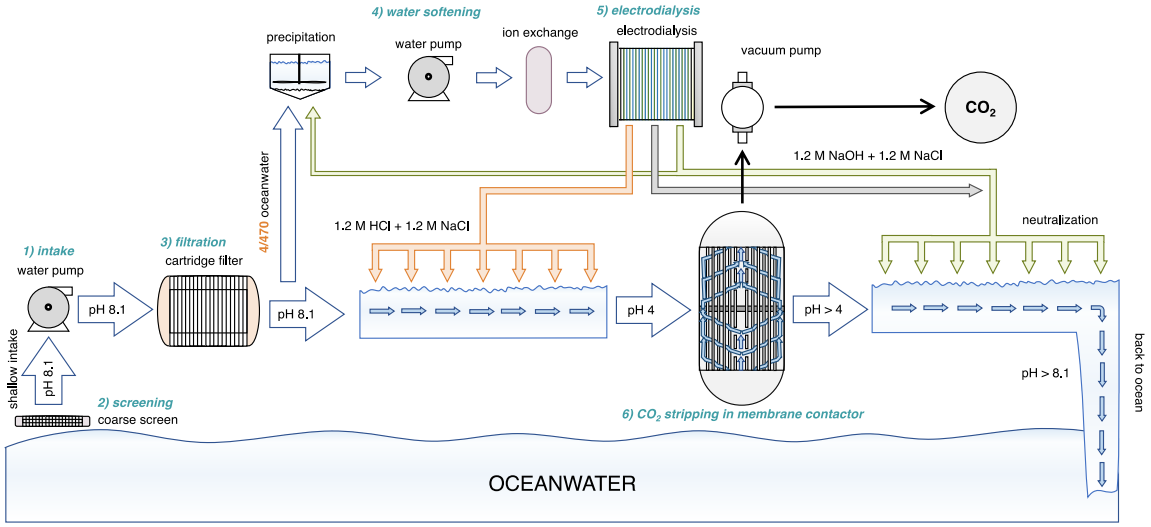

Figure 39. **Schematic of the off-shore electrochemical oceanwater carbon capture system**. The six main process steps are: 1) intake, 2) screening, 3) filtration, 4) water softening, 5) electrodialysis, and 6) CO_2 stripping. Only a small fraction of the intake oceanwater passes through steps 4–5.

A.4 Technoeconomic Analysis Model

Table 4 summarizes key inputs to the TEA. We derive capital costs for the intake and pretreatment steps (screening, filtration) from the desalination industry (*172*). Centrifugal pump, vacuum pump, and motor costs come from well-established engineering cost equations (*173*). We calculate capital costs for the electrodialysis stack based on the electrodialyzer current density and industry projections of future membrane costs (*165*). Membrane contactor costs, costs to remove divalent cations, and labor requirements have

been previously reported for a similar system (*164*). Uninstalled capital costs are scaled by a cost factor that represents additional construction costs, including electrical, piping, and instrumentation and control. We use a discounted cash flow analysis to calculate the CO_2 cost, assuming an 8% rate of return.

Table 4. **Key costs and parameter values for the technoeconomic analysis**. An asterisk indicates parameters that we vary in the TEA. Volumetric flow rates correspond to flow of water in all cases except for the vacuum pump, where they correspond to flow of gas.

Item	**Capital Cost**		**Parameter**	**Value**
Centrifugal Pump (27,000 m^3/day) (*173*)	$42,000		pH of the influent to the membrane contactor*	4
Electrodialysis membrane	$0.05/$cm^2$		Electrodialyzer current density*	500 mA/cm^2
Membrane contactor (*164*) **(1,920 m^3 /day)**	$6600		Electrodialyzer voltage*	2.5 V per cell
Vacuum pump cost (240,000 m^3/day) (*173*)	$252,000		Scale	10 kton/yr (current) 1 megaton/yr (future)
Intake piping (400,000 m^3/day) (*172*)	$420,000		Electricity cost	$0.04/kWh (current) $0.02/kWh (future)
Screening (400,000 m^3/day) (*172*)	$4,000,000		Labor cost (12.5 full-time employees at 10-kton/year scale)	$40,000/year average salary
Cartridge filtration (400,000 m^3/day) (*172*)	$3,900,000		Extraction efficiency	86%
Ion exchanger (720 m^3/day) (*164*)	$120,700		Steady-state CO_2 partial pressure*	6.7 Torr

Since data is available on desalination plants that process oceanwater at a volumetric flow rate of up to 400,000 m^3/day, we define that as the baseline capacity, which corresponds to a maximum CO_2 capture rate of 12.7 kton/year. To scale capital costs up or down from that baseline capacity, we use the commonly adopted 6/10 scaling rule (*174*):

$$C_2 = C_1 \left(\frac{S_2}{S_1}\right)^{6/10}$$

where C_1 and C_2 are the costs at the initial and final scales, respectively, and S_1 and S_2 are the oceanwater flow rates at the initial and final scales, respectively.

We analyze two different scenarios: a "current" scenario, where the CO_2 capture rate is 10 kton/year and electricity costs \$0.04/kWh; and a "future" scenario, where the CO_2 capture rate is 1 megaton/year and electricity costs \$0.02/kWh. In our base case, the influent to the membrane contactor has a pH equal to 4 and the electrodialyzer operates at 500 mA/cm^2 and 2.5 V. We vary all three of these parameters in subsequent parts of this work. The CO_2 partial pressure in the membrane contactor and the extraction efficiency are both defined by the chemical kinetics model, as described below. Where not otherwise specified, analyses assume base-case parameters and the "future" scenario.

A.5 Chemical Kinetics Model

Our collaborators at UC Irvine implement a chemical kinetics model of DIC speciation to better understand the extraction efficiency under realistic flow rates for liquids and gases into and out of the membrane contactor, depicted in Figure 40.

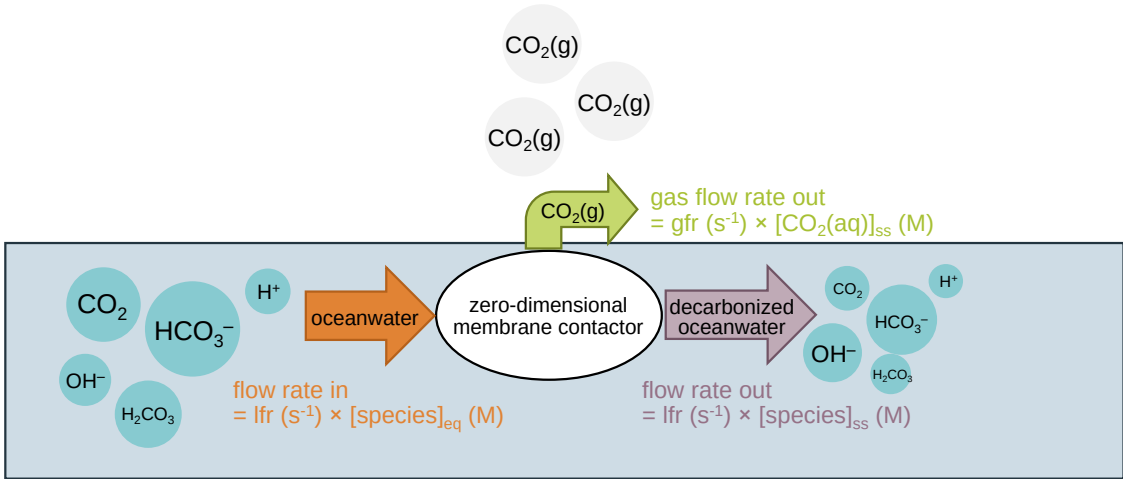

Figure 40. **Schematic of the zero-dimensional finite-element chemical kinetics model of the membrane contactor.**

The importance of this steady-state chemical kinetics analysis is made clear by considering two extreme operating conditions. If oceanwater is quickly flowed through the membrane contactor and/or CO_2 is slowly extracted (i.e. higher vacuum pressure is used), the equilibrium concentration of dissolved CO_2 will not be extracted, and some will remain in solution. If oceanwater is flowed slowly through the membrane contactor and/or CO_2 is quickly extracted (i.e. lower vacuum pressure is used), the amount of CO_2 extracted could exceed the equilibrium concentration of dissolved CO_2 due to chemical interconversion of other DIC (HCO_3^-, CO_3^{2-}) into dissolved CO_2 per Le Chatelier's principle.

The zero-dimensional finite element model reports two key operational parameters—the extraction efficiency and steady-state partial pressure of CO_2 in the membrane contactor—as a function of liquid flow rate of oceanwater into the contactor (assumed to be the same as the liquid flow rate out of the contactor), gas flow rate of CO_2 out of the contactor, and pH of the oceanwater flowing into the contactor. The model incorporates chemical reactions relevant to acidic DIC speciation in oceanwater, primarily proton transfer reactions between DIC species (CO_2, H_2CO_3, HCO_3^-, CO_3^{2-}) and water (H_2O) and its ions (H^+, OH^-), but does not include explicit water and therefore does not account for its phase change into water vapor. Previously published values for two of the rate constants and equilibrium constant are used to determine the third value, using $K = k_f/k_b$. This is considered for the minimal set of reactions that cannot be defined via linear combinations of others using Hess's law. Mass transfer phenomena are not incorporated into the model, which is a reasonable assumption given presumed rapid rates of transport of CO_2 across tens-of-microns-thick walls of fibers used in commercial gas–liquid membrane contactors and the length-to-diameter ratio of fibers, which ensures rapid radial mixing within the microfibers at commercially relevant flow rates.

Simulations are performed until steady state is reached. The extraction efficiency of the membrane contactor is calculated by dividing the gaseous flow rate of CO_2 out of the membrane contactor by the influent DIC flow rate. An extraction efficiency of 100% means that all DIC, whether it originally existed as dissolved CO_2, H_2CO_3, HCO_3^-, or CO_3^{2-}, is extracted in the form of gaseous CO_2.

A.6 Integrating Technoeconomic Analysis with a Chemical Kinetics Model for the Membrane Contactor Reveals Ideal Steady-State Operating Points

Using the chemical kinetics model, we map extraction efficiency as a function of three operating parameters: the pH of the oceanwater that is flowed into the membrane contactor, the flow rate of water into the contactor, and the vacuum being applied to the contactor in order to draw off gaseous CO_2 (Figure 41A and Figure 41C). When pH 4 oceanwater is flowed into the contactor, extraction efficiency is above 90% as long as at least 5 Torr of vacuum is applied (Figure 41A). This high efficiency is not surprising, because nearly all DIC that flows into the contactor already exists as dissolved CO_2 (Figure 38A) and so only a phase change must occur to extract gaseous CO_2.

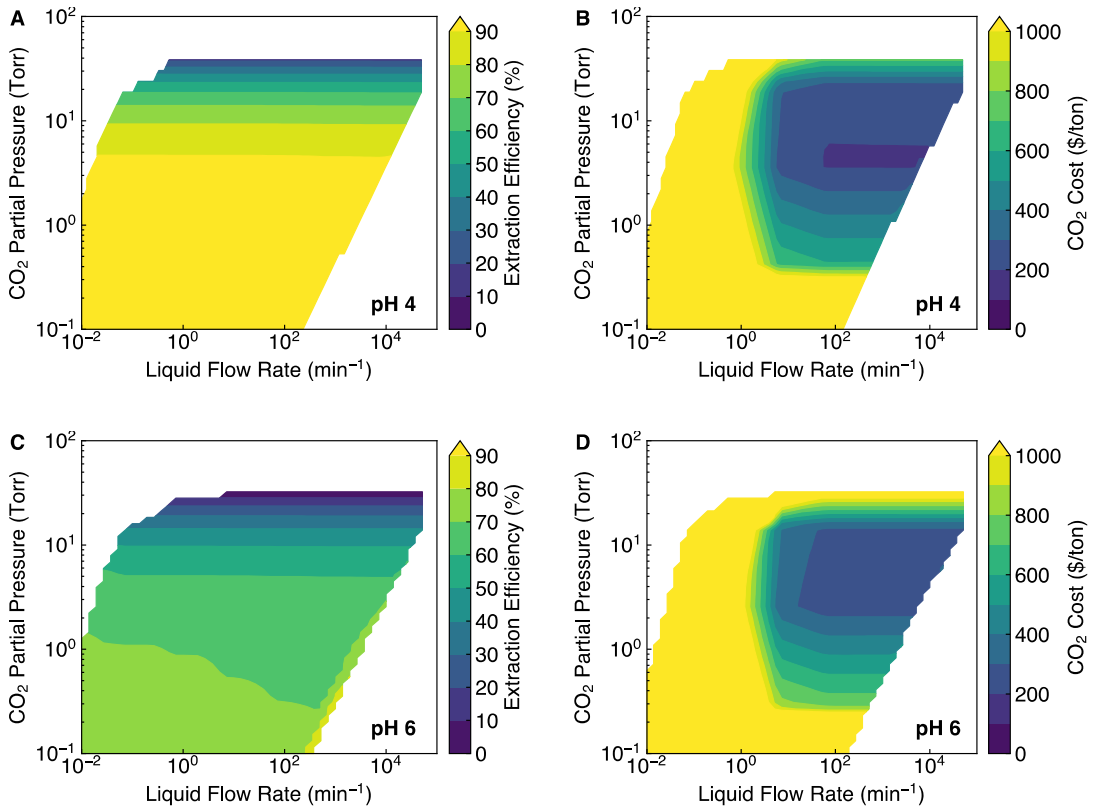

Figure 41. **Projected CO_2 costs under steady-state operation.** (**A**) Extraction efficiency for an influx pH of 4 as a function of CO_2 partial pressure and liquid flow rate as determined by the chemical kinetics model. (**B**) CO_2 cost for the conditions in panel A calculated from TEA. (**C**) Extraction efficiency for an influx pH of 6 as a function of CO_2 partial pressure and liquid flow rate as determined by the chemical kinetics model. (**D**) CO_2 cost for the conditions in panel C calculated from TEA.

However, when pH 6 oceanwater is used, only about 60% extraction efficiency can be achieved for the same ranges of liquid flow rate and partial pressure, due to a majority of DIC existing as HCO_3^- rather than dissolved CO_2 (Figure 41B). As a result, chemical reactions must occur to convert HCO_3^- to dissolved CO_2 before it can form gaseous CO_2 that can be extracted by the vacuum. Evidence of chemical interconversions playing a role in the extraction efficiency can be seen in the bottom left corner of Figure 41C, where efficiencies around 70% are achieved at slow liquid flow rates. When the weakly acidified oceanwater has a long residence time in the membrane contactor due to a slow liquid flow rate, the process of gaseous CO_2 being collected by the vacuum triggers dissolved CO_2 to enter the gas phase so the equilibrium dictated by Henry's law is preserved. Subsequently, Le Chatelier's principle drives HCO_3^- to become dissolved CO_2 to replenish CO_2 that previously entered the gas phase. These observations highlight the utility of the chemical kinetics model for the membrane contactor to capture the interplay of chemical reaction rates, liquid flow rate, vacuum pressure, and influx pH.

To calculate the CO_2 cost for steady-state operation of the membrane contactor, we use the outputs from the zero-dimensional chemical kinetics model as inputs to the TEA. We use the steady-state extraction efficiency and the steady-state CO_2 partial pressure directly as TEA inputs. To account for the liquid flow rate, we calculate the zero-dimensional liquid flow rate (min^{-1}) of the commercial membrane contactor used in our TEA by dividing the maximum volumetric flow rate of liquid through the contactor (L min^{-1}), determined by the membrane contactor specifications, by the volume of the membrane contactor (L). If the steady-state liquid flow rate is less than the maximum liquid flow rate specified by the membrane contactor, we require the oceanwater flow to be split between more membrane contactors, as the total oceanwater volumetric flow rate must remain constant for a given CO_2 mass flow rate. We do not allow the steady-state liquid flow rate to exceed the maximum liquid flow rate specified by the membrane contactor, so the CO_2 cost levels off above that maximum flow rate.

At pH 4, the equilibrium concentration of dissolved CO_2 is close to 100% of the DIC. However, at partial pressures greater than 5 Torr, the chemical kinetics model shows that extraction efficiencies drop below 90% at all liquid flow rates (Figure 41B). The lowest-

cost operating point occurs at an extraction efficiency of 86%, a partial pressure of 6.7 Torr, and a liquid flow rate of 60 min^{-1}, yielding a CO_2 cost of $175/ton (Figure 41D). For a membrane contactor influent at pH 6, extraction efficiencies larger than the equilibrium concentration of dissolved CO_2, which is only 42%, can be observed at low partial pressures and low liquid flow rates (Figure 41D). The lowest-cost operating point occurs at an extraction efficiency of 60%, a partial pressure of 4.8 Torr, and a liquid flow rate of 60 min^{-1}, yielding a CO_2 cost of $226/ton (Figure 41E). Coupling the TEA and chemical kinetics model yields an accurate CO_2 cost and demonstrates that operation using an influent to the membrane contactor that is at pH 4 – 6 could provide a cost-effective means to capture anthropogenic CO_2 dissolved in oceanwater.

A.7 Technoeconomic Analysis Projects Low CO_2 Cost at Megaton/Year Scale

We use the lowest-cost steady-state operating point at pH 4 as the "base case" for our TEA, with a CO_2 partial pressure of 6.7 Torr and an extraction efficiency of 86%. In the "current" scenario (10 kton/year and $0.04/kWh electricity cost), we calculate a levelized CO_2 cost of $861/ton. In the "future" scenario (1 megaton/year and $0.02/kWh electricity cost), we calculate a levelized CO_2 cost of $175/ton. Figure 42A shows that capital costs (CapEx) and replacements account for 50% of the CO_2 cost in the "current" scenario. In the "future" scenario, electricity accounts for 39% of the CO_2 cost, and CapEx and replacements account for another 39% of the CO_2 cost (Figure 42B). Although the scale of the "future" scenario is 100 times larger, the CapEx is only 15 times larger by the 6/10 rule, making the CapEx a less significant contributor to the CO_2 cost at larger scales. The 6/10 rule is no longer accurate for scaling beyond the megaton/year scale, so we do not project costs out to the gigaton/year scale. However, a CO_2 cost of $175/ton at the megaton/year scale puts our oceanwater carbon capture system on track to achieving a CO_2 capture cost below $100/ton at the gigaton/year scale, which is the target set by the U.S. Department of Energy for its Carbon Negative Shot (*175*).

Although the CapEx and electricity constitute different percentages of the CO_2 cost in the "current" and the "future" scenarios, the CapEx and electricity breakdown by process step is the same in both scenarios. CO_2 stripping costs, including membrane contactors and

vacuum pumps, dominate the capital cost, followed by water softening, screening, filtration, and intake (Figure 42C). Electrodialysis represents a relatively small contribution to the capital cost, demonstrating that passing only a small fraction of the intake oceanwater through the electrodialyzer successfully reduces capital cost. Figure 42D shows that electrodialysis electricity dominates the electricity cost, followed by intake and CO_2 stripping. Electricity is the main contributor to the variable operating costs (OpEx).

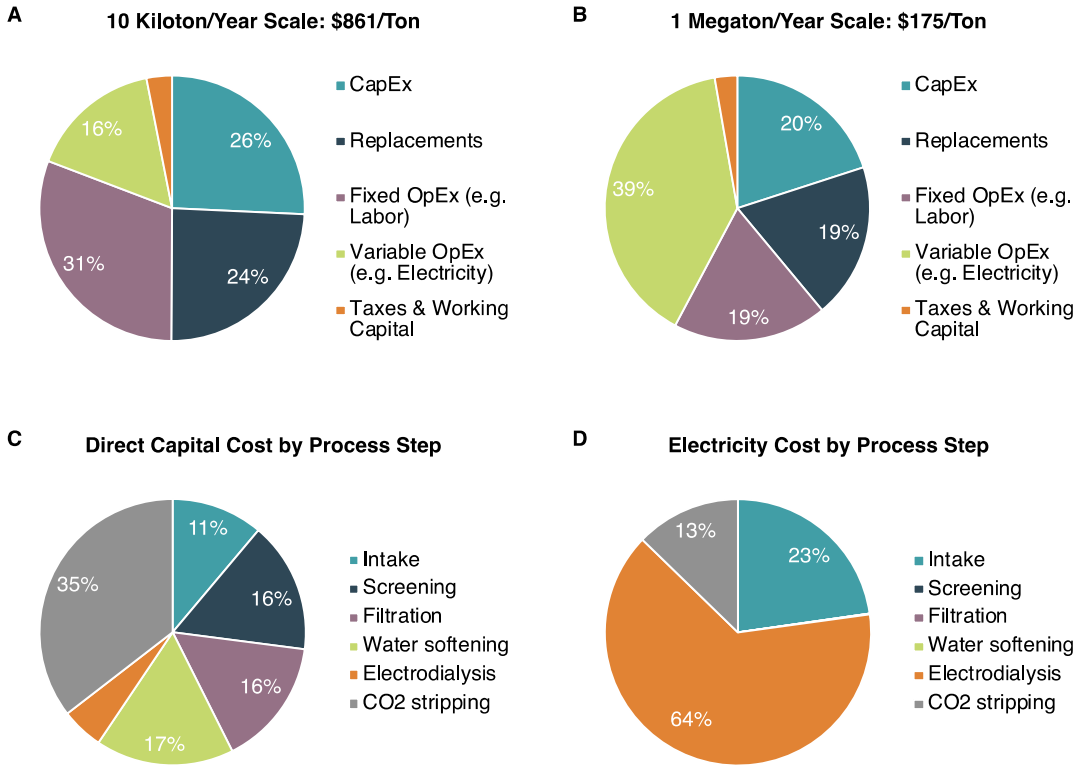

Figure 42. **Cost breakdown of carbon capture costs at different scales.** (**A**) Cost breakdown in "current" scenario (10-kton/year scale and $0.04/kWh electricity cost). (**B**) Cost breakdown in "future" scenario (1-megaton/year scale and $0.02/kWh electricity cost). (**C**) Capital cost breakdown by process step. (**D**) Electricity cost breakdown by process step.

A.8 Electrodialyzer Current, Electrodialyzer Voltage, and Membrane Contactor Pressure Are Key Drivers of System Cost

In Figure 43, we vary key parameters of our electrochemical oceanwater carbon capture system that we can control experimentally, and examine their effect on CO_2 cost.

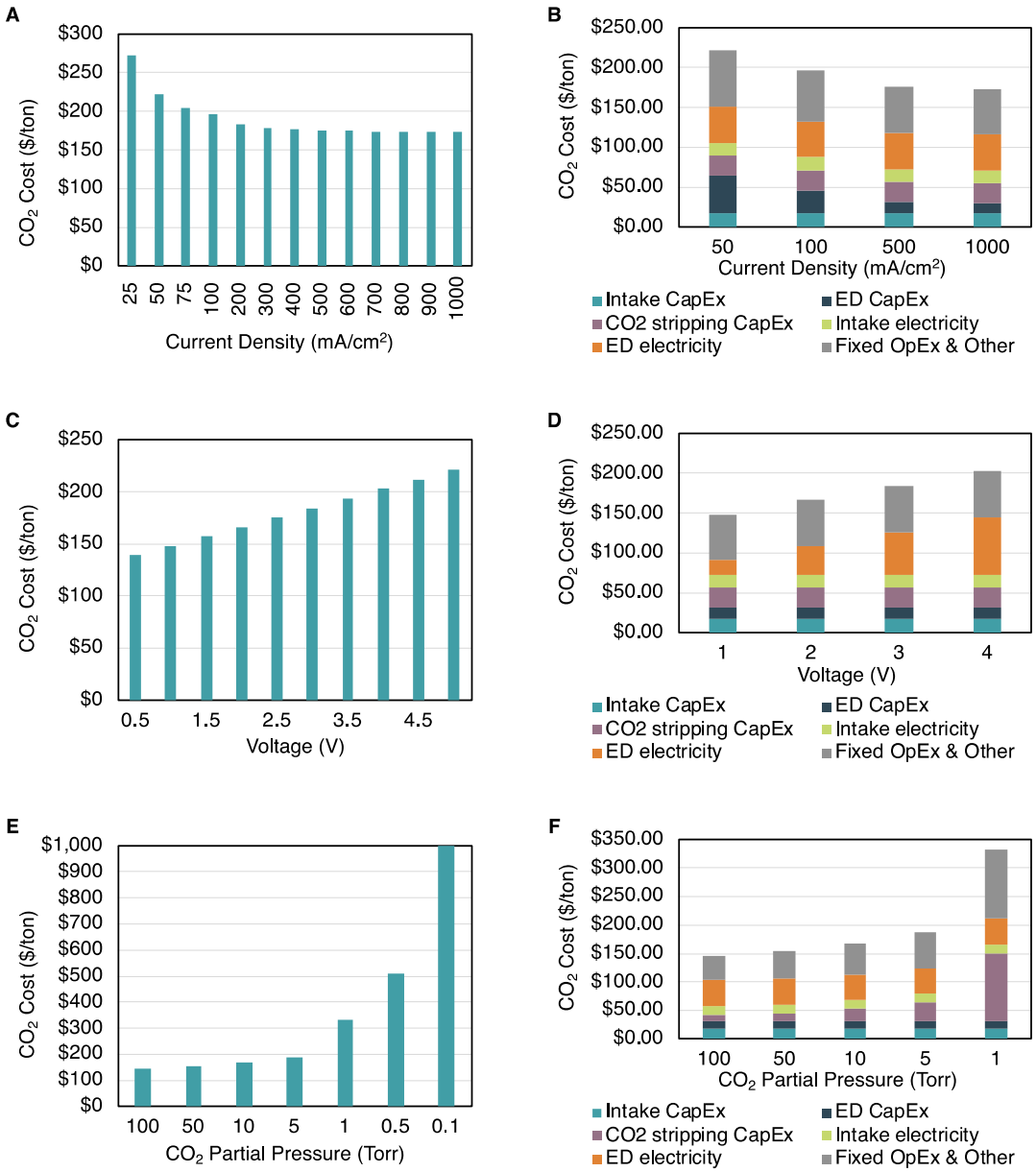

Figure 43. **CO_2 cost sensitivity to key drivers of system cost**. (**A**, **B**) The effect of electrodialyzer current density on CO_2 cost (**A**) and cost breakdown (**B**), with electrodialyzer voltage 2.5 V and CO_2 partial pressure 6.7 Torr. (**C**, **D**) The effect of electrodialyzer voltage on CO_2 cost (**C**) and cost breakdown (**D**), with electrodialyzer current density 500 mA/cm^2 and CO_2 partial pressure 6.7 Torr. (**E**, **F**) The effect of CO_2 partial pressure in the membrane contactor (and correspondingly, vacuum pump base pressure) on CO_2 cost (**E**) and cost breakdown (**F**), with electrodialyzer current density 500 mA/cm^2 and electrodialyzer voltage 2.5 V. Cost breakdowns show most significant contributors to CapEx and OpEx; all else is encompassed in "Fixed OpEx & Other." Analysis assumes "future" scenario (1 megaton/year scale, $0.02/kWh electricity cost).

These include the electrodialyzer current density, the electrodialyzer voltage, and the vacuum pressure in the membrane contactor. The following analysis assumes the "future" scenario (1-megaton/year scale, $0.02/kWh electricity cost), but similar findings hold in the "current" scenario.

Increasing the electrodialyzer operating current density is beneficial up to ~500 mA/cm^2, with diminishing returns at higher current densities (Figure 43A). The electrodialyzer current density only affects the electrodialyzer CapEx, which is given by (*165*):

$$\mathrm{C} = \mathrm{c_A} \cdot \frac{1}{\mathrm{j}} \cdot \mathrm{F} \cdot \mathrm{x} \cdot [\mathrm{H^+}]_{\mathrm{added}} \cdot Q_{OW}$$

where C is the electrodialyzer CapEx (in $), $\mathrm{c_A}$ is the membrane cost per unit area (in $\frac{\$}{\mathrm{cm^2}}$), j is the current density, F is the Faraday constant, x is the fraction of oceanwater that is acidified to produce 1.2 M HCl, $[\mathrm{H^+}]_{\mathrm{added}}$ is the concentration of acid produced by electrodialysis, and Q_{OW} is the oceanwater volumetric flow rate in liters per second. Figure 43B shows that as current density increases beyond 500 mA/cm^2, the electrodialyzer CapEx and CO_2 cost level off, as the electrodialyzer CapEx becomes equal to the cost of the pumps and storage tanks.

Decreasing the electrodialyzer operating voltage reduces the CO_2 cost monotonically (Figure 43C). Opposite to the electrodialyzer current density, the electrodialyzer voltage affects only the electrodialyzer electricity cost (the main contributor to electrodialyzer OpEx) by affecting the electrodialysis energy usage. The electrodialysis energy per CO_2 output is given by:

$$\frac{\mathrm{J}}{\mathrm{kg_{CO_2}}} = \mathrm{V} \cdot \mathrm{F} \cdot \mathrm{x} \cdot [\mathrm{H^+}]_{\mathrm{added}} \cdot \frac{\mathrm{Q_{OW}}}{\mathrm{Q_{CO_2}}}$$

where V is the electrodialyzer voltage and $\mathrm{Q_{CO_2}}$ is the CO_2 mass flow rate in kilograms per second. The electrodialyzer electricity remains a significant contributor to the CO_2 cost down to the thermodynamic limit for water dissociation of ~0.8 V, so reducing the electrodialyzer operating voltage is always beneficial (Figure 43D).

Finally, we find that CO_2 cost is very sensitive to the CO_2 partial pressure in the membrane contactor (Figure 43E). The CO_2 partial pressure has been determined experimentally to be about 60% of the vacuum pump base pressure (*165*). Along with a fixed base pressure, most vacuum pumps also have a maximum volumetric flow rate or pumping speed, since they operate as positive displacement pumps (repeatedly removing a fixed volume of gas). At lower CO_2 partial pressures and the same *volumetric* flow rate of gas out of the membrane contactor, the *molar* flow rate of CO_2 becomes much smaller due to the ideal gas law. Thus, if each vacuum pump is operating at its maximum pumping speed, reducing the CO_2 partial pressure from 10 to 1 Torr would increase the number of pumps needed to achieve a given CO_2 mass flow rate by a factor of 10. As the CO_2 partial pressure decreases (and correspondingly, the vacuum pump base pressure decreases), the CO_2 stripping CapEx increases due to the increase in number of vacuum pumps required (Figure 43F). This effect becomes significant around 1 Torr, suggesting that operating at vacuum pump base pressures below 1 Torr will be cost-prohibitive given the pumping speed of current pumps.

Since the dissolved CO_2 concentration determines the equilibrium (maximum) partial pressure of gaseous CO_2 in the membrane contactor via Henry's Law, operating at a higher pH will require a lower vacuum pressure to achieve maximum extraction. Further, if no external acid is added, CO_2 extraction from bicarbonate will generate stoichiometric base in the form of carbonate and/or hydroxide. This more alkaline solution will have a lower equilibrium concentration of dissolved CO_2, and therefore a lower equilibrium partial pressure of gaseous CO_2, requiring an even lower vacuum pressure to capture CO_2. Therefore, the limitations on vacuum pressure also limit the steady-state operating pH in the membrane contactor to values where the Henry's Law CO_2 partial pressure defined by the equilibrium concentration of dissolved CO_2 is greater than 1 Torr, which is $pH < 7.5$.

A.9 Low Cost is Possible With Low Capacity Factor Power Generation

For maximum climate benefit, carbon capture technologies should be powered by renewable sources of power generation, which often are variable and have capacity factors lower than 100%. To explore the potential of different power generation sources for an offshore oceanwater carbon capture system, we vary electricity cost and capacity factor

and calculate the resulting CO_2 cost (Figure 44). At an electricity cost of \$0.02/kWh, already achieved by the least expensive photovoltaic power-purchase agreements (*176*), capacity factors of 40% are tolerable while retaining a CO_2 cost less than \$300/ton. Wind power (\$0.03/kWh, 50% capacity factor) (*177*) or solar-plus-storage (\$0.04/kWh, 60% capacity factor) (*178*) could also be viable electricity sources.

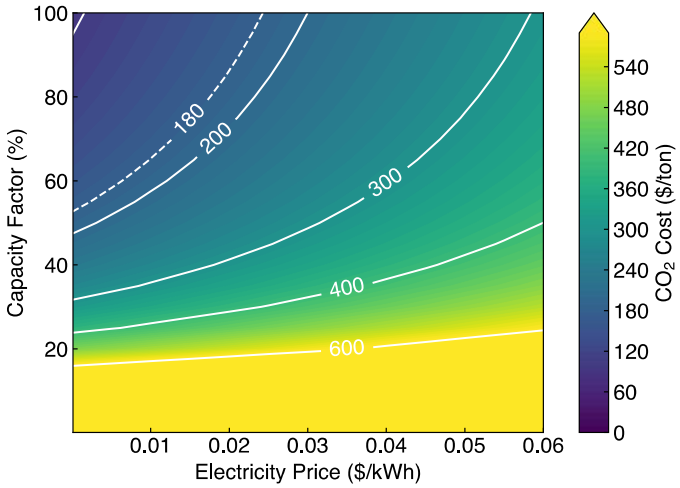

Figure 44. **CO_2 cost with different power generation sources**. Power generation sources are characterized by different electricity costs and capacity factors and modeled assuming the "future" scenario. The \$180/ton line represents the proposed CO_2 capture cost in the new 45Q tax credits.

In the future, increased penetration of renewables on the grid may lead to a need for curtailment: using extra electricity when wind and solar are overproducing to balance the grid. In this scenario, consumers may be able to access nearly free electricity at certain times of the day or year. If electricity is free, we find that capacity factors as low as 50%—meaning the system would only be operating on average half the time over the course of a year—can lead to a CO_2 cost of <\$200/ton.

A.10 Catalyzing CO_2 Extraction Shifts Ideal Operating pH

The ideal pH of the influent to the membrane contactor can differ from 4 if we speed up the conversion of bicarbonate into dissolved CO_2 using catalysts, such as natural or artificial carbonic anhydrase. Figure 45 explores three cases with different assumptions for extraction efficiency, each of which leads to a different ideal pH.

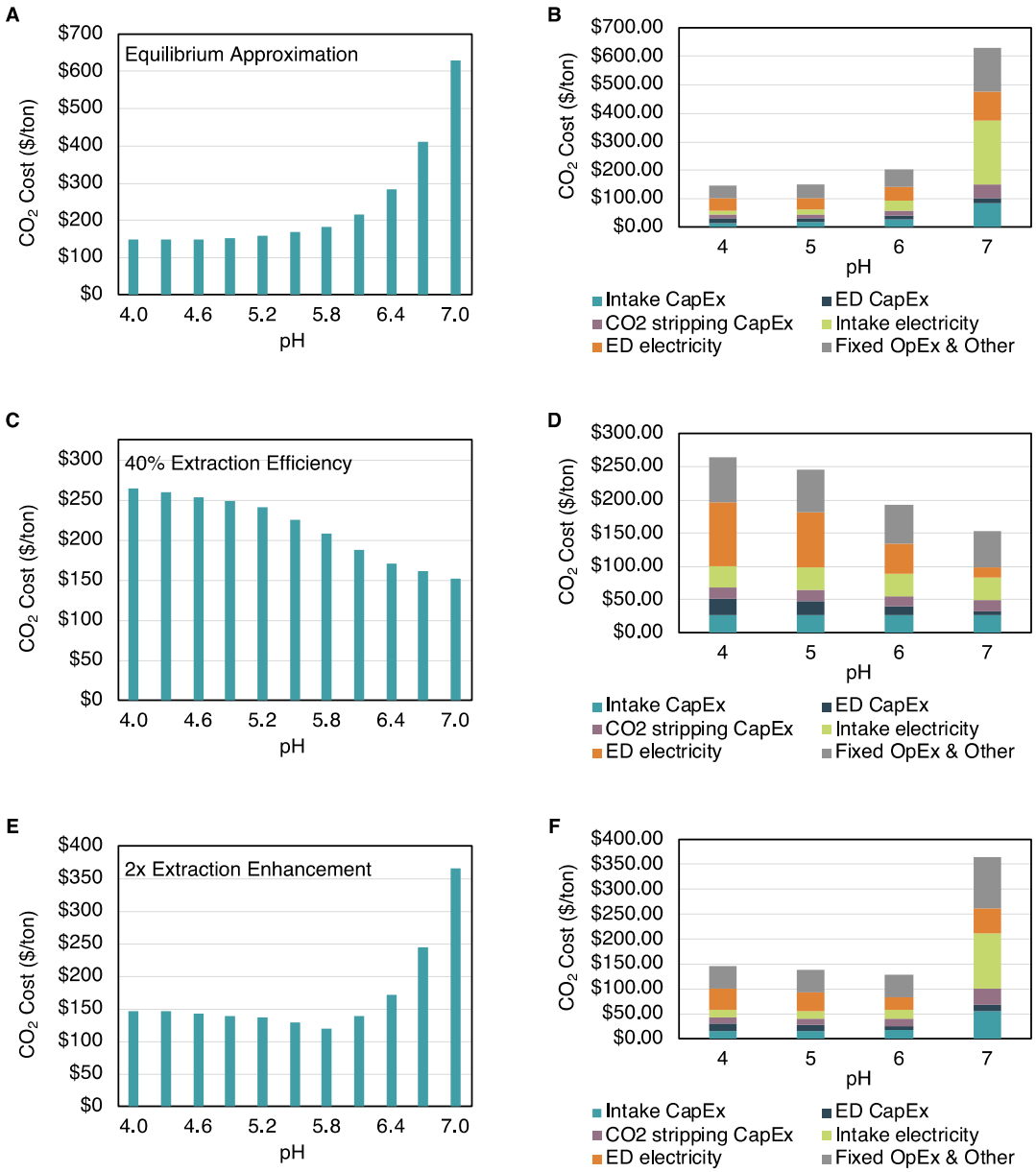

Figure 45. **pH parameter sweeps, assuming varying effects of catalysis on extraction efficiency.** (**A**, **B**) CO_2 cost as a function of pH (**A**) and cost breakdown (**B**) assuming that the extractable CO_2 is equal to the equilibrium concentration of dissolved CO_2. (**C**, **D**) CO_2 cost as a function of pH (**C**) and cost breakdown (**D**) assuming a constant 40% extraction efficiency for all pH values. (**E**, **F**) CO_2 cost as a function of pH (**E**) and cost breakdown (**F**) assuming a 2x enhancement in extraction efficiency is achieved (without exceeding 100%) for all pH values. Cost breakdowns show most significant contributors to CapEx and OpEx; all else is encompassed in "Fixed OpEx & Other." Analysis assumes "future" scenario (1-megaton/year scale, $0.02/kWh electricity cost).

First, we examine CO_2 cost as a function of pH. Rather than calculating the extraction efficiency from the 0D model, we use the approximation that the extractable CO_2 is equal to the dissolved CO_2. We calculate the extraction efficiency by dividing the concentration of dissolved CO_2 by the total DIC concentration, as in Figure 38B. With this approximation, CO_2 cost increases as pH increases due to decreased extraction efficiency (Figure 45A). Figure 45B demonstrates that this decreased extraction efficiency mostly increases the intake electricity cost, since at lower extraction efficiencies, a larger volume of oceanwater must be processed to extract the same amount of CO_2. In this scenario, operating at pH 4 would be optimal.

Second, we assume that we can achieve a constant extraction efficiency of 40% independent of the pH of the membrane contactor influent. In this case, CO_2 cost decreases as pH increases (Figure 45C). As pH increases, a smaller fraction of the oceanwater needs to be acidified through electrodialysis, and if we achieve the same extraction efficiency, this leads to savings in electrodialysis electricity (Figure 45D). If we were able to achieve extraction efficiencies close to 40% at any initial pH condition, operation using native oceanwater would be optimal and an electrodialyzer would not be needed.

Third, we assume that we can double the extraction efficiency at any pH (without exceeding 100%), for example via catalytic enhancement of the observed rate of dissolved CO_2 formation from bicarbonate. In this case, CO_2 cost reaches a minimum at an intermediate pH value for the membrane contactor influent of 5.8 (Figure 45E). Figure 45F demonstrates that this intermediate pH achieves a tradeoff between electrodialysis electricity and intake electricity. If we were able to enhance extraction efficiency by a small factor, utilizing membrane contactor influent at an intermediate pH would be optimal.

There are limitations to this catalytic approach. Although catalysis can enhance the conversion rate of bicarbonate into dissolved CO_2, it cannot increase the dissolved CO_2 concentration beyond the equilibrium concentration. As discussed above, the steady-state operating pH in the membrane contactor cannot exceed pH 7.5 to avoid prohibitively high vacuum pump costs. Therefore, with or without catalysis, acidifying the oceanwater to a pH less than its native pH of 8.1 will be necessary.

A.11 Conclusion

We have presented here a technoeconomic analysis of a system that captures CO_2 directly from oceanwater. In our system, we acidify a fraction of the oceanwater using bipolar membrane electrodialysis, then add that acid stream back into the main oceanwater stream to reach an operating pH (pH 4, in our base case) that shifts the carbonate balance toward dissolved CO_2. We pass the acidified oceanwater through a gas–liquid membrane contactor to extract CO_2 and then neutralize it with the base stream from the electrodialyzer. The decarbonized, neutralized oceanwater is returned to the ocean to absorb more atmospheric CO_2 and the captured CO_2 can either be pumped under the ocean floor for storage, or compressed and transported.

We develop a zero-dimensional finite element model to simulate the membrane contactor, and we map CO_2 extraction efficiency as a function of three important operating parameters: the pH of the ocean water that is fed into the contactor, the flow rate of water into the contactor, and the vacuum being applied to the contactor in order to draw off CO_2. By coupling this thermodynamic model with the TEA, we determine the lowest-cost steady-state operating point for our system for a given pH, which for pH 4 influent to the membrane contactor corresponds an extraction efficiency of 86%.

Using this steady-state operating point as our base case, we perform TEA at different scales of CO_2 capture: one where we capture 10 kilotons of CO_2 per year (CO_2 cost \$861/ton) and one where we capture 1 megaton of CO_2 per year (CO_2 cost \$175/ton), putting us on track to achieve \$100/ton at the 1-gigaton/year scale. We achieve much lower CO_2 costs than previous estimates for oceanwater CO_2 capture mostly due to 1) improved electrodialyzer performance 2) larger scale and 3) the use of a stand-alone, offshore system to reduce intake/outfall costs.

We examine a variety of drivers of system cost that can be controlled experimentally in future stages of this research. We find that CapEx is proportional only to electrodialyzer current density, and OpEx is proportional only to electrodialyzer voltage. Beyond 500 mA/cm^2, increasing the current density has little impact on the CO_2 cost, but decreasing the voltage has benefits down to 1 V per cell. We also find that the steady-state

partial pressure of CO_2 in our membrane contactor must be greater than 1 Torr to avoid prohibitively large vacuum pump costs. Finally, we find that if electricity is inexpensive, we can tolerate a low capacity factor (e.g. from a variable renewable source of energy such as solar or offshore wind).

This analysis demonstrates that DOC is a potentially viable option for large-scale carbon capture and should be added to the existing portfolio of NETs (including DAC, AR, and BECCS). As DIC in oceanwater is 120 times more concentrated than CO_2 in the atmosphere, DOC has the potential to be more energy-efficient than DAC. Further, we design a stand-alone, offshore system, eliminating the significant risks to land availability and food costs presented by technologies like BECCS and AR. In conjunction with immediate mitigation strategies—mainly a steep decline in fossil fuel use—a portfolio of NETs that includes DOC could help limit warming to 1.5ºC.

Appendix B: Fabrication Methods

Device Fabrication

Template-stripped Ag and Au substrates are prepared as described previously (*34*, *48*). WS_2 is mechanically exfoliated directly onto template-stripped Ag (for Schottky-junction devices) or onto PTAA-coated template-stripped Au (for carrier-selective contact devices) from the bulk crystal (HQ Graphene) using Scotch tape. PTAA is spin-coated from a 1.5 mg/mL solution in toluene at 6000 rpm for 30 s, then baked at 100ºC for 10 minutes on a hot plate to crystallize the film.

For Schottky-junction transferred contact devices, Au top contacts are prepared and transferred using the metal transfer technique described below. For evaporated contact devices, Au top contacts are patterned using standard photolithography techniques as described previously (*34*). Contacts are fabricated on WS_2 within 12 hours of exfoliation.

For carrier-selective contact devices, C60, BCP, and Ag are sequentially evaporated in a thermal evaporator at a base pressure below 10^{-6} Torr. C60 is evaporated at 0.3 Å/s, BCP is evaporated at 0.2 Å/s, and Ag is evaporated at 0.7 Å/s. Ag disks are defined using positive photolithography with a positive resist (S1813), and the Ag outside of the photoresist is etched away using Transene Gold Etchant diluted by 50% in water. Contacts are fabricated on WS_2 within 24 hours of exfoliation. The photoresist is dissolved in heated acetone (60ºC).

Final layer thicknesses are confirmed using atomic force microscopy (Asylum Research).

Detailed Metal Transfer Procedure

To make metal contacts on SAM-coated Si/SiO_2, commercially-available Si wafers coated with 285 nm thermal SiO_2 are diced into chips, cleaned in Nanostrip for 5 minutes, then rinsed 3 times in DI water. The chips are placed in a vacuum desiccator. 5 drops of trichloro(1H,1H,2H,2H-perfluorooctyl)silane (PFOTS, Sigma Aldrich) are placed in a cap in the bottom of the desiccator. The desiccator is evacuated slowly, over the course of 3

minutes, then isolated from the vacuum pump and left evacuated for 1 hour. The chips are removed from the vacuum desiccator. 20 nm of Au is evaporated in an electron-beam evaporator at a speed of 1 Å/s and a base pressure below 5×10^{-7} Torr. Photolithography is performed using positive photoresist and a positive photomask to define the contacts. For photolithography, S1813 is used according to the following recipe: spin at 4000 rpm for 30 seconds, soft bake at 115ºC for 1 minute, expose to 365 nm UV light at 15 mW/cm^2 for 8 seconds, develop in MF 319 for 50 seconds, and then rinse in DI water for 10 seconds. The Au around the photoresist is etched by immersion of the chips in Transene Gold Etchant TFA for 10 seconds, then the sample is rinsed in DI water. The photoresist is dissolved in slightly heated acetone (60ºC for 5 minutes).

To make the PDMS/PPC stamps, a similar procedure is followed to that developed in (*51*). PDMS (Sylgard 184) is mixed in a glass petri dish and left in an oven at 60-70ºC overnight. PPC is made by stirring 1.5 g PPC in 10 mL anisole on a hot plate at 60ºC for 1 hour. The PDMS is cut into 1 cm by 1 cm squares with a razor blade. One square is removed from the petri dish, rinsed in IPA for 20 seconds, then dried in nitrogen gas. The PDMS stamp is placed on one end of a glass slide, and the thickest corner of the stamp is identified. The PDMS stamps are plasma-ashed at 300 mTorr and 120 W for 10 minutes. The PDMS stamp is centered on the spinner, and 2 drops of PPC are placed on the PDMS stamp, and then spun at 1500 rpm for 1 minute. The PDMS/PPC stamps are left to sit for a few minutes, but not longer than 10 minutes. The edges of the PDMS/PPC stamp are cut away with a fresh razor blade until the stamp is ~2 mm by 2 mm.

To transfer metal contacts, the stage of a 2D transfer setup is heated to 60ºC. A Si/SiO_2 chip containing metal contacts is loaded onto the stage, and the desired contact is centered in the field of view. The PDMS/PPC stamp is loaded onto the top arm of the transfer setup. The thickest corner of the PDMS/PPC stamp is centered in the field of view. When the stamp is lowered, the polymer front should originate from this corner. The PDMS/PPC stamp and the desired contact are aligned so that the PPC completely covers the contact, but so that just the corner of the stamp will make contact with the substrate. The PDMS/PPC stamp is lowered slowly. Once the polymer front progresses just past the contact, the stage temperature is lowered to 40ºC. After the temperature has reached 40ºC,

the top arm of the transfer setup is raised slowly. As the polymer front begins to move, but before it reaches the contact, the top arm of the transfer setup and therefore the PDMS/PPC stamp is raised very quickly, picking up the contact with it. The stage of the transfer setup is heated to 60ºC again. The target substrate is loaded onto the stage of the transfer setup and the target flake is centered in the field of view. Once the temperature reaches 60ºC, the contact on the PDMS/PPC stamp is aligned with the flake. The PMDS/PPC stamp is lowered slowly, until the polymer front progresses just past the sample. Immediately, and with the stage still at 60ºC, the PDMS/PPC stamp is raised very slowly. The contact should delaminate from the stamp and stick to the flake. Remaining PPC that occasionally sticks to the flake can be removed by rinsing in chloroform for 5 minutes, and then drying in nitrogen gas.

Photocurrent and Power-Dependent I-V

Photocurrent and power-dependent I-V are measured on a scanning confocal microscope (Zeiss Axio Imager 2) using a long working distance objective (50x, NA = 0.55). Devices are contacted using piezoelectrically controlled micromanipulators (MiBots, Imina Technologies). I-V curves are measured with a Keithley 236 Source-Measure Unit using custom LabView programs. Laser powers are measured using a USB power meter (ThorLabs). All measurements are performed under ambient temperature and pressure.

Absorption and EQE

Absorption and EQE are measured using a home-built optical setup with a long working distance objective (50x, NA = 0.55). A supercontinuum laser (Fianium) is coupled to a monochromator to produce a tunable, monochromatic light source. A chopper and lock-in detection are used for all measurements. For absorption, the sample reflectance is measured using a NIST-calibrated photodetector (Newport 818-ST2-UV/DB) with a beamsplitter. A protected silver mirror (Thorlabs) is used to calibrate the reflectance based on its reported reflectance curve, and a dark background is subtracted from both measurements. For EQE, the current generated by the sample is probed using MiBots and compared to the current collected by the NIST calibrated photodetector when placed at the sample position, corrected by the photodetector's responsivity. When measurements were taken with

Mibots in place, absorption and EQE measurements are both corrected by a shading factor of 1.39 that corrects for the shading of the MiBot tips, which is calculated by comparing absorption with and without the tips in place and averaging over the spectral range 450 nm–650 nm.

Solar Simulator

One-sun I-V curves are measured using a 1 kW Xenon arc lamp (Newport Oriel) with an AM1.5G filter (ABET Technologies). To ensure 100 mW/cm^2 incident power, the lamp power is adjusted to generate the correct current on a Si reference cell placed at the same location as the sample. MiBots are used to contact the device, and I-V curves are measured with a Keithley 2425 SourceMeter using custom LabView programs.

For Schottky-junction solar cells, the current density is divided by a spectral mismatch factor to account for the difference in bandgap between our WS_2 sample and our Si reference cell and the difference in spectrum between our solar simulator and AM1.5G (*55*). As no EQE data was available for our device below 400 nm, linear extrapolation was used, leading to about a 5% error in the spectral mismatch factor and the reported J_{SC} values. The device area was assumed to be that of the Au disk, which has a diameter of 28 µm.

For carrier-selective contact solar cells, as the EQE is position dependent, the spectral mismatch correction was not used. The device active area was assumed to be equal to an annulus with an inner radius of the metal disk diameter, and an outer radius of the metal disk diameter plus the measured majority carrier diffusion length (13 µm).

Cross-sectional Analysis by Transmission Electron Microscopy

Site-specific, cross-sectional lamella samples were prepared near the middle of metal contacts using a Nova 600 NanoLab (Thermo Fisher) scanning electron microscope with a gallium focused ion beam and AutoProbe 200 sample lift-out system (Oxford Instruments). TEM imaging was carried out in a Tecnai TF-30 (Thermo Fisher) operated at 300 kV in high-resolution TEM mode.

Device Simulations

Absorption and generation are calculated using the transfer matrix method, with optical constants for WS_2 taken from literature (*3*, *64*).

For Schottky-junction devices, we then use the calculated generation rate as an input into a finite-element device physics simulation software package that solves the semiconductor drift-diffusion equations. All other device simulations are performed using Lumerical CHARGE, a software package which uses the finite-element drift-diffusion method to calculate charge transport in semiconductor devices. The WS_2 doping was specified by the bulk crystal vendor (HQ Graphene). Other WS_2 parameters, including bandgap (*57*), work function (*58*), DC permittivity (*63*), effective mass (*59*), out-of-plane mobility (*60–62*), and photoluminescence quantum yield (*65–67*) are taken from literature and listed in Table 1. The radiative recombination coefficient is calculated using the Roosbroeck-Shockley relation (*102*), and the Shockley-Read-Hall lifetime for minority carriers is then estimated using the photoluminescence quantum yield.

For carrier-selective contact devices, band diagrams and I-V curves are calculated using Sentaurus TCAD. The parameters used in device simulations, as well as their sources, are listed in Table 2.

Appendix C: Analytical StroboSCAT Solution

Our initial differential equations are:

$$\frac{dN}{dt} = -R_A N^2 - \frac{1}{\tau_x} N + D_x \nabla^2 N + \sigma s \nabla^2 T$$

$$\frac{dT}{dt} = \alpha N^2 + \beta N - \frac{1}{\tau_T}[T - T_0] + D_T \nabla^2 T$$

with N being $N(r,t)$ and T being $T(r,t)$. We will now make a simplification so that we can solve these as a function of time, by assuming that there is no spatial dependence and no diffusion. We will also assume that the quantum yield is zero, i.e. all recombination is nonradiative.

$$\frac{dN}{dt} = -R_A N^2 - \frac{1}{\tau_x} N$$

$$\frac{dT}{dt} = \alpha N^2 + \beta N - \frac{1}{\tau_T}[T - T_0] = -\frac{E_g}{c}\frac{dN}{dt} - \frac{1}{\tau_T}[T - T_0]$$

where we have rewritten the T equation in terms of dN/dt.

Analytic Solution for N

Starting with the N equation:

$$\frac{dN}{dt} = -R_A N^2 - \frac{1}{\tau_x} N$$

we can identify that this is actually in the same form as the differential equation used in population dynamics, or the logistic equation:

$$\frac{dP}{dt} = rP\left(1 - \frac{P}{K}\right) = -\frac{r}{K}P^2 + rP$$

which has the solution

$$P(t) = \frac{K}{1 + \left(\frac{K - P_0}{P_0} e^{-rt}\right)} = \frac{KP_0}{P_0 + (K - P_0)e^{-rt}}$$

We can identify that in our equation, $N = P$, $N_0 = P_0$, $r = -\frac{1}{\tau_x}$, and $K = -\frac{1}{R_A \tau_x}$. This leads us to the solution for N:

$$N(t) = \frac{-N_0}{R_A \tau_x \left(N_0 + \left(-\frac{1}{R_A \tau_x} - N_0\right) e^{t/\tau_x}\right)}$$

and simplifying we have our final solution for N:

$$\boxed{N(t) = \frac{N_0}{(1 + N_0 R_A \tau_x)e^{t/\tau_x} - N_0 R_A \tau_x}}$$

We can also define a new function z, which will become useful later:

$$z = \frac{(1 + N_0 R_A \tau_x)e^{t/\tau_x}}{N_0 R_A \tau_x}$$

and write N in terms of z:

$$N = \frac{1}{R_A \tau_x (z - 1)}$$

Analytic Solution for T

Starting with the T equation:

$$\frac{dT_{abs}}{dt} = -\frac{E_g}{c}\frac{dN}{dt} - \frac{1}{\tau_T}[T_{abs} - T_0]$$

where we have written $T = T_{abs}$ to signify that this is the absolute temperature, not the change in temperature. We can change variables to change in temperature T by writing $T = T_{abs} - T_0$ and noting that $\frac{dT}{dt} = \frac{dT_{abs}}{dt}$. We'll also gather all the terms with T on one side.

$$\frac{dT}{dt} + \frac{1}{\tau_T} T = -\frac{E_g}{c} \frac{dN}{dt}$$

Now, let's calculate $\frac{dN}{dt}$ in terms of z, noting that $\frac{dz}{dt} = z/\tau_x$, since it is just an exponential multiplied by a constant prefactor.

$$\frac{dN}{dt} = \frac{dN}{dz}\frac{dz}{dt} = \frac{1}{R_A \tau_x} \frac{-1}{(z-1)^2} \frac{z}{\tau_x}$$

which, substituting back into our differential equation for T, gives us

$$\frac{dT}{dt} + \frac{1}{\tau_T} T = \frac{E_g}{c R_A \tau_x^2} \frac{z}{(z-1)^2}$$

Now we can get this differential equation in terms of z by noting that $\frac{dT}{dt} = \frac{dT}{dz}\frac{dz}{dt} = \frac{z}{\tau_x}\frac{dT}{dz}$:

$$\frac{z}{\tau_x}\frac{dT}{dz} + \frac{1}{\tau_T} T = \frac{E_g}{c R_A \tau_x^2} \frac{z}{(z-1)^2}$$

and simplifying to get dT/dz alone:

$$\frac{dT}{dz} + \frac{\tau_x}{\tau_T}\frac{1}{z} T = \frac{E_g}{c R_A \tau_x} \frac{1}{(z-1)^2}$$

This is a nonhomogeneous first order linear ODE. We can use the integrating factor technique to solve it.

$$\exp\left[\int P(z) dz\right] = \exp\left[\int \frac{\tau_x}{\tau_T}\frac{1}{z} dz\right] = \exp\left[\frac{\tau_x}{\tau_T}\ln(z)\right] = z^{\tau_x/\tau_T}$$

In the integrating factor technique, we multiply the whole equation by the integrating factor:

$$z^{\tau_x/\tau_T}\frac{dT}{dz} + \frac{\tau_x}{\tau_T}\frac{z^{\tau_x/\tau_T}}{z} T = \frac{E_g}{c R_A \tau_x} \frac{z^{\tau_x/\tau_T}}{(z-1)^2}$$

Then we use the product rule to simplify the homogeneous part of the equation:

$$\frac{d}{dt}\left(z^{\tau_x/\tau_T}T\right) = z^{\tau_x/\tau_T}\frac{dT}{dz} + \frac{\tau_x}{\tau_T}z^{\tau_x/\tau_T-1}T$$

which gives:

$$\frac{d}{dt}\left(z^{\tau_x/\tau_T}T\right) = \frac{E_g}{cR_A\tau_x}\frac{z^{\tau_x/\tau_T}}{(z-1)^2}$$

And now we can integrate both sides from 0 to t to get:

$$\int_{t=0}^{t}\frac{d}{dt}\left(z^{\tau_x/\tau_T}T\right) = \frac{E_g}{cR_A\tau_x}\int_{t=0}^{t}\frac{z^{\tau_x/\tau_T}}{(z-1)^2}$$

$$z(t)^{\tau_x/\tau_T}T(t) - z(t=0)^{\tau_x/\tau_T}T(t=0) = \frac{E_g}{cR_A\tau_x}\int_{t=0}^{t}\frac{z^{\tau_x/\tau_T}}{(z-1)^2}\,dz$$

At $t = 0$, $T = T_0$, and z is

$$z = \frac{(1+N_0R_A\tau_x)}{N_0R_A\tau_x} = 1 + \frac{1}{N_0R_A\tau_x}$$

So we have

$$z(t)^{\tau_x/\tau_T}T(t) - T_0\left(1+\frac{1}{N_0R_A\tau_x}\right)^{\tau_x/\tau_T} = \frac{E_g}{cR_A\tau_x}\int_{t=0}^{t}\frac{z^{\tau_x/\tau_T}}{(z-1)^2}\,dz$$

So we have arrived at an equation for T:

$$\boxed{T(t) = z(t)^{-\tau_x/\tau_T}\left(T_0\left(1+\frac{1}{N_0R_A\tau_x}\right)^{\tau_x/\tau_T} + \frac{E_g}{cR_A\tau_x}\int_{t=0}^{t}\frac{z^{\tau_x/\tau_T}}{(z-1)^2}\,dz\right)}$$

Appendix D: Nature Materials Cover Art

I designed the cover art for the October 2018 issue of Nature Materials, to accompany the article cited below:

H. A. Atwater, A. R. Davoyan, O. Ilic, D. Jariwala, M. C. Sherrott, C. M. Went, W. S. Whitney, J. Wong, Materials challenges for the Starshot lightsail. *Nat. Mater.* **17**, 861–867 (2018).